Modeling the dynamics of a spar-type floating offshore wind turbine

MSc. Thesis

Laurens B. Savenije

December 4, 2009

Technical University Delft
Wind Energy Research Group

Siemens Wind Power
Offshore Center of Competence

Preface

This MSc thesis is done in cooperation between the TU Delft and Siemens Wind Power. The graduation committee consists of:

Prof. dr. G.J.W. van Bussel	Delft University of Technology
Ir. T. Ashuri	Delft University of Technology
Ir. E. de Beer	Siemens Wind Power
Dr. ir. J.W. Staerdahl	Siemens Wind Power
Dr. ir. H.J. de Koning Gans	Delft University of Technology

I would like to thank some individuals for the successful completion of this graduation project.

First, I would like to thank my committee for all the help, advice, feedback and evaluating this report. In addition, many thanks go to Turaj for guiding me through this project and encouraging me to write a conference and journal paper. Thank you Eric for helping me out whenever I needed it and the great time in Stavanger. Thank you Jesper for always giving me the required data in short notice.

Thank you also to David Molenaar (from Siemens Wind Power) for this great opportunity, for all the advice and feedback, and for giving me the chance to attend the installation of Hywind in Stavanger, Norway.

Big thanks to my parents for the infinite amount of trust and support, and to Anna without whom I could have never succeeded.

Abstract

The installation of floating wind farms in deeper water is encouraged by the stronger and steadier wind, the lower visibility and noise impact, the absence of road restrictions, but also the absence or shortage of shallow water. In the summer of 2009, the first large-scale floating wind turbine "Hywind" was installed. Hywind is a spar-buoy concept with three catenary mooring lines.

Offshore wind power in general is still in its infancy; floating wind turbines are a completely novel concept. The experience with modeling such turbines is still limited. Furthermore, existing models for the design of offshore wind turbines are highly complex as they focus - by definition - mostly on the forces of the wind on the turbine. The correctness and applicability of existing simulation models for the design of floating wind turbines can therefore not be assumed a-priori and need to be researched. This requires that the driving physical processes governing the behaviour of floating wind turbines are investigated first. For this purpose, a new basic model has been developed. The requirement of the model is that it incorporates the most significant physical processes so as to be able to provide insight into the dominant physical behaviour of spar-type floating wind turbines. Such a basic model can subsequently be used for the validation of existing, more complex models.

In this thesis, the requirements of the model have been set and the dominant physical processes determined. As a result, certain assumptions and simplifications have been made, which illustrate the limitations of the model. Subsequently, the physically-based A.T.FLOW model has been developed. Various verification methods show that A.T.FLOW simulates load cases as expected and is a useful tool for assessing the physical behaviour of spar-type floating wind turbines.

The coming two years the forcing and behaviour of the operating full-scale Hywind demo project is monitored. This data should be used to further test and validate A.T.FLOW and to guide further development of the model.

Contents

Chapter 1

Introduction

1.1 The floating wind turbine concept

Offshore wind energy has high potential [1]. EWEA statistics show that a total of 1,471 MW was installed worldwide by the end of 2008, all of it in EU waters[1]. The installation of wind farms in deeper water is encouraged by the stronger and steadier wind, the lower visibility and noise impact, the absence of road restrictions [2], but also the absence or shortage of shallow water. Most of the offshore wind resource potential is available in water deeper than 30m [3; 4], but most of the European offshore wind turbines have been installed in water shallower than 20 m by driving monopiles into the seabed or by relying on conventional concrete gravity bases [3]. The deepest installed offshore wind turbine is the Beatrice wind farm demonstrator project using jackets with a depth of 44 m [5]. Deeper water requires larger, more expensive supporting structures. For water deeper than 60 m floating wind turbines are a feasible option [6; 7]. A disadvantage of floating wind turbines is their enhanced dynamics [1], hence the importance of research on floating wind turbine behaviour.

A floating turbine can be stabilised by buoyancy, ballast and mooring. Often a combination of these is used. An object in water has a lifting force, called the buoyancy force. This force acts through the buoyancy point, generating a moment that restores the object when heeled. Ballast increases stability by lowering the center of gravity and a mooring system by mooring line tension. Types of floating concepts are the tension leg platform (TLP) and the spar-buoy, see figure 1.1.

[1]Seas of change: offshore wind energy, 2009; http://www.ewea.org/index.php?id=1611

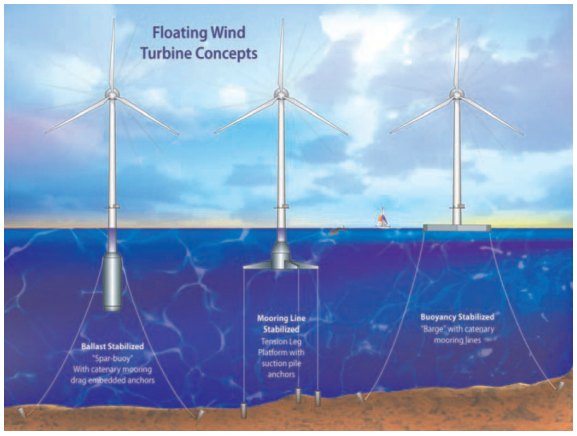

Figure 1.1: Floating wind turbine concepts [2]

1.2 Hywind demo project

The last few years the wind industry has shown interest in floating wind turbines. Statoil is the first to build a multimegawatt floating wind turbine. In the summer of 2009 their concept, Hywind, was installed in the deep waters of the Norwegian coast, see figure 1.2. Hywind is a spar-buoy concept with three catenary mooring lines using mainly ballast to stabilize the platform. The spar has a draft of 100 m and a maximum diameter of 8.3 m. The lines are attached to an anchor at a depth of 210 m. The pilot project was assembled inshore in Amøyfjorden near Stavanger and is located in the North Sea some 10 kilometres offshore Karmøy in the county of Rogaland. A three metre high model has already been tested successfully in SINTEF Marinteks wave simulator in Trondheim. The full-scale turbine will be monitored for two years.

The Hywind concept combines known technologies in a completely new setting and opens up the possibility for the wind industry to capture the wind energy within deep water environments. The objective of the pilot is to reduce costs so that floating wind power can compete in the power market. Large floating offshore wind farms can contribute to the growing energy demand and sustainable solutions. StatoilHydro is investing around NOK 400 million in the construction and further development of the pilot, and in research and development related to the wind turbine concept.

Siemens Wind Power is contracted by StatoilHydro to deliver and install the 2.3 MW wind turbine. Technip has build the floating elements and is in charge of

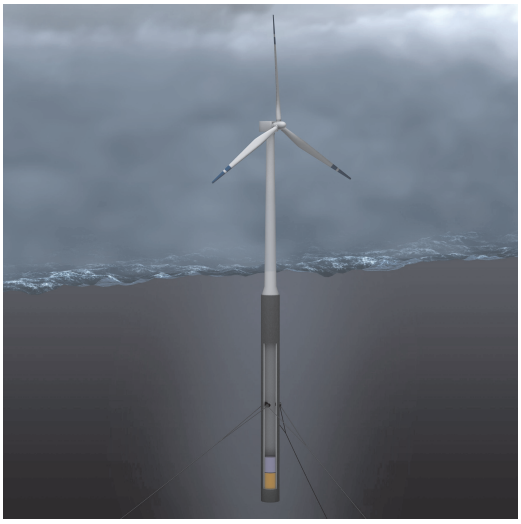

Figure 1.2: Hywind spar buoy concept (source: StatoilHydro)

the offshore installation. Nexans has installed the cable to shore and Haugaland Kraft is responsible for the landfall. Enova is supporting the project with 59 million NOK.

1.3 Fixed vs floating

Both concepts are subjected to wind and wave loads. Wind and water that pass the turbine transfer their energy to the structure. The dynamics of the turbine rotor result in aerodynamic damping. The dynamics of the submerged structure result in hydrodynamic damping. Both concepts are enforced by gyroscopic moments caused by the fast rotation of the rotor.

A fixed offshore turbine is attached to the soil. The reaction forces and moments of the soil prevent the turbine from displacing or rotating where the turbine is clamped. The turbine does deflect due to the acting loads like a clamped beam.

A floating turbine is not clamped. It has enhanced dynamics due to the six extra degrees of freedom (three translational: surge, sway and heave; three rotational: roll, pitch and yaw). Both concepts have three bending degrees of freedom (side-side, fore-aft and torsional). The buoyancy and mooring forces, which act as springs, prevent the wind turbine from drifting of and sinking. When the tur-

bine is static the weight, buoyancy force and mooring forces are in equilibrium. The buoyancy and mooring forces react to the displacements of the turbine. The increased dynamics of the floating turbine result in higher aerodynamic and hydrodynamic damping. Also the gyroscopic moments will be higher.

A fixed offshore wind turbine is designed for natural frequencies around 0.3 Hz. That way, the natural frequencies are clear from the 1P and 3P rotor frequencies. A rotational speed of 16 rpm (rotations per minute) corresponds to a 1P frequency of $12/60 = 0.27$ Hz. This is the frequency of one full rotation. 3P indicates the frequency that a blade passes the tower. When there are three blades, the 3P frequency is 0.8 Hz. Around 0.3 Hz waves are wind-generated.

The six extra degrees of freedom of the floating turbine have large periods, hence low frequencies (see Table 1.1). This is due to the high mass and inertia of the floating platform. Around these low frequencies infra-gravity waves are present, which contain less energy. Swell waves occurs around frequencies of 1/10 Hz. Due to the increased dynamics of a floating turbine, the tower bending stiffness should be increased. This results in higher natural bending frequencies. The spar structure is very stiff and will have a larger natural frequency than the tower. Overall, the bending natural frequencies will increase for a floating spar-type concepts. The floating turbine must be designed in a way that the bending natural frequency will not resonate with 3P.

Table 1.1: Natural periods of a floating and fixed turbine [8]. Surge, sway and heave are the global displacements. Roll, pitch and yaw are the Euler angles. The bending modes are side-side, fore-aft and torsional.

	Floating Hywind (s - 1/Hz)	Fixed (s - 1/Hz)
Surge	1/109.3	-
Sway	1/108.7	-
Heave	1/27.7	-
Roll	1/25.2	-
Pitch	1/25.3	-
Yaw	1/18.2	-
Side-side	> 0.3	$\simeq 0.3$
Fore-aft	> 0.3	$\simeq 0.3$
Torsional	> 0.9	> 0.9

The acting loads and natural frequencies of fixed and floating concepts are different, which results in different dynamic behaviour.

1.4 Modeling of spar-type floating wind turbines

In terms of simulating acting loads and dynamic behaviour, the fixed and floating turbine require different models. Attemps have been made to simulate spar-type floating wind turbines by extending or combining existing models. Design codes for wind turbines and floating platforms already exist separately. Wind turbine design codes are used to model and simulate wind turbine behaviour, as well as to carry out design calculations [9]. Hydrodynamic models analyze the wave interaction and dynamic responses of offshore floating platforms. Three established design codes for spar-type floating wind turbine are H2SR, BHawC and OC3. The design code H2SR is presented in more detail, because results of A.T.FLOW and H2SR are compared for verification in Chapter 4.

- **H2SR** - A combination of SIMO/RIFLEX developed by MARINTEK and HAWC2 developed by RisøNational Laboratory. HAWC2 is a code developed for calculation of dynamic wind turbine load and response including coupling to control [5]. HAWC2 (Horizontal Axis Wind turbine Code) is a state-of-the-art aero elastic code for simulation of the dynamic response of horizontal axes 2- and 3-bladed wind turbines in time domain. The model contains a very detailed description of the aero elastical and mechanical aspects existing within a wind turbine. H2SR has been validated towards results from scaled model measurements [10]. The submodels of HAWC2 contain[2]

  - Wind: Wind shear, tower shadow, up-flow, yawed flow
  - Turbulence: MANN and VEERS models
  - Aerodynamics: Blade element momentum model
  - Structure: Finite element model (beam elements)
  - Structure: 3 substructures (blades, nacelle/shaft, tower)
  - Structure: Sub-model for large non-linear deflections
  - Controller: Stall, active stall, pitch, variable pitch
  - Offshore: Wave- and current models

  SIMO/RIFLEX is a combination of SIMO and RIFLEX, both software tools developed by MARINTEK. SIMO is time tomain simulation program for study of motions and station keeping of multibody floating vessels. Included are the modeling of the environment, the station keeping forces and connecting force mechanisms. The simulated environment contains[3]

  - Waves: regular and irregular

[2] http://www.iet.aau.dk

[3] http://www.sintef.no/Home/Marine/MARINTEK/Software-developed-at-MARINTEK/

  - Wind: constant and with gust
  - Current: constant and varying

  The relevant station keeping force for spar-type floating wind turbines comes from the catenary mooring lines. SIMO can model the mooring system by

  - A general tension elongation relationship
  - Any number of segments, branches, buoys and clump-weights

  Several force models are available ranging from

  - Hydrostatic stiffness
  - Damping (linear and quadratic)
  - Wind forces
  - Current forces (linear and quadratic)
  - First and second order wave excitation forces

  The main limitation of SIMO is that it only models rigid bodies. Therefore RIFLEX accounts for the structural bending of the spar. In many ways SIMO and RIFLEX are the same, but RIFLEX is designed to analyse slender marine structures including structural analyses. It models the flexibility by finite element analysis.

- **BHawC** - Siemens Wind Power extended the aeroelastic wind turbine design code BHawC (Bonus energy Horizontal Axis Wind turbine Code). Six degrees of freedom have been added to the system. The spar is assumed infinitely stiff. The wave loads are not performed by BHawC, but given as inputs from other models (SIMO, WAMIT and MIMOSA). The wave loads are represented as a net force and moment around mean water level (MWL). Therefore one extra node at MWL is added to the model. The net wave force is given by SIMO, using results from WAMIT (Wave Analysis at MIT). The mooring stiffnesses are given by MIMOSA.

- **OC3** - The Offshore Code Comparison Collaboration (OC3) has modeled different concepts of floating wind turbines. The modelin of the spar-type Hywind demo project is currently in progress. In the OC3 program the aero-servo-elastic wind turbine codes FAST and ADAMS account for the wind turbine simulations. The commonly employed external hydrodynamic wave-body interaction program WAMIT accounts for the hydrodynamics. The mooring line force-displacement relationship was generated by FAST.[4]

[4] http://wind.nrel.gov/public/jjonkman/

The strength of H2SR and OC3 is that they use state-of-art models for both aerodynamics and hydrodynamics. However, the fact that these models are state-of-art separately does not guarantee that they are state-of-art when combined, especially if the application is a novel concept such as floating offshore wind turbines. Reasons for this include

1. Different models are based on different assumptions, which may be conflicting.
2. Coupling of two models with different structures may lead to unexpected results due to interface issues.
3. The models were developed for a specific purpose, which is different from the new application. Bringing two models together does not mean that they together bring what is required.

Extending a single, complex model such as BHawC for designing floating wind turbines is ignoring the fact that this model is - by definition - focused too much on one part of physics. This approach undermines the fundamental difference of the problem to be investigated. Therefore, there is a major risk that essential aspects of the problem are overlooked. This risk is increased further by the complexity of the model which does not allow testing and validation to verify model suitability. The same applies for extending a complex floating platform model with aerodynamics.

It should be noted that floating wind turbines are a completely novel concept. The experience with modeling such turbines is still limited. The applicability of existing simulation models for the design of floating wind turbines can therefore not be assumed and should be confirmed. For this, a new basic model must be developed. This model should be built upon the most significant physics and provide insight in the dominant physics and behaviour of spar-type floating wind turbines. Such a basic model can then be used for the validation of existing, more compex models.

1.5 Problem formulation and approach

In view of this background and motivation, the problem is formulated as:

Develop a physically-based model to assess behaviour of spar-type floating wind turbines.

Physical behaviour is understood as the static and dynamic response of the turbine as a result of the acting loads. Assessing physical behaviour requires clear understanding of the relation between results and physics used in the tool. The

model is a new simulator containing the dominant physics, which leaves out the unnecessary to give clear insight in the physics that drive a floating offshore wind turbine. The tool is designed for the Hywind concept, but should be applicable to other spar-type floating concepts. This leads to the first task:

Task 1 *Identify the dominant physical processes the model should contain.*

When the dominant physics have been determined it is clear which non-relevant parts can be excluded. Parts are left out or simplified and the content and set-up of the model is subsequently built up. The model is created.

Task 2 *Develop the model.*

The required verification and validation leads to the final tasks.

Task 3 *Verify the model by using results from other verified models, proven theory and model predictions.*

Task 4 *Validate the analysis tool by using measurement data.*

This report addresses task 1, 2 and 3. Task 4 will be performed when the measurements from Hywind are available. It is important to know the forces acting on every part of the structure, but understanding why these forces act and what are their consequences is of even more importance. This research aims to increase our understanding of floating wind turbine behaviour, contributing to the state-of-the-art of scientific knowledge. The model is written in MATLAB code in time domain. In some of the figures the values on the axes are left out for confidential reasons.

1.6 Report outline

The report consists of three parts. Part 1 is on the modeling of spar-type floating wind turbines. Chapter 2 presents the requirements, assumptions and limitations of the new model, which is referred to as A.T.FLOW. Chapter 3 presents the structure and contents of A.T.FLOW.

Part 2 describes the verification methods. Chapter 4 verifies model parts through comparisons with results from existing models. Chapter 5 presents model predictions on three load cases which are compared to the results of A.T.FLOW.

Part 3 contains the conclusion and recommendations based on the results in Chapters 6 and 7, respectively.

Part I

Modeling of a spar-type floating wind turbine

Chapter 2

Model requirements and limitations

Section 2.1 presents the model requirements for A.T.FLOW. Based on the requirements assumptions are made, which are presented in section 2.2. The assumptions result in limitations of the model. These are also given in section 2.2.

2.1 Model requirements

The principle requirement of the new model A.T.FLOW is to assess the physical behaviour of the spar-type floating turbine. To obtain the best assessments, the analysis tool must be clear to the user. This clarity is obtained in two steps

1. The theory must be clear to the user. A good assessment can only be done when the user understands the theory behind the model. The theory is however often complex. Therefore the theory is simplified as much as possible without harnessing the results too much. Theory which has minor impact on the physical behaviour is left out. Secondly, good documentation of the theory is crucial.

2. The code must be clear to the user, so that it is practical in usage. This is done by good documentation of the code and a simple structure of the model.

In a later stadium further research on this type of modeling could indicate a need for model adaption or extention. Therefore a requirement is that the model should be easy to adapt or extend. A simple model structure with independent modules should enable this.

This would make a tool which enables good assessments on spar-type floating turbine behaviour.

2.2 Model assumptions and limitations

This section focusses on the simplifications of the theory mentioned in item 1 of section 2.1. This results in a list of assumptions and resulting limitations of the model. The main assumptions are summarised in the bullets below. Consequently each assumption is clearified. Assume

- A uniform wind velocity
- A single regular wave
- An infinitely stiff structure
- All rotations of the support platform are small
- A quasi-static mooring system
- A quasi-static controller
- A standard BEM code
- Morison's equation for hydrodynamic loads

The model is written in the time domain using MATLAB.

2.2.1 Wind and Waves

The description of the wind velocity can be deterministic or stochastic. A deterministic wind description is uniform (constant in space and time) or stepwise (a sequence of stepwise changes in the wind velocity). A stochastic wind description is turbulent (variable in space and time) and corresponds to reality.

The wave description can also be deterministic (regular) or stochastic (irregular). A regular wave is harmonic and has a constant frequency and wave height. An irregular wave corresponds to real site conditions. By superposition of many regular waves with different frequencies, a wave spectrum is created which simulates a certain cite condition.

A.T.FLOW assumes a stochastic wind description which is variable in space, but fixed in time. So turbulence is neglected. The wave description is assumed regular. These simplifications of environmental conditions are based on the same arguments. Wind desciptions with turbulence and irregular wave descriptions are used to analyse life-time loads, hence fatigue analyses. This research does not focus on life-time behaviour. Secondly, by simplifying the wind and wave description, the results can more easily be related to the inputs. In this way the model results can be better assessed. Finally, it is expected that turbulence will have minor impact on the physical behaviour due to the high mass and inertia of the body.

2.2.2 Mechanical

Structural body

A floating wind turbine is a flexible multibody system. A.T.FLOW assumes that the structure is single rigid body. A rigid body may be treated as a point mass moving with the center of mass of the body. All the mass moments of inertias are computed about the center of mass.

The bending of the structural elements is neglected. A real flexible structure has frequencies of bending modes, which can resonate with free body modes. This is neglected by A.T.FLOW. Since the frequencies of the bending modes and free body modes are far apart as shown in Table 1.1. Therefore resonance will not occur. Structural bending influences the internal stresses of structural parts. This research does not focuss on fatigue or maximum design loads of structural parts, hence the irrelevance of stress. The system rotates around a point approximately 40 m above the spar bottom. The structural bending causes the largest deflections at the tower top changing the relative wind velocity of the blade elements. This results in inaccuracies of the aerodynamic loads for a rigid body. The center of mass is assumed fixed in time, but will in reality displace during deformations. This variation of the center of mass is in the order of a few centimeters.

Mooring system

The three catenary mooring lines act as springs preventing the platform from drifting of. The pretension in the lines and the attached clump weight result in a high translational stiffness. The yaw stiffness is created by the delta connection in the line, where the lines are connected to the substucture.

The dynamics of the mooring system can influence the tension in the mooring lines. The dynamic tension is related to the elastic stiffness of the line for non-snapping conditions. [11]. To simplify the tension-line calculations the mooring system can be assumed quasi-static, negecting the mooring dynamics. Quasi-static means that for a given platform displacement the mooring system module solves for the tensions of each mooring line by assuming that each cable is in static equilibrium at that instant [2]. This quasi-static approach ignores the inertia and damping of the mooring system. While some literature states the importance of modeling mooring dynamics [12], other recommend quasi-static modeling [2; 13; 14]. An argument is that the quasi-static approach, suitable for the design of catenary mooring systems in shallow water (depth less than approximately 100 m), is generally considered inadequate for deep water applications [15]. In deep water dynamic tensions can be excited due to the platform motions [15]. The counter-argument is that the inertia of the mooring system

contributing to the dynamic tension can be ignored compared to the platform inertia and ignoring the mooring system damping is a conservative approach [2].

For A.T.FLOW the mooring system is assumed static. This assumption was made due to time restrictions of this thesis project. The static non-linear load-displacement relation (for translational and yaw) calculated by Statoil is used as input to the model. The static mooring system is modeled in a way that adaptation to a dynamic mooring system is possible.

Euler angles

With the assumption that all rotations of the support platform are small, rotation sequence becomes unimportant. Consequently, all the complications of using Euler angles are avoided, where the order of rotation is significant, for the derivation and implementation of the equations of motion in A.T.FLOW [2]. However, a single large angle ω_x, ω_y or ω_z is still accurate, but the combination of two large angles is not. Appendix C gives more background on Euler angles.

2.2.3 Controller

A dynamic controller regulates the torque of the generator and the pitch angle of the blades to optimize the power output and loads on the rotor. The balance of the aerodynamic loads, rotor inertia, generator torque and mechanical friction results in an angular velocity of the rotor. A.T.FLOW assumes a static controller with a fixed angular velocity of the rotor and a fixed pitch angle of the blades. When the relative wind velocity at the rotor changes the control values remain static. These control values are averages from BHawC calculations (using a dynamic controller) during stable production of e.g. a uniform wind velocity of 10 m/s. Notice that the "static controller" is not really a controller, since it does not regulate anything.

With a static controller the inputs to the model are simplified and the results can more easily be related to the inputs. In this way the model results can be better assessed. A limitations is that the model is not appropriate for detailed aerodynamic research. A.T.FLOW is designed in a way that a more complex controller can be build in.

2.2.4 Aerodynamics

A wind turbine extracts energy from the wind. The wind velocity at the rotor decreases due to the presence of the rotor. To calculate the aerodynamic loads, the induced velocities at the rotor are required. Blade-Element-Momentum (BEM) theory can calculate these induced velocities. It is the most conservative theory

used for wind turbine design.

The main sources for inaccuracies in the BEM theory are [16]

- Yawed rotor conditions
- Use of 2D static aerofoil data

The yawed rotor results in a skewed wake, which causes a non-uniform induction distribution. The local induced velocities at the blades wil vary considerably from the azimuthally annular averaged values. The 2D static aerofoil data does not yield a good correlation between calculated loads and measurements due to 3D rotating effects and unsteady aerodynamic effects. To reduce the uncertainties in the BEM theory due to the limitations of the momentum equations and due to the inaccuracies in the aerofoil data, various corrections were included in the past years. This has resulted in the so-called 'Extended BEM' theory. Allthough the correction in the 'Extended BEM' theory improved aerodynamic load predictions, better models are still required [16].

The BEM code in A.T.FLOW is a standard BEM code, hence not using 'Extended BEM' theory. This limites the model to non yawed rotor conditions and basic aerodynamic research. When research on detailed aerodynamics is required, the BEM code can be extended. Yawed idling conditions can be simulated, since the presence of the rotor has barely any affect on the wind velocity. The empirical equation of Glauert is used for large axial induction factors.

2.2.5 Hydrodynamics

Morison's equation is the most common method used to simulate hydrodynamic loads on slender cylindrical structures. Morison's method can be used when diffraction is negligible. Diffraction deformes the incident wave field when the structure is large compared to the wave length. Froude-Krylov theory is an alternative to Morison's when inertia is dominant and drag is negligible. Froude-Krylov theory neglects viscous drag forces. The amount of diffraction is determined with the diffraction ratio R_{diffr}.

$$R_{diffr} = \frac{D_s}{\lambda_w} \tag{2.1}$$

with

R_{diffr}	Diffraction ratio
D_s	Spar diameter
λ_w	Wave length

Diffraction is negligible for $R_{diffr} < 0.2$. For a spar diameter of 8.3 m, Morison and Froud-Krylov can be used for wave lengths larger than 40 m. For waves with a steepness of 1:15 the corresponding wave heights should be larger than 2.7 m [17].

Flow separation increases the drag. When drag is no longer negligible the Froud-Krylov theory can no longer be applied. Only Morison can be used. The KC value indicates the ratio between the drag and the inertia force, hence the occurance of flow separation. The equation for the KC value is

$$KC = \frac{H_w}{D_s} \tag{2.2}$$

with

KC	KC value
H_w	Wave height

Flow separation is important for $KC > 2$, which is true for wave heights larger than 16.6 m [18]. Since smaller waves will be analysed the drag forces can be neglected.

It can be concluded that Morison's equation and Froud-Krylov theory can be used for wave heights in between $2.7 < H_w < 16.6$ m. For $H_w > 16.6$ m Morison's equation must be used. For $H_w < 2.7$ diffraction theory is required. This research focusses on wave heights larger than 3.0 m. Morison's equation is used for the hydrodynamic loads calculations although drag can be neglected.

The motion of the spar also causes hydrodynamic loads, known as hydrodynamic damping. When there is no wave, but the spar does move, Morison's equation should still be used. Diffraction depends on the wave length or in this case on the length of spar motion. The wave length can also be calculated by $\lambda_w = 1.56T_w^2$, with T_w the wave period. The natural periods of the free body modes are high, varying approximately from 18 to 110 sec (see Table 1.1). Diffraction will not occur and the usage of Morison's equation is justified.

Second order wave drift forces are neglected, which consist of mean wave drift forces and low-frequency wave drift forces. The low-frequency wave drift forces only occur in irregular waves. The neglection of mean wave drift forces is a limitation of A.T.FLOW. These drift foces can be implemented when needed.

Chapter 3

Hywind dynamic modeling

An overview is given of the degrees of freedom and coordinates of the system. Section 3.3 presents the structure of the model. In sections 3.4 to 3.10 the modules are presented.

3.1 Introduction

This chapter presents the contents and structure of A.T.FLOW, the analysis tool and simulator of a spar-type floating offshore wind turbine. A.T.FLOW consists of the following modules: Wind, Waves, Aerodynamic, Hydrostatic & Hydrodynamic, Mechanical, Controller and DOF Solver.

3.2 Degrees of freedom and coordinate systems

A rigid body in space has six degrees of freedom (DOF). Three DOFs specify the location of the center of mass and three additional DOFs specify the orientation of the body. The location of the center of mass is defined by X, Y and Z. The orientation of the body is defined by Euler angles θ, ϕ and ψ. The sequence of the Euler angles is: yaw - pitch - roll. The names of the degrees of freedom are

X	Surge	(Back - forward)
Y	Sway	(Side - side)
Z	Heave	(Up - down)
θ	Pitch	
ϕ	Roll	
ψ	Yaw	

Figure 3.1 illustrates the positions and orientations of the three coordinate systems. There are two coordinate systems: global and local. This model has one global coordinate system and two local coordinate systems. The global coordi-

nate system is fixed and positioned at the seabed. The origin of the first local coordinate system is positioned at the center of mass *cg* of the structure. The second local coordinate system is positioned at the hub center.

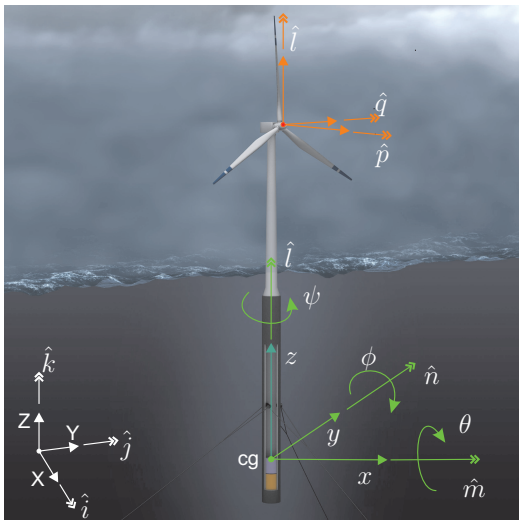

Figure 3.1: Coordinate systems

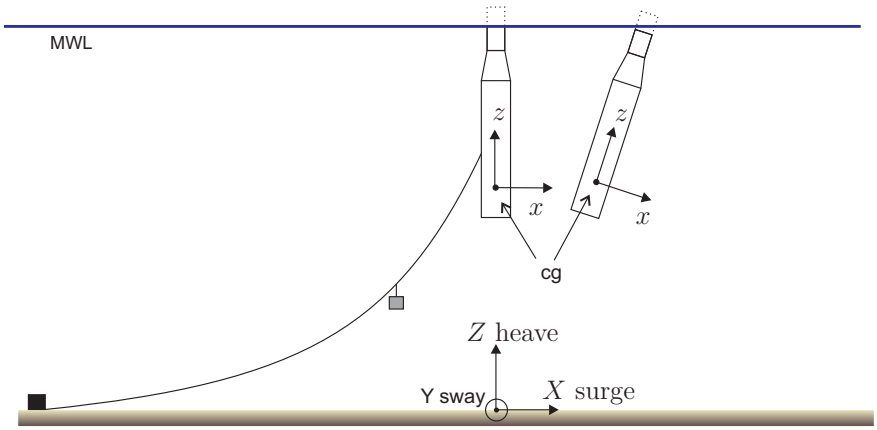

Figure 3.2: Orientation of the global coordinate system with respect to the mooring system

The coordinates of the global coordinate system are X, Y, Z with fixed base vectors $\hat{i}$, $\hat{j}$, $\hat{k}$. Figure 3.2 shows the orientation of the global coordiate system with respect to the mooring system. When the tensions in the mooring lines are equal and the body is is not inclined, the origin of the global coordinate system is positioned straight underneith the spar cg. Base vectors $\hat{k}$ and $\hat{l}$ are then aligned and the X axis is aligned with mooring line 1.

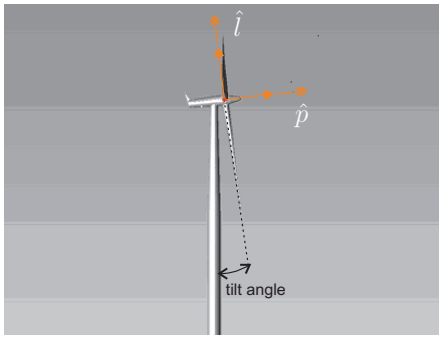

Figure 3.3: Second local coordinate system at hub

The coordinates of the first local coordinate system are x, y, z with free base vectors $\hat{m}$, $\hat{n}$, $\hat{l}$. The base vectors of the second local coordinate system are $\hat{p}$, $\hat{q}$ and $\hat{l}$. Base vector $\hat{p}$ is aligned with the main shaft of the turbine and $\hat{l}$ aligned with the rotor tilt as shown in Figure 3.3. To simplify the model, the coning of the blades and the rotor tilt are neglected.

3.3 Model structure

The model structure is presented in Figure 3.4. The modules are coupled through inputs and outputs. The DOF Solver module is the core, which solves the differential equations. The solution of the differential equation is $\mathbf{S}$, which contains the position, velocity, orientation and angular velocity of the center of mass.
The structure is briefly explained step by step. The modules that calculate the load on the floating turbine are the aerodynamic, mechanical, and hydrostatic & hydrodynamic modules. These are all bilaterally coupled to the DOF Solver. The aerodynamic module calculates the aerodynamic loads on the turbine $\vec{F}^{aero}$. The mechanical modules calculates the mooring loads $\vec{F}^{mooring}$ and gyroscopic loads $\vec{M}^{gyros}$, and the hydrostatic & hydrodynamic module calculates the hydrostatic & hydrodynamic loads $\vec{F}^{hydro}$. The other modules give inputs to the loads modules. The wind module contains the wind field description V_{field}. This is an input to the controller and the aerodynamic modules. The controller sets rotational speed

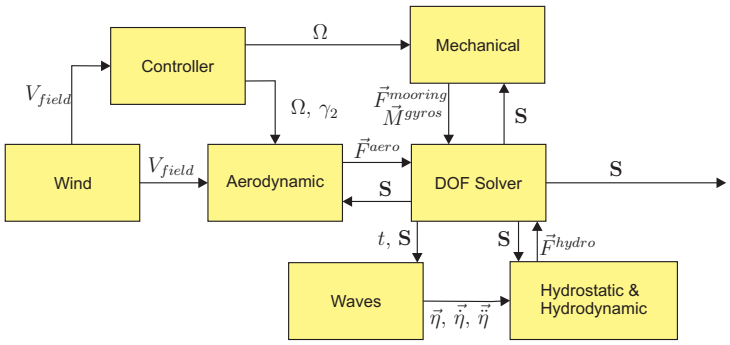

Figure 3.4: Coupled modules in model structure of A.T.FLOW

Ω of the rotor and the pitch angle γ_2 of the blade. The waves module contains the wave description $\vec{\eta}$,$\dot{\vec{\eta}}$,$\ddot{\vec{\eta}}$.

3.4 Wind module

The output of the wind module is the undisturbed wind field. A wind field at the wind turbine rotor is variable in space, time and direction, It is shaped by the undisturbed wind velocity V_w, wind shear, tower shadow and turbulence. It was assumed in section 2.2 that the wind field will be constant in space, time and direction, hereby turbulence is neglected. Inputs to the aerodynamic module are the undisturbed wind velocity at hub height V_w and the wind field velocities, denoted as V_{field}.

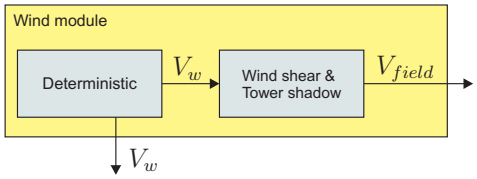

Figure 3.5: Structure and contents of the wind module

The direction of the wind depends on the wind angle β_{wind}, which is formulated with respect to the global coordinate system.

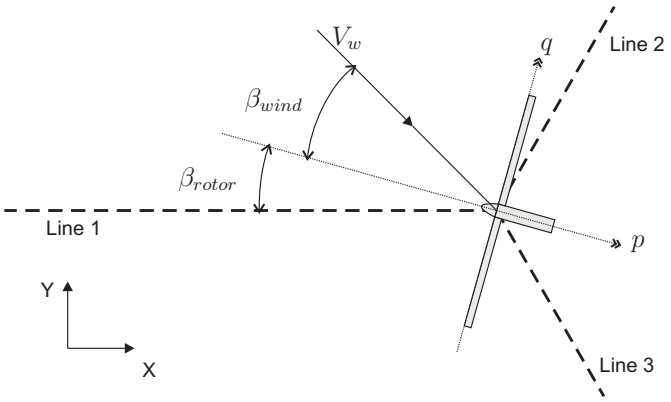

Figure 3.6: Wind angle with respect to the global coordiante system

3.4.1 Wind field

Wind shear is the variation of the free stream wind velocity with height. Close to the ground the wind velocity is close to zero, but by enlarging altitude, wind velocity increases. Tower shadow is the distortion of the average, undisturbed wind velocity caused by the presence of the tower in the wind field. The wind field shaped by shear and tower shadow is

$$V_{field} = R_{shear} R_{shadow} V_w \tag{3.1}$$

with

R_{shear}	Shear ratio
R_{shadow}	Shadow ratio

There are several ways to represent wind shear. By using a linear, power or logarithmic function [9]. Figure 3.7 shows the shear results of the three models. The power function, which is also the IEC standard, will be used in A.T.FLOW

$$R_{shear} = (\frac{H}{H_{obs}})^{\alpha_{PL}} \tag{3.2}$$

with

H	Height from mean water level (MWL)
H_{obs}	Height of wind speed observation
α_{PL}	Power law constant

The exponent is a highly variable quantity. A typical value for α_{PL} at an open offshore sea is 0.14 [19]. In Figure 3.7 the observation is done at hub height $H_{obs} = 65$ m. Therefore $R_{shear} = 1.0$, when $H = 65$ m.

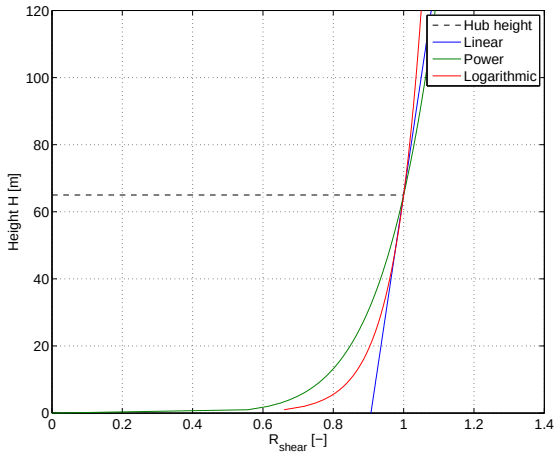

Figure 3.7: Shear functions with H and R_{shear}

Models to simulate tower shadow are the (1-cos) model and the potential flow (dipole) model. The results of the tower shadow models are the same [20]. The potential flow model will be used in A.T.FLOW. Because of the vortices behind the tower, the potential flow model is not usable for downstream velocity calculations. Since in this case only upstream velocities are relevant, the potential flow model can be used. The potential flow equation for R_{shadow} is

$$R_{shadow} = 1 - D_t(H)^2 \frac{X_{sh}^2 - Y_{sh}^2}{(X_{sh}^2 + Y_{sh}^2)^2} \tag{3.3}$$

with

D_t	Tower diameter at height H
H	Height from MWL
X_{sh}	Distance in X direction from blade to tower center
Y_{sh}	Distance in Y direction to tower center

Section 2.2 assumed that blade coning and rotor twist is neglected. Therefore X_{sh} is a constant value. The tower diameter at MWL is 6.0 m and at the nacelle 2.4

m. The coning of the tower is assumed linear from MWL to nacelle. Therefore

$$D_t = 6.0 - \frac{2.4}{H_{hub}} H \tag{3.4}$$

with

H_{hub} Hub height from MWL

Figure 3.8 shows the results of R_{shadow} for $X_{sh} = 7.0$ m. The wind velolity of a blade element is affected by tower shadow when a blade passes the tower. The change in wind velocity due to tower shadow creates a variation in loading every time the blade passes the tower.

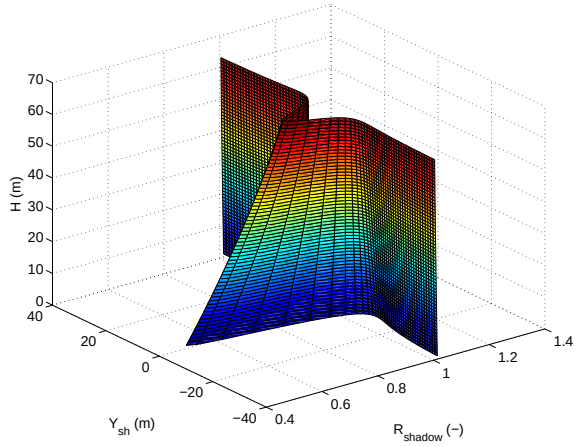

Figure 3.8: Tower shadow potential flow model at $X_{sh} = 7.0$ m

3.5 Controller

The input to the controller is the undisturbed wind velocity V_w at hub height. Section 2.2 assumed that the controller is static. It sets a rotor angular velocity Ω and blade pitch angle γ_2 for a certain V_w. These values are averages known from previous calculations done by BHawC. When the relative wind velocity at the rotor changes due to a wind gust or movement of the turbine, the control values remain fixed, hence static. Figures 3.9 and 3.10 show the static control settings for values of V_w.

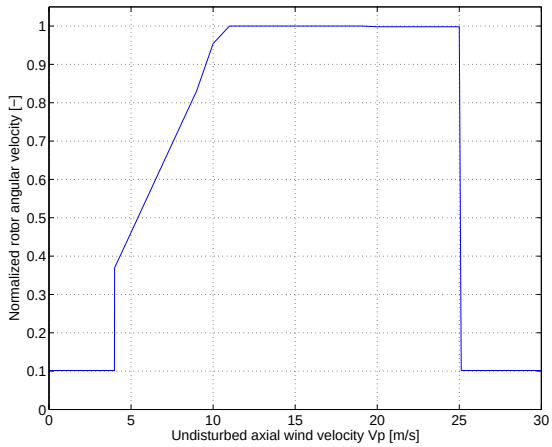

Figure 3.9: Normalized control settings of rotor angular velocity Ω for certain V_p

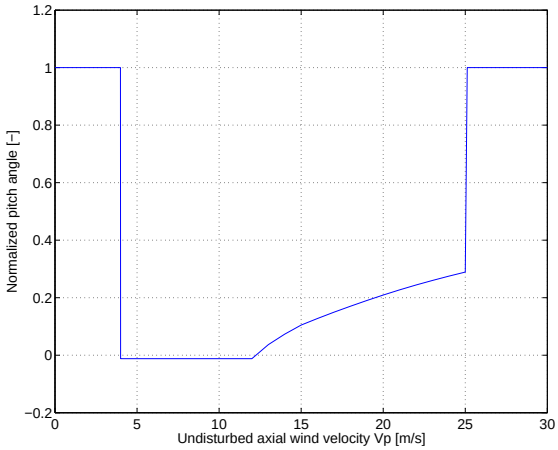

Figure 3.10: Normalized control settings of blade pitch angle γ_2 for certain V_p

3.6 Aerodynamic module

The aerodynamic module calculates the aerodynamic loads on each blade element using blade element theory and momentum theory. The structure of the module is presented in Figure 3.11. First the undisturbed wind velocity at hub height V_w with global coordinates is transformed to the second local coordinate system, with base vectors $\hat{p}$, $\hat{q}$ and $\hat{l}$. The BEM code numerically calculates

the induction factors a and a'. During a turbulent wake state, the induction factors are corrected with Glauert's correction. Next, the induced wind field is calculated. With the induced velocities known at each blade element, the aerodynamic loads are calculated using blade element theory. To calculate the dynamic aerodynamic loads, the velocity of the blade elements is required. Finally the aerodynamic loads are converted back to the global coordinate system.

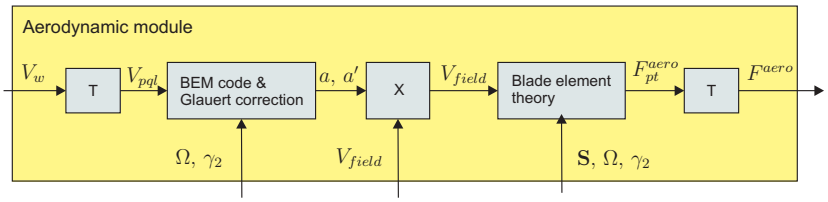

Figure 3.11: Aerodynamic module

The blade element theory is presented in section 3.6.1 and momentum theory in section 3.6.2. The BEM code is explained in section 3.6.3. Section 3.6.4 gives the calculation of the aerodynamic loads.

3.6.1 Blade element theory

The blade element theory describes the aerodynamic forces, lift L and drag D, on a blade element. A full blade consists of various types of airfoils with different characteristics.

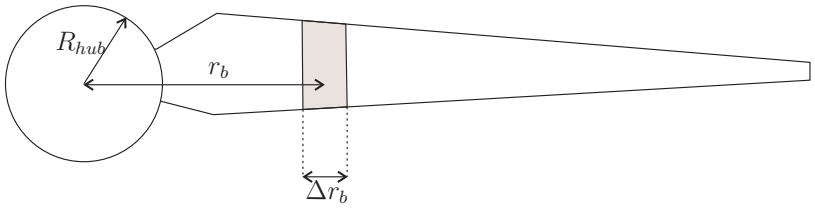

Figure 3.12: Blade element with length Δr_b

The lift and drag forces on a blade element depend on the type of airfoil, the air density, the resultant wind velocity and the surface of the blade element. The equations for the lift and drag forces on a blade element are

$$\Delta L = \frac{1}{2}\rho_{air} c W^2 C_l \Delta r_b \tag{3.5}$$

$$\Delta D = \frac{1}{2}\rho_{air} c W^2 C_d \Delta r_b \tag{3.6}$$

with

ρ_{air}	Air density
c	Airfoil chord length
W	Resultant wind velocity
C_l	2D lift coefficient
C_d	2D drag coefficient
α	Angle of attack
Δr_b	Length of the blade element

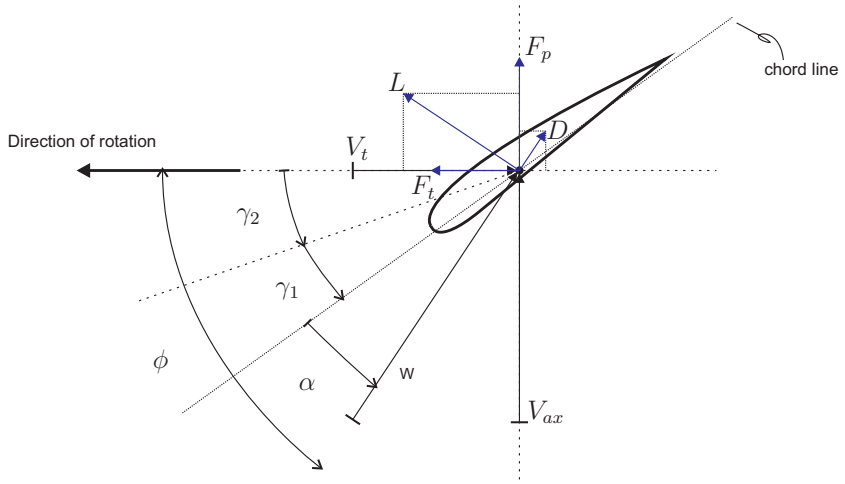

Figure 3.13: Airfoil cross-section with angles and forces

The aerodynamic wind velocity W is the vector sum of the perpendicular and tangential wind velocities on the blade element. The angle of inflow ϕ is the angle between W and V_t.

$$W = \sqrt{V_{ax}^2 + V_t^2} \tag{3.7}$$

and

$$\phi = \tan^{-1}(V_{ax}/V_t) \tag{3.8}$$

with

V_{ax}	Axial wind velocity at blade element in $\hat{p}$ direction
V_t	Tangential wind velocity at blade element in $\hat{t}$ direction
ϕ	Angle of inflow

The lift and drag coefficients of the airfoil are related to the angle of attack of the blade element. The angle of attack is the angle between the chord line and the resultant wind velocity W, which differs for each blade radius due to the twist distribution γ_1.

$$\alpha = \phi - \gamma_1 - \gamma_2 \tag{3.9}$$

with

α	Angle of attack
γ_1	Fixed twist angle
γ_2	Variable pitch angle

Every airfoil has its own characteristics depending on the $C_l(\alpha)$ and $C_d(\alpha)$ curves. With measurements on the airfoil the lift and drag coefficients are empirically determined for different angles of attack. The $C_l(\alpha)$ and $C_d(\alpha)$ curves of the airfoils on SWT 2.3-82.4 are not shown for confidentiality reasons. At certain airfoil thicknesses the curves are known. The thickness of an airfoil is given in percentages. For blade element thicknesses different from the given values, the coefficients are interpolated.
The perpendicular force F_p (Thrust) and tangential force F_t are expressed as a function of the drag and lift forces.

$$\Delta F_p = N_b(\Delta L \cos\phi + \Delta D \sin\phi) = \frac{1}{2}\rho_{air} W^2 N_b c (C_l \cos\phi + C_d \sin\phi)\Delta r \tag{3.10}$$

$$\Delta F_t = N_b(\Delta L \sin\phi - \Delta D \cos\phi) = \frac{1}{2}\rho_{air} W^2 N_b c (C_l \sin\phi - C_d \cos\phi)\Delta r \tag{3.11}$$

with

N_b	Number of blades

The torque is

$$\Delta Q = \Delta F_t r_b \tag{3.12}$$

with

r_b Blade element radius (see Figure 3.12)

The axial and tangential wind velocities are not identical to the free stream wind speed and the rotational speed, respectively. Due to the presence of the turbine these wind velocities are induced. The fractional decrease or increase of the wind velocity is represented by induction factors a and a'. The axial wind velocity is

$$V_{ax} = V_p(1 - a) \tag{3.13}$$

and the tangential wind velocity is

$$V_t = \Omega r(1 + a') \tag{3.14}$$

with

V_{ax} Wind velocity at the rotor disk position
V_p Undisturbed wind velocity perpendicular to rotor
a Axial induction factor
a' Tangential induction factor
Ω Angular velocity of rotor

3.6.2 Momentum theory

The momentum theory (or Rankine-Froude actuator-disk theory) is based on conservation laws. The principal use of the momentum theory is to obtain a first estimate of the wake-induced flow, and hence the total induced power loss. The rotor is replaced by an "actuator disk", which is a circular surface of zero thickness that can support a pressure difference decelerating the air through the disk. The assumptions on which the momentum theory is based are:

1. Homogenous steady wind
2. Incompressible wind flow (constant air density)
3. No obstruction to wind flow either upstream or downstream
4. Wind flow passing through disk separated from surrounding flow by stream-tube
5. Uniform wind at disk

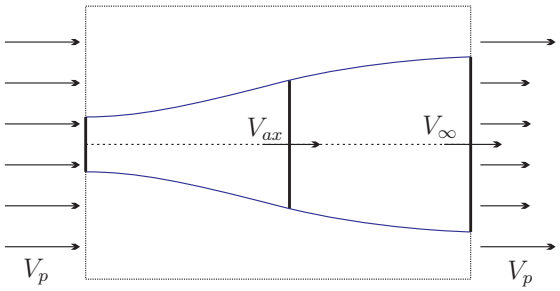

Figure 3.14: Stream tube

6. No rotation of flow produced by disk
7. Static pressure far upstream and far downstream of disk equal the undisturbed ambient pressure

Combining the mass continuity equations in the control volume for within and outside the stream-tube as shown in Figure 3.14, the momentum theory and the Bernoulli's principle give the equation for the rate of change of axial momentum of the air passing through the swept annulus. Hence the thrust

$$\Delta F_p = \frac{1}{2}\rho_{air} A_r (V_p^2 - V_\infty^2) \tag{3.15}$$

with

V_∞ Wind velocity far downstream in the wake
A_r Rotor disk area

Also

$$V_{ax} = \frac{1}{2}(V_p + V_\infty) \tag{3.16}$$

Thus, the velocity at the disk is the average of the upstream and downsteam velocties. Defining an axial induction factor a as the fractional decrease in wind velocity between the free stream and the disk, then

$$a = \frac{V_p - V_{ax}}{V_p} \tag{3.17}$$

and

$$V_{ax} = V_p(1-a) \tag{3.18}$$

Combining Eq. 3.16 and 3.18

$$V_\infty = V_p(1-2a) \tag{3.19}$$

Equation 3.19 implies that the momentum theory only holds for an induction factor lower than 0.5. For higher values the downstream velocity would be zero or negative. Combining Eq. 3.15 and 3.19 gives

$$\Delta F_p = 4\rho_{air}\pi V_p^2 a(1-a)r\Delta r \tag{3.20}$$

with the thrust coefficient

$$C_T = 4a(1-a) \tag{3.21}$$

For high induction factors ($a > 0.4$) Glauert's correction is applied

$$a = 0.143 + \sqrt{0.6427C_T - 0.55106} \tag{3.22}$$

For a more elaborate explanation of the momentum theory see section 3.3.2 of [9].

Angular momentum theory

The momentum theory can be extended to the case where the disk generates angular momentum, which can be related to rotor torque. When wake rotation is included the induced velocity at the rotor consists of not only the axial component but also a component in the rotor plane. The generation of rotational kinetic energy in the wake results in less extraction by the rotor than would be expected without wake rotation. Note that accros the flow disk, the angular velocity of the air relative to the blade increases from Ω to $\Omega + \omega$. The angular indcution factor a', is defined as

$$a' = \omega/\Omega \tag{3.23}$$

Applying the conservation of angular momentum, one can derive an expression for the rotor torque. The torque exerted on the rotor must equal the change in angular momentum.

$$\Delta Q = 4\rho_{air}\pi V_p \Omega r_b a'(1-a)r^2\Delta r_b \tag{3.24}$$

An elaborate explanation of the momentum theory with wake rotation is given in section 3.3 of [19].

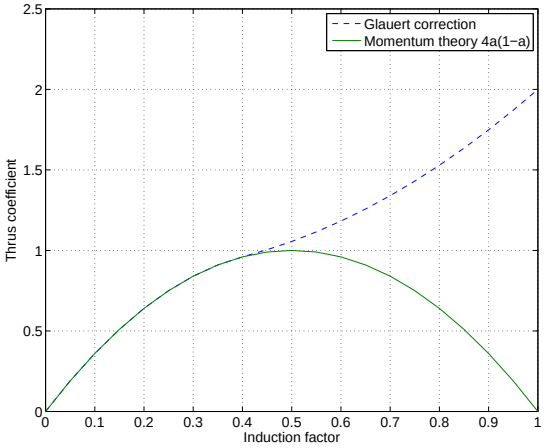

Figure 3.15: Glauert correction for high induction factor

3.6.3 BEM code

By combining the equations for the thrust and torque from momentum theory and blade element theory, the induction factors can be numerically estimated by the so called BEM code. Assuming equality of Eqs. 3.10 and 3.20 gives

$$C_T = 4a(1-a) = \frac{N_b c W^2 (C_l \cos\phi + C_d \sin\phi)}{2\pi r_b V_p^2} \tag{3.25}$$

Solving for a gives

$$a = \frac{1}{2} - \frac{1}{2}\sqrt{1 - C_T} \tag{3.26}$$

Assuming equality of Eqs. 3.12 and 3.24 gives

$$a' = \frac{W^2 N_b c (C_l \sin\phi - C_d \cos\phi)}{8\pi r_b^2 V_p \Omega} \tag{3.27}$$

When the inductions factors are known, the local aerodynamic loads on each blade element can be calculated. In the BEM code the following sequence of steps are taken

1. Set chord and twist distribution
2. Assume values for induction factors a and a'

3. Calculate the resultant wind velocity W with Eq. 3.7 and corresponding angle of inflow ϕ with Eq. 3.8
4. Find the angle of attack α using Eq. 3.9
5. Lookup the corresponding empirical coefficients C_l and C_d
6. Calculate C_T with Eq. 3.25 and solve for a using Eq. 3.26
7. Calculate a' with Eq. 3.27
8. Use the found a and a' as input to step 3 and repeat sequence untill convergence

3.6.4 Calculating the dynamic blade element forces

Now that the induced wind velocity at each blade element in time is known, the loads on each blade element can be calculated by

$$\Delta L = \frac{1}{2}\rho_{air} c C_l((V_{ax} - \dot{x}_p)^2 + (V_t - \dot{x}_t)^2)\Delta r_b \tag{3.28}$$

$$\Delta D = \frac{1}{2}\rho_{air} c C_d((V_{ax} - \dot{x}_p)^2 + (V_t - \dot{x}_t)^2)\Delta r_b \tag{3.29}$$

with

$\dot{x}_p$ Velocity of blade element in $\hat{p}$ direction, see Figure 3.1
$\dot{x}_t$ Velocity of blade element in $\hat{t}$ direction, see Figure 3.1

The aerodynamic force in $\hat{q}$ direction is

$$\Delta F_q^{aero} = -\Delta F_t \sin\alpha_{az} \tag{3.30}$$

The aerodynamic force in $\hat{l}$ direction is

$$\Delta F_l^{aero} = \Delta F_t \cos\alpha_{az} \tag{3.31}$$

The aerodynamic force vector with global coordinates on one blade element is

$$\Delta\vec{F}^{aero} = \begin{bmatrix} \Delta F_X^{aero} \\ \Delta F_Y^{aero} \\ \Delta F_Z^{aero} \end{bmatrix} = R_\theta R_\phi R_\psi \begin{bmatrix} \Delta F_p^{aero} \\ \Delta F_q^{aero} \\ \Delta F_l^{aero} \end{bmatrix} \tag{3.32}$$

The total aerodynamic moment vector is

$$\vec{M}^{aero} = \begin{bmatrix} M_x^{aero} \\ M_y^{aero} \\ M_z^{aero} \end{bmatrix} = \begin{bmatrix} x_b \\ y_b \\ z_b \end{bmatrix} \times \begin{bmatrix} F_x^{aero} \\ F_y^{aero} \\ F_z^{aero} \end{bmatrix} \tag{3.33}$$

3.7 Waves module

The outputs of the waves module are the translations, velocities and accelerations of the wave particles at the spar in the global coordinate system. In section 2.2 it was assumed that the wave description is deterministic, being a single regular wave with constant wave height H_w. The inputs to the wave module are the time t and the DOF solver output $\mathbf{S}$. With $\mathbf{S}$, the position of the spar $\vec{r}_{spar}$ in the global coordinate system can be calculated by transformations. Airy's linear wave theory [17] calculates the wave particle motion, which is the output of the wave module.

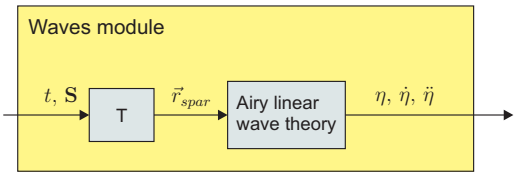

Figure 3.16: Structure of waves module. Time t; $\mathbf{S}$ contains the position, velocity, orientation and angular velocity of cg; the position vector of the spar sections $\vec{r}_{spar}$; the wave position, velocity and acceleration η, $\dot{\eta}$ and, $\ddot{\eta}$.

Airy's linear wave theory [17] describes wave particle motion in undisturbed deep waters. The theory assumes that the fluid layer has a uniform mean depth and that the fluid flow is inviscid, incompressible and irrotational. This theory was first published, in correct form, by George Biddell Airy in the 19th century. A single regular wave has an amplitude U_a, frequency ω_w and phase α_w. The translation of the wave particle in the direction of the wave

$$\eta_h = U_a \cos(\alpha_w - \omega_w t) \tag{3.34}$$

The wave elevation in Z direction

$$\eta_Z = -U_a \sin(\alpha_w - \omega_w t) \tag{3.35}$$

with

η_h	Translations of wave particle in direction of the wave
η_Z	Wave translation in Z direction
U_a	Wave amplitude
α_w	Wave phase
ω_w	Wave frequency
t	Time

The translations in X, Y are found by simple geometric calculations.

$$\eta_X = \eta_h \cos(\beta_{wave}) \tag{3.36}$$

$$\eta_Y = \eta_h \sin(\beta_{wave}) \tag{3.37}$$

where β_{wave} is the wave angle with respect to the global coordinate system as presented in Figure 3.17. The wave particle translation vector is

$$\vec{\eta} = \begin{bmatrix} \eta_X \\ \eta_Y \\ \eta_Z \end{bmatrix} \tag{3.38}$$

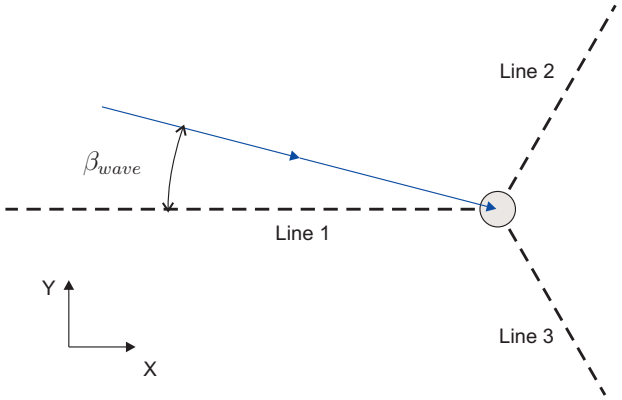

Figure 3.17: Wave angle with respect to the global coordinate system

The wave amplitude U_a is a function of the water depth d and depends on the wave height H_w and the wave number k_w. The wave number $k_w = \frac{2\pi}{\lambda_w}$, where λ_w is the wave length in meters.

$$U_a = \frac{1}{2} H_w e^{-k_w d} \tag{3.39}$$

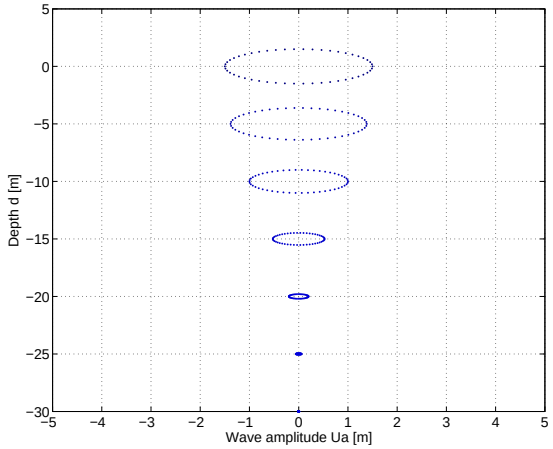

Figure 3.18: Exponential decrease of wave amplitude U_a with depth d for $H_w = 3$ m. The motion of the wave particle is circular, but looks eliptical due to the scaled axes.

The amplitude decreases exponentially with increasing depth (Figure 3.18). When $d = 0$, $U_a = \frac{1}{2}H_w$. At large depths ($d < 50$) U_a is negligible even for large waves. When the spar moves away from its original position the wave at the spar will have a phase difference which depends on the translation of the spar as shown in Figure 3.19. The wave phase differences is

$$\alpha = k_w\, s \tag{3.40}$$

with s the horizontal translation of the spar section in the direction of the wave. Figure 3.19 illustrates how the phase shift can be found with some simple geometric calculations. The translation s depends on the new position of the spar section and the wave angle β_{wave} by

$$s_i = \sqrt{X_i^2 + Y_i^2}\cos(\tan^{-1}(Y/X) - \beta_{wave}) \tag{3.41}$$

The velocity and acceleration of the wave particle are the first and second derivative of the particle translation, respectively

$$\dot{\vec{\eta}} = \frac{\partial \vec{\eta}}{\partial t} \tag{3.42}$$

$$\ddot{\vec{\eta}} = \frac{\partial^2 \vec{\eta}}{\partial t^2} \tag{3.43}$$

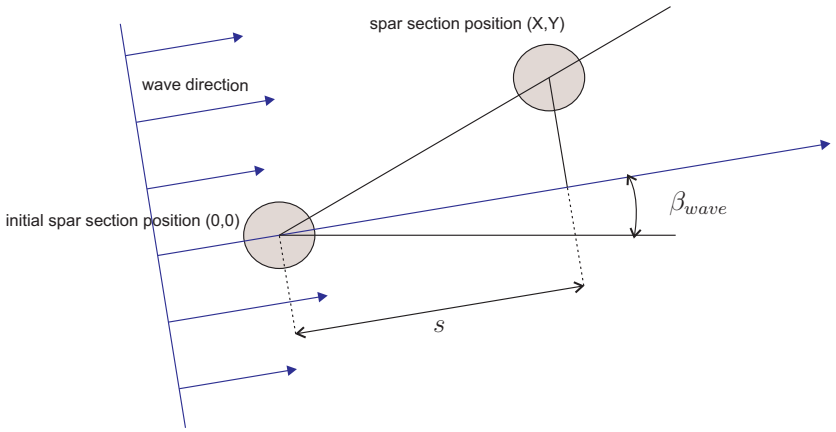

Figure 3.19: Determination of the wave distance s to calculate the wave phase α with Eq. 3.40

3.8 Hydrostatic & hydrodynamic module

The outputs of the hydrostatic & hydrodynamic module are the loads from buoyancy, waves, sea current and hydrodynamic damping. The structure of the module is presented in Figure 3.20. The inputs to the module are **S** and wave information.

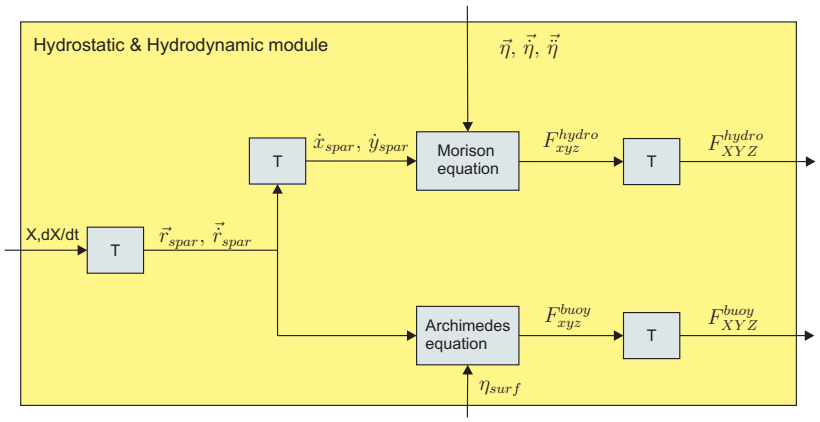

Figure 3.20: Hydrodynamic module

Section 3.8.1 explains the buoyancy force and section 3.8.2 presents the wave,

current and hydrodynamic damping loads.

3.8.1 Buoyancy

Archimedes' law states that the net upward force on a floating object equals the weight of the displaced fluid. This upward force is called the buoyancy force. Archimedes' law holds for any kind of liquid. In this case we consider sea water with a density of 1025 kg/m^3. In still water when the translations and rotations are zero

$$F_b = \rho_{sea}\, g\, V_{displ}$$

with

F_b	Buoyancy force
ρ_{sea}	Sea water density
g	Gravitational acceleration
V_{displ}	Displaced water volume when $u_Z = 0$
u_Z	Translation in Z-direction in global coordinate system

The total buoyancy force acts through the center of buoyancy *cb* in Z direction as shown in Figure 3.21.

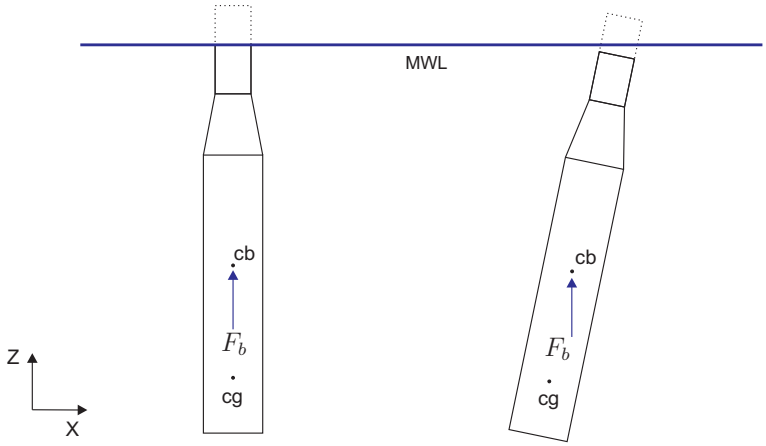

Figure 3.21: Net upward buoyancy force acting through *cb*

When the turbine rises or sinks, the displaced water volume decreases or increases, respectively. In still water

$$F_b = \rho_{sea}\, g\, (V_{displ} - A_{surf}\, u_Z)$$

with

A_{surf} Constant spar area at water surface with 6.0 m diameter

The surface wave elevation η_{surf} similarly affects the buoyancy force.

$$F_b = \rho_{sea}\, g\, (V_{displ} - A_{surf}\, u_Z + A_{surf}\, \eta_{surf}) \tag{3.44}$$

with

η_{surf} Wave elevation at surface

The buoyancy force changes linearly with the surface wave elevation and the vertical translation. It therefore acts as a spring force. Eq. 3.44 holds for vertical translations between $-11 < z < 4.5$. For larger translations the spar area changes. The rotations will also affect the volume of displaced water changing the buoyancy force. For small angles this affect is minor and neglected.

The displaced water volume is divided in three parts with different cross sections. Figure 3.22 shows the dimensions of the substructure. The upper and bottom parts, 1 and 3, have constant diameters of 6 and 8.3 m, respectively. The middle part has a conical shape varying linearly from from a 6 to 8.2 m diameter.
The center of buoyancy *cb* is the center of mass of the displaced water volume. The location of *cb* determines the restoring moment of the buoyancy force. In still water without translations, when $u_Z = 0$ m, *cb* lies at $z = 25.65$ m. Waves and translations of the turbine affect the location of *cb*. The following equation calculates the center of mass of the displaced water, hence

$$cb = \frac{V_1 r_1 + V_2 r_2 + V_3 r_3}{V_1 + V_2 + V_3} \tag{3.45}$$

and

$$V_1 = A_{surf}(4.5 - u_Z + \eta_{surf}) \tag{3.46}$$

and

$$r_1 = \frac{1}{2}(4.5 - u_Z + \eta_{surf}) + 89 + 6.5 \tag{3.47}$$

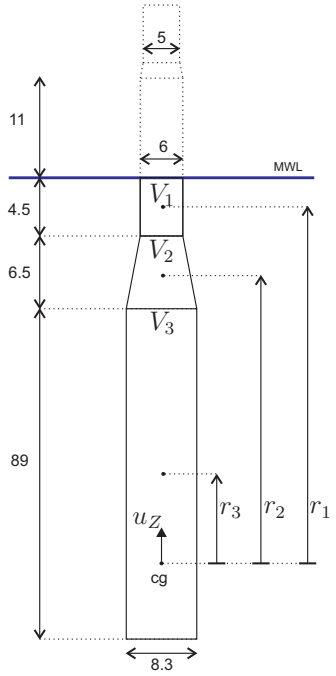

Figure 3.22: Calculating the center of buoyancy *cb*

with

V_1	Volume of the displaced water of spar part 1
V_2	Volume of the displaced water of spar part 2
V_3	Volume of the displaced water of spar part 3
r_1	Distance from center of mass of part 1 to *cg*
r_2	Distance from center of mass of part 2 to *cg*
r_3	Distance from center of mass of part 3 to *cg*

Again, Eq. 3.45 holds for vertical translations between $-11 < u_Z < 4.5$. Out of these values, the surface spar area changes, see Figure 3.22. When u_Z increases with 1.0 m, *cb* decreases with approximately 0.71 m.

3.8.2 Wave, current and damping loads

Kinetic energy of the moving water is passed to the substructure. The motion of a water particle is caused by waves and current. The motion of the platform itself influences the relative water particle motion. The superposition of these motions results in the relative velocity and acceleration of a water particle.

Hydrodynamic loads on the sides of the spar

In chapter 2 it is stated that the hydrodynamic loads on sides of the spar are calculated with Morison's equation [21]. Morison's equation relates to the water particle velocity and acceleration. Since these differ over the spar, the hydrodynamic loads are not equally distibuted over the surface of the cylindrical spar. Therefore, the substructure is divided into a number of sections. Morison's equation consists of a drag force and an inertia force with certain drag and inertia coefficients

$$\vec{F}_{xy}^{hydro} = \vec{F}_{xy}^{drag} + \vec{F}_{xy}^{inertia} \tag{3.48}$$

with

$\vec{F}_{xy}^{hydro}$	The hydrodynamic force vector on the side
$\vec{F}_{xy}^{drag}$	The hydrodynamic drag force vector on the side
$\vec{F}_{xy}^{inertia}$	The hydrodynamic inertia force vector on the side

The drag force is a viscous force related to velocity squared, the water density, the object's surface and the drag coefficient C_d. C_d is not a constant but varies as a function of speed, flow direction, object shape, object size, fluid density and fluid viscosity. Speed, kinematic viscosity and a characteristic length scale of the object are incorporated into a dimensionless quantity called the Reynolds number or Re. Cd is thus a function of Re. The drag coefficient for a cylindrical object is assumed contant $C_d = 0.6$ [22]. When the spar is inclined, the horizontal cross section of the spar changes from cylindrical to elliptical in the horizontal plane, changing the drag coefficient.

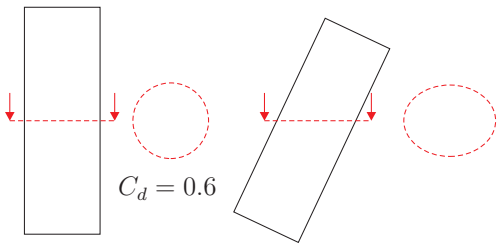

Figure 3.23: Hydrodynamic drag coefficients

The velocity and acceleration of the wave particle, current and spar are all converted from the global coordinate system to the first local coordinate system as illustrated in Figure 3.1). This implies that the local velocities are either perpendicular or parallel to the spar. The perpendicular velocity vectors $\dot{x}_s$ and $\dot{y}_s$

encounter a cylindrical cross-section with a drag coefficient of 0.6. The friction forces on the sides caused by the velocity vectors $\dot{z}_s$ are neglected. Figure 3.24 shows the transformation of the velocity vectors from the global to the first local coordinate system.

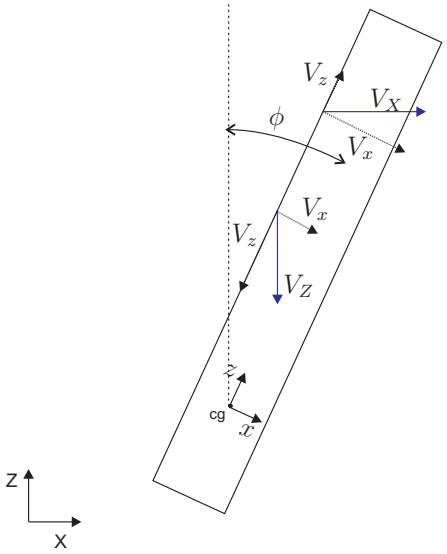

Figure 3.24: Hydrodynamic velocity transformations

The following equations are the loads in the x direction, but can also be used in the y direction. The drag term ΔF_x^{drag} on a spar section in the x direction is

$$\Delta F_x^{drag} = \frac{1}{2}\rho_{sea} C_D D(\dot{\xi}_x + c_x - \dot{x}_s)\left|\dot{\xi}_x + c_x - \dot{x}_s\right|\Delta z_s \tag{3.49}$$

with

C_D	Local drag coefficient
D	Local spar diameter
$\dot{\eta}x$	Local velocity of wave particle in x direction
c_x	Local constant current velocity in x direction
$\dot{x}_s$	Local velocity of spar in x direction
Δz_s	Unit length of spar section

The inertia term is related to acceleration. The acceleration of the water particles and spar are also transformed from the global to the first local coordinate system.

The intertia force on a spar section is

$$\Delta F_x^{inertia} = \rho_{sea} A_s (C_m \ddot{\xi}_x - C_a \ddot{x}_s) \Delta z_s \tag{3.50}$$

with

C_m	Inertia coefficient $C_m = 1 + C_a$ [18]
C_a	Added mass coefficient
$\ddot{\xi}_x$	Local acceleration of wave particle in x direction
$\ddot{x}_s$	Local acceleration of spar in x direction
A_s	Cross-section area of spar section

The inertia equation is separated in two terms. The spar section acceleration corresponds to the added mass coefficient C_a and the wave particle acceleration to the inertia coefficient C_m. In fluid mechanics, added mass is the inertia added to a system. This is because an accelerating or decelerating body must move some volume of surrounding fluid as it moves through it. The object and fluid cannot occupy the same physical space simultaneously. The added mass creates an 'extra' force needed to give the platform a unit acceleration. The dimensionless added mass coefficient C_a is often empirically estimated and is a value between 0 and 1. The value estimated for Hywind by OC3 is 0.97 for all spar cross sections [22].

When the Morison equation is placed in the equations of motion of section i, the forces are transformed to the global coordinate system with transformation matrix T.

$$\Delta m \ddot{x}_s = \Delta F_x^{drag} + \Delta F_x^{inertia} \tag{3.51}$$

with

Δm	Mass of spar section

Combining Equations 3.50 and 3.51

$$\Delta m \ddot{x}_s = F_x^{drag} + \rho_{sea} A_s (C_m \ddot{\eta}_x - C_a \ddot{x}_s) \Delta z \tag{3.52}$$

The term $\ddot{x}_s$ is on both sides of Equation 3.52. Moving $\ddot{x}_s$ to the left side results in

$$(\Delta m + \Delta m_{a1}) \ddot{x}_s = \Delta F_x^{drag} + \rho_{sea} A_s C_m \ddot{\eta}_x \Delta z \tag{3.53}$$

where Δm_{a1} is the translational added mass of the spar section side

$$\Delta m_{a1} = \rho_{sea} A_s C_a \Delta z \tag{3.54}$$

The full translational added mass of the spar side equals

$$m_{a1} = C_a \rho_{sea} V_{displ} \tag{3.55}$$

The added mass term is removed from the Morison equation and added to the mass of the system. Therefore the hydrodynamic force in x direction is

$$\Delta F_x^{hydro} = \Delta F_x^{drag} + \rho_{sea} A_s C_m \ddot{\eta}_x \Delta z \tag{3.56}$$

F_x^{hydro} is transformed to global coordinates as explained in Appendix C and shown in Figure 3.25.

$$\vec{F}_{side}^{hydro} = \begin{bmatrix} F_X^{hydro} \\ F_Y^{hydro} \\ F_Z^{hydro} \end{bmatrix} = R_\theta R_\phi R_\psi \begin{bmatrix} F_x^{hydro} \\ F_y^{hydro} \\ 0 \end{bmatrix} \tag{3.57}$$

The hydrodynamic moment vector is

$$\vec{M}^{hydro} = \begin{bmatrix} M_x^{hydro} \\ M_y^{hydro} \\ M_z^{hydro} \end{bmatrix} = \begin{bmatrix} 0 \\ 0 \\ z_s \end{bmatrix} \times \begin{bmatrix} F_x^{hydro} \\ F_y^{hydro} \\ 0 \end{bmatrix} \tag{3.58}$$

Placing the hydrodynamic moments in the equations of motions results in

$$(\Delta I_{yy} + \Delta I_a)\, \dot{\omega}_y = M_y^{hydro} \tag{3.59}$$

When putting $\ddot{x}_s = \dot{\omega}_y\, z_s$ in Eq. 3.59, then the rotational added mass is

$$\Delta I_a = C_a\, \rho_{sea}\, A_s\, z_s^2\, \Delta z \tag{3.60}$$

ΔI_{yy}	Moment of inertia of spar section around y axis
ΔI_a	Rotational added mass of spar section
$\dot{\omega}_y$	Angular acceleration of spar section around y axis

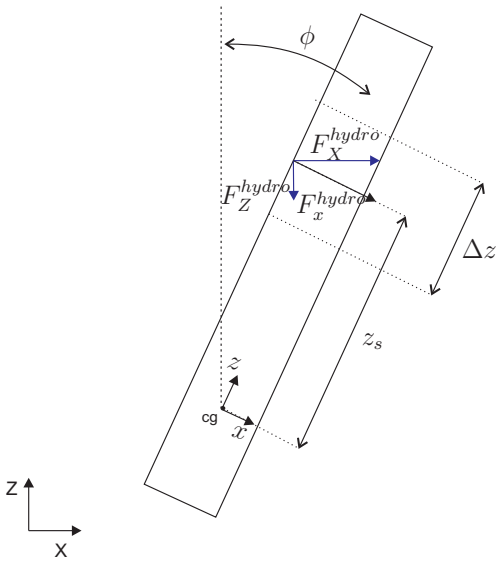

Figure 3.25: Transforming the hydrodynamic loads to the global coordinate sytem

Hydrodynamic loads on the bottom of the spar

The hydrodynamic loads in z direction act on the bottom plate. Friction along the side is neglected. The bottom plate lies around a depth of 100 m. At this depth wave loads can be neglected as shown in 3.18. The hydrodynamic force on the bottom consists of the Morison inertia term and a linear damping term

$$F_z^{hydro} = -m_a^2 \ddot{z}_s - C_{bot} \dot{z}_s \tag{3.61}$$

with

m_a^2	Added mass of the bottom
C_{bot}	Damping coefficient of the bottom plate [kg/s]

Conservatively assumed the vertical added mass below a floating object equals approximately the mass of half a sphere of water below the object [18], as shown in Figure 3.26.

$$m_{a2} = \frac{1}{3} \rho_{sea} D_{bot}^3 \tag{3.62}$$

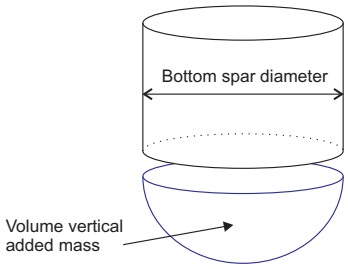

Figure 3.26: The bottom added mass of a vertical cylinder

where D_{bot} is the diameter at the bottom of the spar. Transforming the bottom force to global coordinates results in

$$\vec{F}_{bot}^{hydro} = R_\theta R_\phi R_\psi \begin{bmatrix} 0 \\ 0 \\ F_z^{hydro} \end{bmatrix} \tag{3.63}$$

The total hydrodynamic force vector is

$$\vec{F}^{hydro} = \vec{F}_{side}^{hydro} + \vec{F}_{bot}^{hydro} \tag{3.64}$$

3.9 Mechanical module

Section 3.9.1 presents how the structural body is modeled considering masses, inertias, kinematics and transformations. Section 3.9.2 and 3.9.3 explain the calculation on the mooring and gyroscopic loads for the mechanical module. Figure 3.27 illustrates the structure of the mechanical module. The inputs to the module are $\mathbf{S}$ and the rotor angular velocity Ω. The outputs are the mooring loads and gyroscopic moments.

3.9.1 Structural body

Section 2.2 assumed a rigid body as a point mass moving with the center of mass cg. The fixed center of mass is positioned 32 m above the spar bottom. When the body is in equilibrium without external forces applied, then $cg = -68.0$ m below MWL. The equations of motion are solved around cg. This requires moment of inertias around cg. Therefore the inertias of the rotor, tower and spar are converted to cg and summed up.

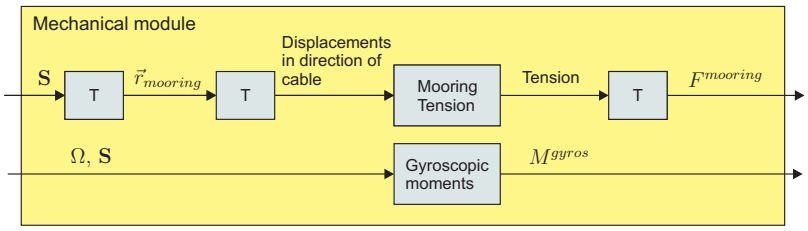

Figure 3.27: Structure of mechanical module

When a body is infinitely stiff, the positions, velocities and accelerations of all the points on the body can be calculated by kinematics. Appendix C presents the kinematics and transformations used in A.T.FLOW.

The total gravitational force vector acting through the center of mass is

$$\vec{W} = \begin{bmatrix} 0 \\ 0 \\ -mg \\ 0 \\ 0 \\ 0 \end{bmatrix} \tag{3.65}$$

3.9.2 Mooring loads

Section 2.2 assumed a quasi-static mooring system. Therefore the dynamics of the mooring system are neglected.

Translational stiffness of the mooring system

The quasi-static reaction force of a single mooring line depends nonlinearly on the platform displacements. This load-displacement relation was calculated by StatoilHydro for the Hywind mooring system and the results are presented in Figure 3.28.

The mooring line tension consists of a horizontal and vertical component. When the horizontal distance between the anchor and the fairlead decreases, the tension in the line also decreases. The vertical component is larger than the horizontal component, because the line is bend. When the distance increases, the tension increases and the horizontal component is larger, because the line is taut.

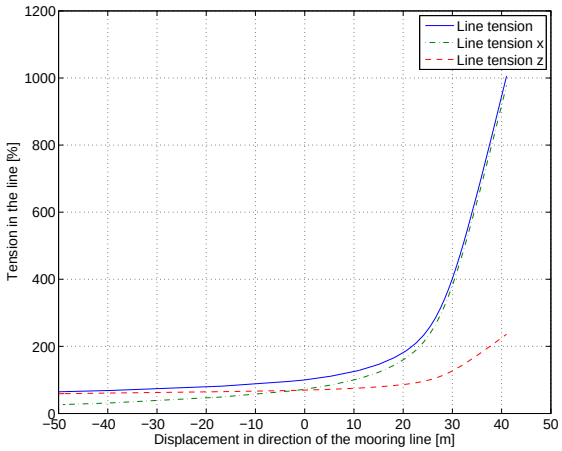

Figure 3.28: Normalized tension in a single mooring line for different fearlead displacements. Normalized by dividing the data with the net tension in the line at a zero displacement. Therefore the value is 100% at a zero displacement.

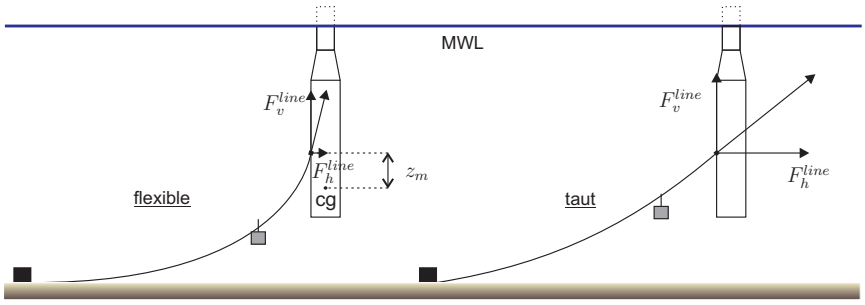

Figure 3.29: Horizontal and vertical component of tension

Above a positive displacement of 20m the tension rises dramatically as the mooring line gets more and more taut. This can be seen in Figure 3.28. The largest

nonlinearities occur for horizontal displacements between 0 and 30 m. The mooring line angles β^{line} are illustrated in Figure 3.30.

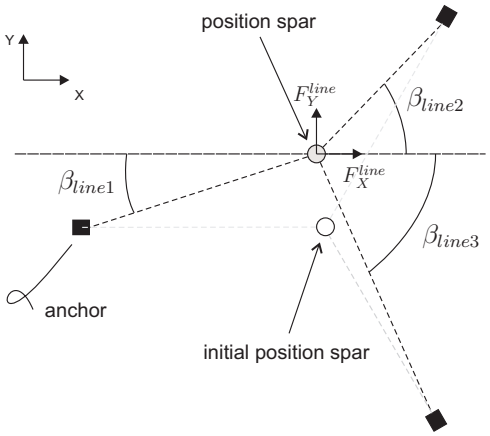

Figure 3.30: Mooring line angles and net forces

The mooring reaction forces are

$$F_X^{line} = F_{h1}^{line}\cos(\beta_{line1}) + F_{h2}^{line}\cos(\beta_{line2}) + F_{h3}^{line}\cos(\beta_{line3}) \tag{3.66}$$

and

$$F_Y^{line} = F_{h1}^{line}\sin(\beta_{line1}) + F_{h2}^{line}\sin(\beta_{line2}) + F_{h3}^{line}\sin(\beta_{line3}) \tag{3.67}$$

and

$$F_Z^{line} = F_{v1}^{line} + F_{v2}^{line} + F_{v3}^{line} \tag{3.68}$$

with

F_h^{line}	Horizontal mooring line tension
F_v^{line}	Vertical mooring line tension
F_X^{line}	Total mooring line force in X direction
F_Y^{line}	Total mooring line force in Y direction
F_Z^{line}	Total mooring line force in Z direction
β^{line}	Mooring line angle

The mooring force vector is

$$\vec{F}^{mooring} = \begin{bmatrix} F_X^{line} \\ F_Y^{line} \\ F_Z^{line} \end{bmatrix} \tag{3.69}$$

and the moment vector is

$$\vec{M}^{mooring} = \begin{bmatrix} 0 \\ 0 \\ z_m \end{bmatrix} \times \begin{bmatrix} F_x^{line} \\ F_y^{line} \\ F_z^{line} \end{bmatrix} + \begin{bmatrix} 0 \\ 0 \\ M_z^{mooring} \end{bmatrix} \tag{3.70}$$

Angular stiffness

The results for the yaw moment $M_z^{mooring}$ from Statoil are presented in Figure 3.31.

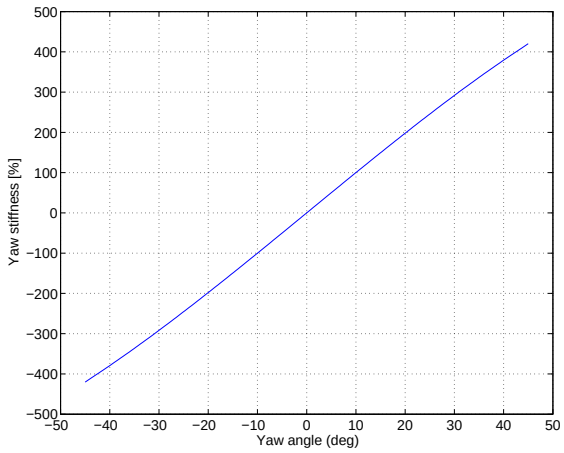

Figure 3.31: Normalized mooring yaw stiffness. Normalized by dividing the data with the mooring yaw moment at a yaw angle of 10 deg. Therefore the value is 100% at a yaw angle of 10 deg.

For a known displacement in time the corresponding quasi-static reaction force and yaw stiffness is looked up from figures 3.28 and 3.31.

3.9.3 Gyroscopic effect

The rotation of the rotor causes gyroscopic moments. The gyroscopic moment vector is [23]

$$\vec{M}^{gyros} = -I^r_{xx}\Omega \begin{bmatrix} 0 \\ \omega_z \\ \omega_y \end{bmatrix} \tag{3.71}$$

with

$\vec{M}^{gyros}$	Gyroscopic moment vector
I^r_{xx}	Moment of inertia about x axis
Ω	Angular velocity of the rotor
ω_z	Body angular velocity around z axis
ω_y	Body angular velocity around y axis

3.10 DOF Solver

The equations of motion which are solved in time are ordinary differential equations. MATLAB has build-in functions that integrate and solve the system of differential equations for a given time period with initial conditions. The function used for this model is the commonly used ode45 solving first order linear or non-linear differential equations. This routine uses a variable step Runge-Kutta Method to solve differential equations numerically.

3.10.1 Equations of Motion

The three force equations of motion are

$$\mathbf{M}\,\vec{\ddot{r}} = \vec{f} = \vec{W} + \vec{F}^{aero} + \vec{F}^{hydro} + \vec{F}^{mooring} \tag{3.72}$$

with

$\mathbf{M}$	Mass matrix
$\vec{\ddot{r}}$	Translational acceleration vector
$\vec{f}$	Total external force vector
$\vec{W}$	Weight vector (Eq. 3.65)
$\vec{F}^{aero}$	Aerodynamic force vector (Eq. 3.32)
$\vec{F}^{hydro}$	Hydrostatic and hydrodynamic force vector (Eq. 3.64)
$\vec{F}^{mooring}$	Mooring force vector (Eq. 3.69)

The external load vectors F were given in the previous sections. The matrix $\mathbf{M}$ contains

$$\mathbf{M} = \begin{bmatrix} m + m_{a1} & 0 & 0 \\ 0 & m + m_{a1} & 0 \\ 0 & 0 & m + m_{a2} \end{bmatrix} \tag{3.73}$$

The translational acceleration vector $\vec{\ddot{r}}$ is

$$\vec{\ddot{r}} = \begin{bmatrix} \ddot{X} \\ \ddot{Y} \\ \ddot{Z} \end{bmatrix} \tag{3.74}$$

and total external force vector

$$\vec{f} = \begin{bmatrix} F_X \\ F_Y \\ F_Z \end{bmatrix} \tag{3.75}$$

The three moment equations of motions are

$$\mathbf{I}\,\vec{\dot{\omega}} = \vec{M}^{aero} + \vec{M}^{hydro} + \vec{M}^{mooring} + \vec{M}^{gyros} \tag{3.76}$$

with

$\mathbf{I}$	Moment of inerta matrix
$\vec{\dot{\omega}}$	Angular acceleration vector
$\vec{M}^{aero}$	Aerodynamic moment vector (Eq. 3.33)
$\vec{M}^{hydro}$	Hydrostatic and hydrodynamic moment vector (Eq. 3.58)
$\vec{M}^{mooring}$	Mooring moment vector (Eq. 3.70)
$\vec{M}^{gyros}$	Gyroscopic moment vector (Eq. 3.71)

The matrix $\mathbf{I}$ contains

$$\mathbf{M} = \begin{bmatrix} I_{xx} + I_a & 0 & 0 \\ 0 & I_{yy} + I_a & 0 \\ 0 & 0 & I_{zz} \end{bmatrix} \tag{3.77}$$

The rotational acceleration vector $\vec{\dot{\omega}}$ is

$$\vec{\dot{\omega}} = \begin{bmatrix} \dot{\omega}_x \\ \dot{\omega}_y \\ \dot{\omega}_z \end{bmatrix} \tag{3.78}$$

3.10.2 Solver outputs

For every timestep dT the solver function ode45 gives the output $\mathbf{S}$.

$$\mathbf{S} = \begin{bmatrix} X \\ \dot{X} \\ Y \\ \dot{Y} \\ Z \\ \dot{Z} \\ \theta \\ \dot{\theta} \\ \phi \\ \dot{\phi} \\ \psi \\ \dot{\psi} \end{bmatrix} \tag{3.79}$$

with

X	Surge displacement of cg
$\dot{X}$	Surge velocity of cg
Y	Sway displacement of cg
$\dot{Y}$	Sway velocity of cg
Z	Heave displacement of cg
$\dot{Z}$	Heave velocity of cg
θ	Euler angle, roll
$\dot{\theta}$	Roll angular velocity
ϕ	Euler angle, pitch
$\dot{\phi}$	Pitch angular velocity
ψ	Euler angle, yaw
$\dot{\psi}$	Yaw angular velocity

Part II

Verification and predictions

Chapter 4

Model verification

Section 4.2 verifies the theory used for the wave loads by comparing it to results from SIMO/RIFLEX. Section 4.3 presents the verification of the restoring characteristics using pullout tests from SIMO/RIFLEX. Section 4.4 verfies the hydrodynamic damping using decay tests from SIMO/RIFLEX. Section 4.5 verifies the aerodynamic performance of SWT 2.3-80 comparing to BHawC calculations.

4.1 Introduction

This chapter performs task 3 of the problem formulation, the verification of the model. Task 4, validation by using measurement data, is not part of this thesis. The verification procedure consists of

- Comparison to other verified models
- Providing a solid scientific basis
- Good and clear explanation of the model to build confidence

The verification of the second and third items are part of Chapter 3. This chapter presents the verification by the first item, comparing to results from verified models. This verification procedure depends on the availability of results from other models. During this thesis the following was available for comparison

- Wave force representation
- Restoring stiffness of the system
- Hydrodynamic damping characteristics of the substructure
- Aerodynamic performance of SWT 2.3-80

4.2 Wave force representation

Using SIMO/RIFLEX, Statoil calculated the total wave force of a regular wave on the side of the submerged spar and the total wave moment around mean water level (MWL). The total wave force is the summation of the wave forces on the spar sections. The total moment is the summation of the moments around MWL of the spar sections. During the calculations the spar is static and not inclined. The results from SIMO/RIFLEX are compared to the results from A.T.FLOW Morison equation is used for the wave load calculations (Eq. 3.48). SIMO/RIFLEX is a conservative hydrodynamic model giving accurate results. When the results of A.T.FLOW correspond to the results of SIMO/RILFEX, the usage of Morison's equation is verified.

First, the results of the regular wave at MWL are compared in Figure 4.1. The regular wave has a constant wave height of 4 m. The results from SIMO/RIFLEX show a irregular wave at the startup. From $t = 30$ sec, the wave of SIMO/RIFLEX is regular. This difference is probably caused by initial conditions of SIMO/RIFLEX. Anyhow, it nicely shows the correctness of te wave elevation of A.T.FLOW.

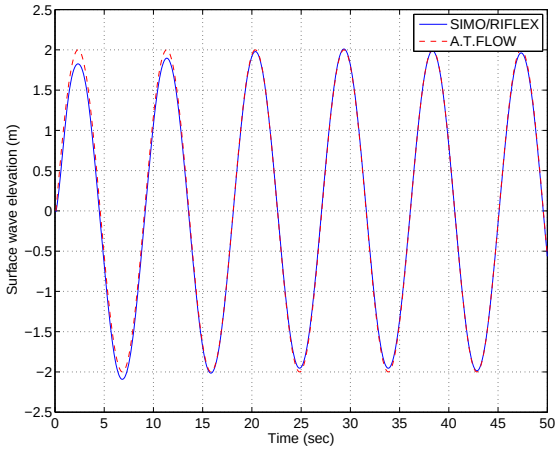

Figure 4.1: Wave elevation at MWL

Figures 4.2 and 4.3 show the total wave force and moment on the submerged spar. The total force and moment are the integration of the forces and moments on all the spar sections. For $t < 30$ sec, the results of the total force and moment can not correspond. However, when the wave elevations match for $t > 30$ sec, the results of the total wave force and moment should coincide. Figures 4.2

and 4.3 confirm this. The similarity of the results verifies the use of Morison's equation and implies a correct force and moment integration. The accuracy of the total wave moment implies that the moment arms of each spar section are implemented correctly.

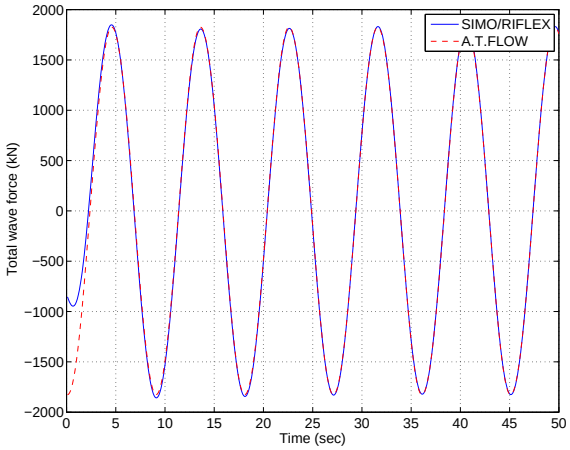

Figure 4.2: Total wave force on side of submerged spar

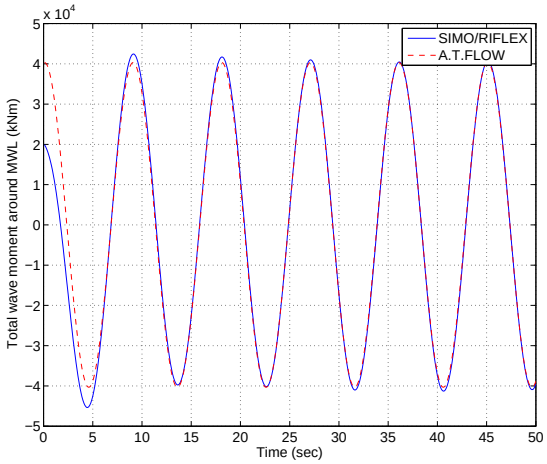

Figure 4.3: Total wave moment around MWL

4.3 The restoring stiffness of the system

The restoring stiffness indicates the resistance of the system in relation to displacement or rotation. This translational stiffness depends on the system mass and the net mooring force. The rotational stiffness is caused by the system moment of inertia and the net restoring moment from the gravitational force, the buoyancy force and the mooring force. The restoring stiffness can be tested by a pull-out.

The system is pulled into a degree of freedom by applying a constant force or moment in that direction. The calculations are done in a situation of still water and no wind. The force is applied at the center of mass *cg* and the moment around *cg*. When the constant load is applied for some time, the system will converge to an offset. At this point the applied force equals the total mooring force in surge direction. A small load causes a small offset and a large load causes a large offset. The relation between load and offset shows the restoring stiffness for each degree of freedom. Statoil executed a pull-out case using SIMO/RIFLEX. The results of the pull-outs in surge and roll are presented in Figures 4.4 and 4.5, respectively.

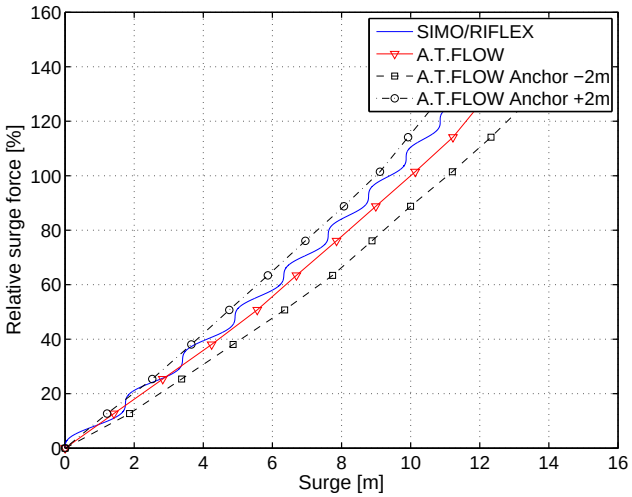

Figure 4.4: Pull-out in surge normalized wrt the value of A.T.FLOW at 10 m. Therefore the value at 10 m offset is 100%.

Figures 4.4 shows ripples in the curve of SIMO/RIFLEX. This is because the results of SIMO/RIFLEX are calculated in a different way. Instead of letting the system converge to a new position when applying a constant force, the reaction force and displacement is monitored in time. Therefore te dynamics of

the system are included in the results. But when this is done very slowly, the dynamics are negligible. However, the results of SIMO/RIFLEX in Figure 4.4 do show some dynamics, expressed in the humps in the curve. The method of SIMO/RIFLEX is faster, but gives less accurate results since dynamic behaviour is included. The results of SIMO/RIFLEX and A.T.FLOW seem to correspond, but to indicate the sensitivity of the A.T.FLOW results, critical parameters should be varied. The parameters that influence the surge load-displacement relation are the mooring characteristics (mooring weight, line stiffness, line length and distance between fairlead and anchor). The only parameter which is used in A.T.FLOW is the distance between the fairlead and the anchor. The other structural parameters can therefore not be varied. The distance towards the anchor is varied to determine its sensitivity. The curves indicated with a cirle and square are results from A.T.FLOW with an anchor positioned either 2 m further of or closer to the turbine. When the anchor is too close the displacement is larger. When the anchor is closer the displacement is smaller. The influence of the anchor positions is great. It can be stated that A.T.FlOW has an acceptable anchor position error of 1.0 m.

Figures 4.5 and 4.6 show the pitch load-displacement of A.T.FLOW and SIMO RIFLEX. The rotational restoring stiffness depends on the restoring moments caused by the gravitational force, the buoyancy force and the mooring force. These moments depend on the locations their forces act on, which are cg, cb and the fairlead position cm. The moment is taken around cg. Therefore the gravitational moment is zero. Varying cb and cm shows the sensitivity of these parameters on the results.

The design locations of these parameters are $z_{cb} = 15.6$ m and $z_{cm} = 14.8$. It is to be expected that when z_{cb} and z_{cm} are higher, the restoring moment is higher and the healed angle is lower. When the turbine is designed to have cb positioned 2.0 m lower, the roll angle increases with 15%. The other way around, the roll angle decreases with 15%. When the mooring fairlead is placed 10.0 m lower, the roll angle increases with 3%. The other way around, the roll angle decreases with 3%. So, the parameter z_{cb} has more influence on the angular stiffness than z_{cm}. This is because the buoyancy force is much larger. With the parameters placed at their design positions, the results of SIMO/RIFLEX and A.T.FLOW correspond with an accuracy of $z_{cb} \simeq 0.3$ m. To move cb two meter up, the diameter of the substructure must be increased from 8.3 m to 10.9 m, hence an increase of 2.6 m.

The other pull-out results are given in Appendix D.

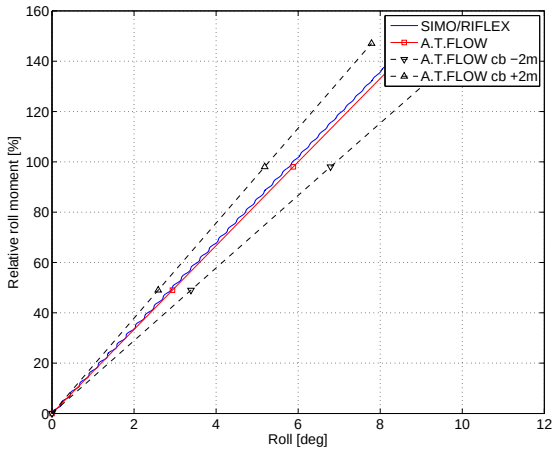

Figure 4.5: Pull-out in roll normalized wrt the value of A.T.FLOW at 6.0 deg. Therefore the value at 6.0 def offset is 100%.

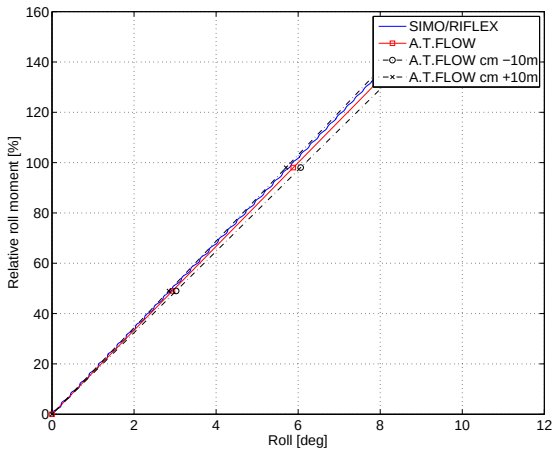

Figure 4.6: Pull-out in roll normalized wrt the value of A.T.FLOW at 6.0 deg. Therefore the value at 6.0 def offset is 100%.

4.4 The hydrodynamic damping of the substructure

The hydrodynamic damping indicates the resistance of the system in relation to translational velocity and angular velocity. The damping is caused by the seawater passing the spar and mooring lines. The hydrodynamic damping can be tested by a decay.

A decay test releases the system from a given position or rotation. The calculations are done in a situation of still water and no wind. The system will damp out. Statoil has executed decay tests using SIMO/RIFLEX. The results from SIMO/RIFLEX and A.T.FLOW are compared. The results of the decay tests in surge and roll are presented in Figures 4.7 and 4.8, respectively.

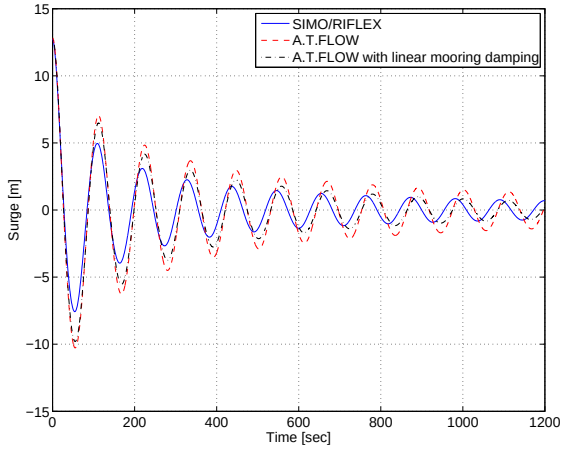

Figure 4.7: Decay test in surge

Figure 4.7 shows the hydrodynamic damping in surge of SIMO/RIFLEX and A.T.FLOW. The spar is released from approximately $X = 12.8$ m. The damping of SIMO/RIFLEX is larger than that of A.T.FLOW. Two important points to regard in the figure are the decay of the amplitude and the period of each oscillation. The period of SIMO/RIFLEX is approximately 105 sec. The period of A.T.FLOW varies from 112 to 109 sec. The period of A.T.FLOW is larger. This is also clearly visible in Figure 4.7. The period is mainly influenced by the mass of the system. This indicates that the mass in A.T.FLOW is too high. The decay of the amplitude is faster for SIMO/RIFLEX, which indicates larger damping. The difference could be explained by the fact that A.T.FLOW does not model

the damping of the mooring. Therefore some linear mooring damping was included in A.T.FLOW to analyse the impact. Figure 4.7 shows that the results with linear mooring damping are improved. Before extending A.T.FLOW with a dynamic mooring system, the measurements on Hywind should be awaited.

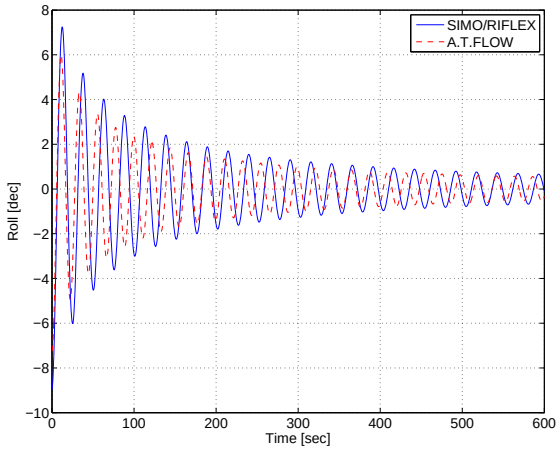

Figure 4.8: Decay test in roll

Figure 4.8 shows the decay of the roll angle. The platform is released from a roll angle of approximately 9 deg. The approximate periods of A.T.FLOW and SIMO/RIFLEX are respectively 20.2 and 21.5 sec. The period of A.T.FLOW is lower, which implies a lower moment of inertia. The decay of A.T.FLOW seems to go faster than SIMO/RIFLEX, which indicates larger damping.

It can be concluded that A.T.FLOW is stable for surge and roll decays. The results are not identical to the results from SIMO/RIFLEX, but the damping behaviour is simular. The measurements on Hywind are required to give recommendations on how to improve the hydrodynamic module. The results of the decay tests for the other degrees of freedom are given in Appendix E.

4.5 Aerodynamic performance of the wind turbine

The aerodynamic performance of SWT 2.3-82.4 used for Hywind is estimated by BHawC. The results from BHawC are compared with the BEM code results from A.T.FLOW. The verification of the aerodynamic performance is done in two steps. First, a single blade element is analysed comparing the aerodynamic

characteristics. Then, the overall performance of the full rotor is verified by comparing the total thrust and mechanical torque for different wind speeds.

BHawC contains a more detailed code considering aerodynamics than A.T.FLOW. To match the model results, BHawC is adapted to correspond to A.T.FLOW. Therefore BHawC is run without tilt and coning, and without 3D corrections. For this analysis both models are run with no yaw, no shear, no tower shadow, uniform wind and no waves. Still, some differences between the models are present. The calculations from BHawC can only be done with a dynamic turbine, while A.T.FLOW is able to consider a static turbine. The results of BHawC are therefore averages of a quasi-stable period. BHawC also consideres structural bending of the blades and tower, while A.T.FLOW assumes a rigid body.

Data from BHawC is available for wind velocities of 5, 10, 15, 20 and 25 m/s. The controller determines for every wind velocity a certain rotational speed Ω and blade pitch angle γ_2. These are presented in Table 4.1.

Table 4.1: Controller settings

V_p	5	10	15	20	25	m/s
Ω	0.808	1.67	1.75	1.747	1.747	rad/s
γ_2	-1	-1	8.6	17.15	23.7	deg

4.5.1 Blade element comparison

A blade element with radius r_b m has a certain resultant wind velocity W, angle of attack α, lift coefficient C_l and drag coefficient C_d. The aerodynamic characteristics of BHawC and A.T.FLOW are compared for a blade element with radius $r_b = 17.15$ m during a constant wind velocity $V_w = 5$ m/s. Table 4.2 shows the results from both models.

Table 4.2: Comparison of aerodynamic characteristics of a blade element with $V_w = 5$ m/s and $r_i = 17.15$ m

	BHawC	A.T.FLOW	Units
W	15.6	15.6	m/s
α	8.89	8.88	deg
C_l	1.15	1.15	-
C_d	0.0336	0.0336	-

Table 4.2 shows that the aerodynamic characteristics of this blade element match. If the structural characteristics of the blade are implemented correctly, then it can be concluded that the aerodynamic characteristics of all blade elements should match the results from BHawC. Then the total aerodynamic thrust and torque should match as well.

4.5.2 Overall aerodynamic performance comparison

Figure 4.9 shows the mechanical torque (Eq. 3.12) and axial thrust force (Eq. 3.10) for various constant wind speeds calculated with BHawC and A.T.FLOW. The results are compared for wind speeds of 5, 10, 15, 20 and 25 m/s. Data is available for for these wind speeds only.

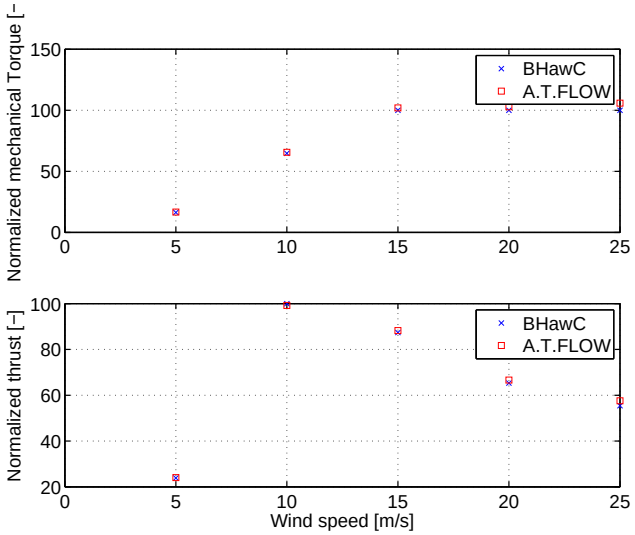

Figure 4.9: Results of BHawC and A.T.FLOW for the mechanical torque and thrust

The results of the thrust correspond with an error between 0.5% and 4% as presented in Figure 4.10. The torque results agree with an error between 1% and 6% as presented in Figure 4.11. These percentages are acceptable values. A more detailed research on the differences between BHawC and A.T.FLOW is required to analyse the model results. By adjusting the control settings, the results of A.T.FLOW can be tuned to match BHawC perfectly, but the settings of BHawC are sufficient. It can be concluded that the BEM code used in A.T.FLOW is correctly implemented.

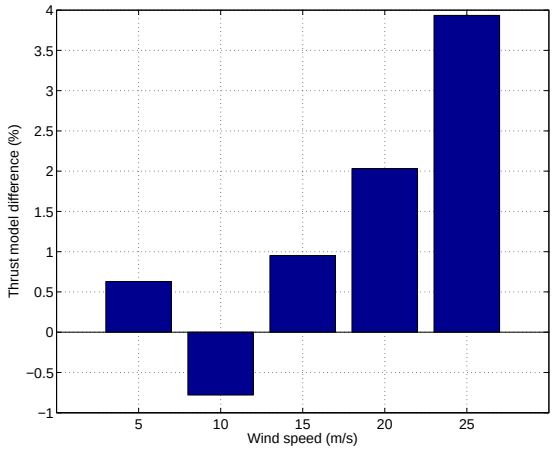

Figure 4.10: Model result differences of mechanical torque in percentages

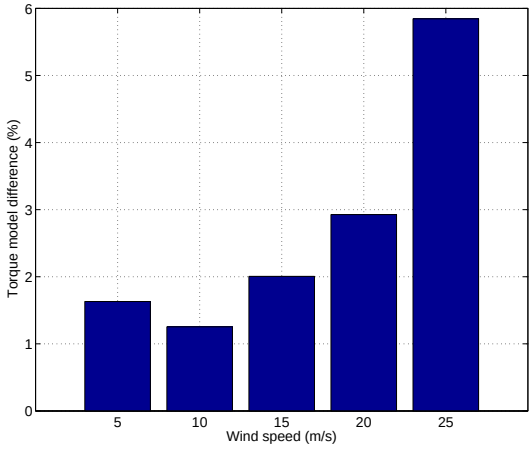

Figure 4.11: Model result differences of thrust in percentages

Chapter 5

Load case model predictions

5.1 Introduction

Based on simple calculations and logics, predictions are compared to model results from A.T.FLOW. The comparison shows if A.T.FLOW presents what is to be expected. The similarities and differences are analysed. Predictions are done on three types of load cases

- Case 1: Yaw misalignments between wind and wave
- Case 2: Yaw misalignments between wind and rotor in an idling situation
- Case 3: Wind gust

The cases are presented in Sections 5.2, 5.3 and 5.4. Each section contains a case explanation, a case prediction and a comparison with the model results.

5.2 Case 1: Wind-wave misalignment

Prediction case 1 analyses wind-wave yaw misalignments β_{w-w}. The wind has a constant velocity of 10 m/s and a fixed direction $\beta_{wind} = 0$ deg aligned with the rotor as illustrated in Figure 5.1. A single regular wave has a constant wave height of 3 m with direction β_{wave}. Since the system is symmetric along the X-axis, it is not nessecary to analyse misalignments over 360 degrees. Predictions are done on misalignment angles of 0, 30 and 90 deg. The initial orientation of the rotor is $\beta_{rotor} = 0$ deg for all misalignments. Figure 5.1 illustrates the different misalignment scenarios.

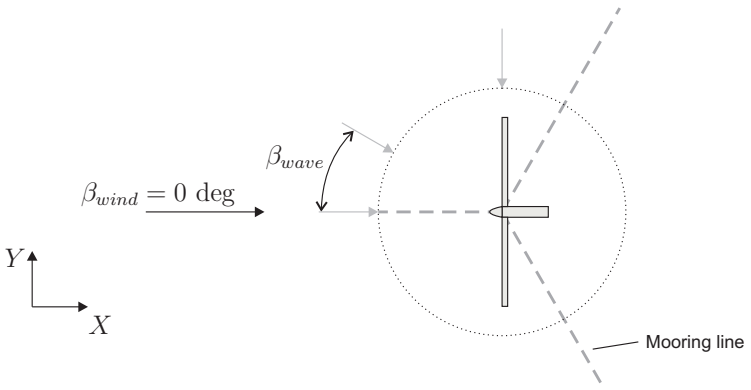

Figure 5.1: Load case with a wind-wave misalignment

5.2.1 Prediction

The following will occur during a wind-wave misalignment.

1. The thrust force enforces an average surge and pitch angle
2. A wave force in X direction causes surge oscillations. A wave force in Y direction causes sway oscillations
3. Rotor movement and rotation into the wind causes aerodynamic damping
4. When the turbine sways, it automatically surges due to the mooring system assymetry about the X axis
5. Pitch and yaw motion are coupled due to the gyroscopic effect of the rotor

Each occurence will be explained briefly

1. In time, a constant force causes permanent displacement and rotation. The constant thrust force results in an average displacement and rotation about which the turbine will oscillate. At this point, when static, the body forces are in equilibrium. Figure 4.9 shows that at a wind velocity of 10 m/s the thrust force is 220 kN. From Figure 4.4, it can be seen that the average surge displacement will be $X = 6.0$ m. A thrust force of 220 kN creates a moment around cg of 29700 kNm. Figure E.3 in Appendix D shows a corresponding pitch angle of $\phi = 2.0$ deg. The average displacement and angle of the other coordinates are zero.
2. The wave force is regular, but not constant, causing oscillations around the average coordinates. A wave force in X and Y direction causes oscillations in surge and sway, respectively. When yaw $\psi = 0$ deg, the X force causes a pitch oscillation and the Y force causes a roll oscillation. When yaw $\psi \neq 0$ deg, the force direction and angular oscillation are not directly related.

3. At a misalignment angle of 0 deg, assuming yaw $\psi = 0$ deg, surge and pitch motion are dominant. The rotor moves into or away from the wind increasing or decreasing the relative wind velocity. Aerodynamic damping will reduce the turbine's oscillations. At a misalignment ange of 90 deg, assuming yaw $\psi = 0$ deg, sway and roll motion are dominant. There is a negligible aerodynamic damping in sway and roll from the rotor. Therefore the oscillations will be larger compared to $\beta_{w-w} = 0$ deg.

4. The assymetry of the mooring system causes a negative surge force when the turbine has a sway displacement. When the sway displacement increases, the negative surge force increases, acting as a spring force. The turbine will make a loop in the horizontal plane. At a misalignment of 90 deg, when yaw $\psi = 0$ deg, the sway oscillations are highest causing the largest loop. The average surge displacement will decrease due to the increased negative F_X^{hydro}.

5. Due to the gyroscopic effect the pitch and yaw motions are coupled. At a misalignment of 0 deg, the pitch oscillation is largest causing a high gyroscopig yaw moment. When $\beta_{w-w} = 90$ deg, the yaw motion will be smaller due to the lower pitch oscillation.

The aerodynamic damping and assymetry of the mooring system predict the largest oscillations at $\beta_{w-w} = 90$ deg. The gyroscopig effect predicts the largest yaw motion at $\beta_{w-w} = 0$ deg.

Wind-wave misalignment angle of 0 degrees

For this scenario the wind and wave are aligned. Then

- Dominant surge and pitch oscillations
- Barely any sway and roll oscillations
- Large aerodynamic damping of surge and pitch
- Large yaw oscillations due to large pitch oscillation (Gyroscopig effect)

Wind-wave misalignment angle of 30 degrees

At a misalignment angle of 30 deg the wave force has a component in Y direction, while the force component in X direction has decreased. Then

- Decreased surge and pitch oscillations
- Increased sway and roll oscillations
- Lower aerodynamic damping

- Lower yaw oscillations due to lower pitch oscillation (Gyroscopig effect)
- Decreased average surge displacement due to mooring system assymetry

Wind-wave misalignment of 90 degrees

When increasing the misalignment angle to 90 deg, the behaviour described for a 30 deg misalignment will magnify. At $\beta_{w-w} = 90$ the wave force has no component in X direction. Then

- Dominant sway and roll oscillations
- Barely any surge and pitch oscillations
- Negligible aerodynamic damping
- Low yaw oscillations due to low pitch oscillation (Gyroscopig effect)
- Lowest average surge displacement due to mooring system assymetry. The only surge oscillation is caused by the assymetry of the mooring system.

Wind-wave misalignment angle higher than 90 degrees

Increasing the misalignment angle from 90 deg to 180 deg will vary F_Y^{hydro} and F_X^{hydro} as described before. The behaviour will not be different from previous misalignments.

5.2.2 Comparison to model

The predictions of case 1 are compared to the model results. Figure 5.1 shows the results of A.T.FLOW for $\beta_{w-w} = 0$ deg. The results of the other misalignments are given in Appendix F in Figures F.1, and F.2. It can be concluded that

- As predicted, surge and pitch oscillations are dominant for $\beta_{w-w} = 0$ deg, and sway and roll oscillations are dominant for $\beta_{w-w} = 90$ deg.
- As predicted, the yaw amplitude is largest at $\beta_{w-w} = 0$ deg due to the gyroscopic yaw moment. At $\beta_{w-w} = 30$ deg the yaw motion is already lower due to the decreased gyroscopic moment. The yaw motion is almost zero at at $\beta_{w-w} = 90$ deg.
- The average coordinates of surge and pitch are 5.65 m and 1.9 deg when $\beta_{w-w} = 0$ deg, and 5.50 m and 1.9 deg when $\beta_{w-w} = 90$ deg, which is near to the predicted 6.0 m and 2.2 deg. The lower average surge displacement at $\beta_{w-w} = 90$ deg is caused by the assymetry of the mooring system, as predicted.

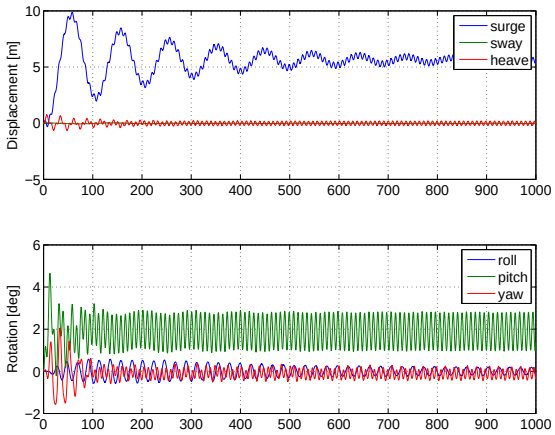

Figure 5.2: A.T.FLOW results for case 1 with a wind-wave misalignment of 0 deg

- The aerodynamic damping does not influence the oscillations induced by the waves. Figure 5.3 shows the velocities in X direction of a blade in time for $\beta_{w_W} = 0$ deg. The maximum velocity of the highest and lowest point on the rotor are 2.0 and -2.0 m/s, respectively. This causes a maximum $V_w = 12.0$ m/s and a minumum $V_w = 8.0$ m/s.

  The presence of aerodynamic damping can be noticed in Figures 5.3 and F.2, where the conversion of surge towards its average position is faster for $\beta_{w-w} = 0$ deg than for $\beta_{w-w} = 90$ deg. It was expected that the oscillations for $\beta_{w-w} = 0$ deg would be lower that for $\beta_{w-w} = 90$ deg due to the aerodynamic damping. However, the amplitudes of surge and sway are equal with 0.55 m for $\beta_{w-w} = 0$ deg and $\beta_{w-w} = 90$ deg. Also the amplitudes of pitch and roll are equal with 1.8 deg. This implies that the aerodynamic damping does not influence the oscillations induced by the waves. The reason for this is that the frequency of the wave is far from the natural frequencies. If the wave frequency would be closer to a natural frequency aerodynamic damping will have more impact [24].

5.3 Case 2: Wind-rotor misalignment

Prediction case 2 analyses the yaw misalignment β_{w-r} of the wind and the rotor, when idling at a high wind velocity of 44.8 m/s. This large wind velocity is used, because for this velocity the rotational speed is known for all yaw misalignments.

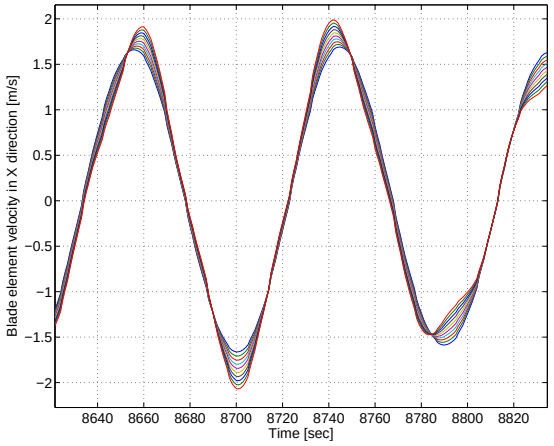

Figure 5.3: A.T.FLOW results for case 1 with a wind-rotor misalignment of 0 deg. The figure shows the surge velocity of different blade elements of one blade due to pitching the platform. Each line represent a different blade element. The blade element with the largest radius with an upward blade will have the largest surge velocity

During an idling situation the blade pitch angle is $\gamma_2 = -82$ deg. There is no wave. This would be very unrealistic at 44.8 m/s, but this is a test case for the aerodynamic model and not a realistic case. This wind-rotor yaw misalignment could occur when the yaw motor fails. The misalignments are caused by changing the wind direction and keeping the initial orientation of the rotor fixed. Figure 5.4 shows possible wind-rotor misalignments.

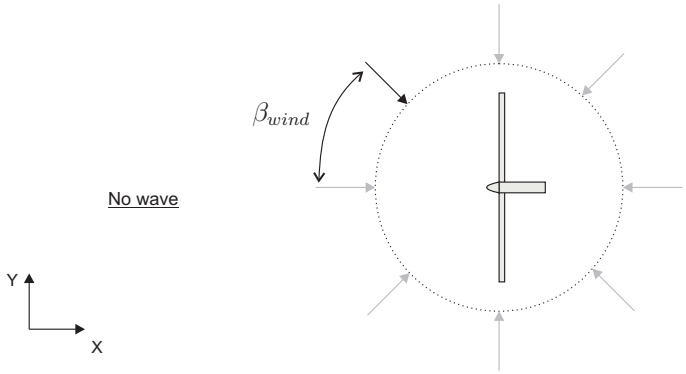

Figure 5.4: Load case with a wind-rotor misalignment

The angular velocity Ω of the rotor is approximately 12.6 deg/s, when the rotor and wind are aligned, hence $\beta_{w-r} = 0$. Ω varies for different misalignments. Figure 5.5 shows the average rotational velocity versus the misalignment angle. At certain misalignments the rotor will not rotate ($\Omega = 0$), but simply oscillate around an azimuth angle. During operation the rotor is never blocked. This data is provided by BHawC calculations.

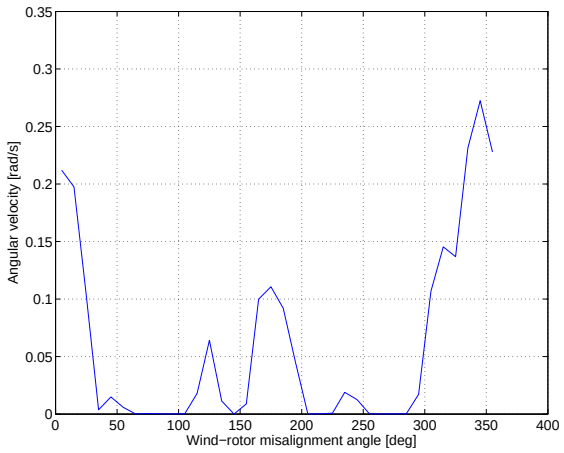

Figure 5.5: Angular velocity Ω versus misalignment angle (source: BHawC)

The prediction ignores momentum theory, tower shadow, shear and aerodynamic loads on the tower and nacelle. This is done to simplify the prediction. In idling the rotor barely extracts energy from the wind, resulting in low induction factors. Therefore the momentum theory can be neglected. The wind shear and tower shadow will not influence the general behaviour of the turbine for different misalignments, since they are not affected by the misalignment angle. Tower and nacelle drag loads are important. Their impact is analysed when needed. Predictions are done for misalignment angles of 0, 25, 90 and 345 deg.

5.3.1 Prediction

At any misalignment angle, either the upward blade or the downward blade will rotate into the wind, increasing the relative wind velocity. This causes loading differences on the upward and downward blades. The differences in blade loading is the key to this prediction. Theory and logical reasoning result in a prediction on the turbine behaviour. The prediction wil not result in exact values.

The wind velocity V_w has two components on a blade element: the perpendicular V_p and tangential V_t. When the rotational coordinates pitch, roll and yaw are zero

$$V_p = V_w \cos(\beta_{w-r}) \tag{5.1}$$

and

$$V_t = r_b\Omega - V_w \sin(\beta_{w-r}) \sin(\alpha_{az}) \tag{5.2}$$

with

V_w	Free stream wind velocity
V_p	Free stream wind velocity perpendicular to blade element
V_t	Free stream wind velocity tangential to blade element
β_{w-r}	Yaw misalignment between wind and rotor
r_b	Radius of blade element
Ω	Angular velocity
α_{az}	Blade azimuth angle

Equation 5.1 implies that V_p is always the same for all blade elements and depends on the misalignment angle β_{w-r}. Equation 5.2 states that V_t is the summation of the blade tangential velocity and the wind velocity component in tangential direction of the blade. V_t depends on the mislalignment angle and the azimuth angle. Every blade element has a different V_t. The variation of V_t is crucial in this prediction.

Wind-rotor misalignment angle of 0 degrees

The wind and rotor are aligned, hence $V_p = V_w$ and $V_t = r_b\Omega$. Consequently the angle of inflow ϕ, resultant wind velocity W and the angle of attack α are equal for all annuli. For this prediction case tower shadow and shear are neglected. Therefore the lift and drag forces are constant during a rotation. This adds up to a constant thrust and torque. The equations for the average aerodynamic forces in X, Y and Z direction are

$$F_X^{aero} = T = L\cos(\phi) + D\sin(\phi) \tag{5.3}$$

$$F_Y^{aero} = -(L\sin(\phi) - D\cos(\phi))\sin(\alpha_{az}) \tag{5.4}$$

$$F_Z^{aero} = (L\sin(\phi) - D\cos(\phi))\cos(\alpha_{az}) \tag{5.5}$$

During a full rotation, the summation of all aerodynamic forces in Y and Z direction cancel each other out, hence $F_Y^{aero} = F_Z^{aero} = 0$. F_X^{aero} will be constant, but the direction is still unknown.

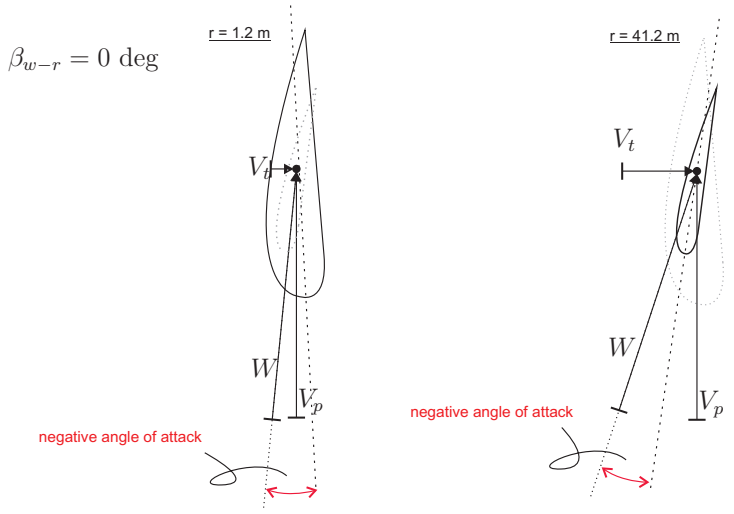

Figure 5.6: Tangential wind velocity on blade elements with $r_b = 20$ m and $\beta w - r = 0$ deg

Figure 5.6 shows that the angle of inflow varies from $\phi \simeq 90$ deg to $\phi \simeq 78$ deg depending on the blade radius. Using Equation 3.9 gives a varying angle of attack of $\alpha = -1$ deg to $\alpha = -5$ deg. The average value will lie around -3 deg. Around this angles of attack C_d and C_l are both very small, which is the purpose during idling. C_d is constant for all angles of attacks. C_l changes sign around $\alpha = -2.5$ deg and is maximum two times larger than C_d.
Using Equation 5.3 for the lowest radius $r = 1.2$ m with $\phi \simeq 90$ results in

$$F_X^{aero} = D > 0 \tag{5.6}$$

For the highest radius $r = 41.2$ m with $\phi \simeq 78$ deg

$$F_X^{aero} = T = 0.21L + 0.98D \tag{5.7}$$

The $C_l - \alpha$ and $C_d - \alpha$ state that for small angles of attack $L < 2D$, and the drag term is dominant. If the lift force would be negative, then F_X^{aero} is still positive. Due to the aerodynamic loads on the rotor the turbine will displace in positive surge and rotate in positive pitch. The displacement and rotation will be small due to the low forces.

Notice that the torque is negative, while it was expected that a positive torque $Q = I_{xx}^r \Omega$, where I_{xx}^r is the inertia of the rotor. It can be concluded that the data in Figure 5.5 does not correspond to the results of this prediction case. The prediction will not correspond to reality, but that is not of much importance in this verification method. The analysis is valid as long as the results of A.T.FLOW correspond to these predictions, e.g. giving a negative torque.

Wind-rotor misalignment angle of 25 degrees

When the wind changes direction it creates a 25 deg yaw misalignmen. The prediction gets more complicated. The rotor is still idling, but with a lower angular velocity of 5.8 deg/s (Figure 5.5). This implies a lower torque. Equation 5.1 gives that V_p will decrease with 90%. Equation 5.2 gives that V_t will vary between -18.8 m/s and 23.2 m/s depending on the blade element radius and azimuth. Figure 5.7 shows the tangential velocity V_t for the three blade elements with blade radius $r = 20$ m. The initial azimuth angles α_{az} of the blades are 0, 120 and 270 deg. The smallest tangential velocity -18.8 m/s occurs at the lowest blade radius $r_i = 1.2$ when the blade is vertically up with $\alpha_{az} = 90$. The highest tangential velocity 23.3 m/s occurs at the highest blade radius $r_i = 41.2$, when the blade is vertically down with $\alpha_{az} = 270$.

It can be concluded that when the blade is up, V_t is negative and small. When the blade is down, V_t is positive and large. V_t does not change sign exactly at $\alpha_{az} = 0$ deg or $\alpha_{az} = 180$ deg due to the influence of the low angular velocity of the rotor.

The aerodynamic lift L and drag D depend on the air density ρ_{air}, the surface of the blade element S, the resultant wind velocity W and the aerodynamic coefficients C_l and C_d. Only W, C_l and C_d are influenced by the varying V_t. The effect of V_t on W, C_l and C_d is analysed. Figure 5.8 shows a blade with $\alpha_{az} = 90$ and $\alpha_{az} = 270$ deg.

Figure 5.8 shows that W is low for an upward blade and high for a downward blade. The angle of inflow ϕ is higher than 90 deg when the blade is up, and lower when the blade is down. The angle of attack α is positive when a blade is up and negative when a blade is down. On average α of a downward blade is larger than α of an upward blade.

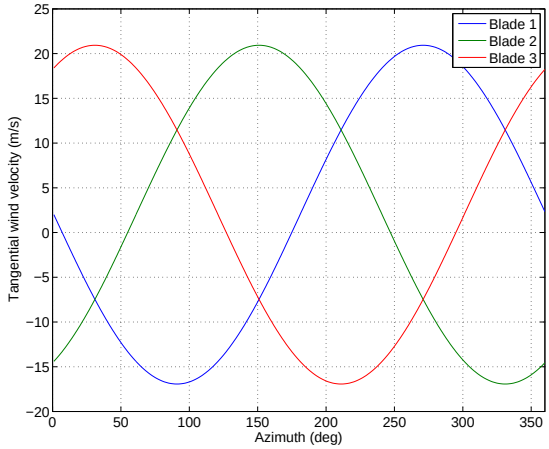

Figure 5.7: Tangential wind velocity and $\beta_{w-r} = 25$ on blade elements with $r = 20$ m

C_l and C_d depend on the angle of attack α. From the $C_l - \alpha$ and $C_d - \alpha$ curves it can be stated that C_l is positive when a blade is up. C_l is negative and larger when a blade is down. C_d is always positive, but larger for a downward blade. A summary is given in Table 5.1.

Table 5.1

	Blade up	Blade down	Units
V_p	-	-	m/s
V_t	< 0	$>> 0$	m/s
W	$< r\Omega$	$> r\Omega$	m/s
ϕ	> 90	$<< 90$	deg
α	> 0	$<< 0$	deg
C_l	> 0	$<< 0$	-
C_d	> 0	$>> 0$	-

The equations for the lift an drag force are repeated for convenience.

$$\Delta L = \frac{1}{2}\rho_{air} S W^2 C_l \tag{5.8}$$

$$\Delta D = \frac{1}{2}\rho_{air} S W^2 C_d \tag{5.9}$$

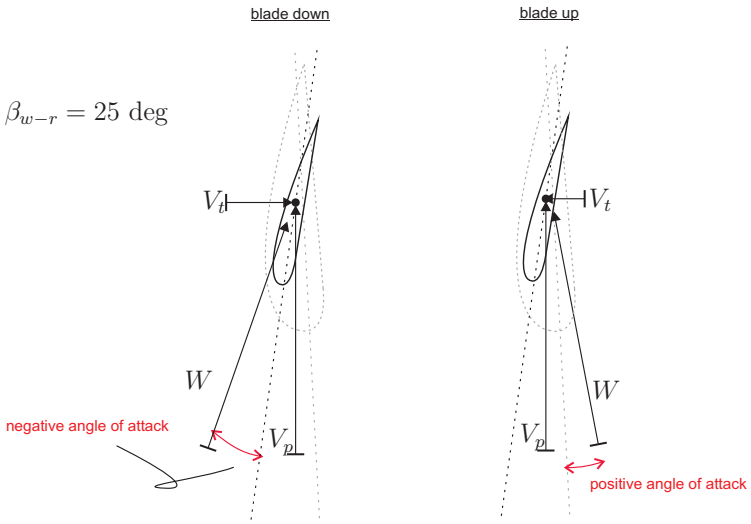

Figure 5.8: Aerodynamic characteristics for an upward and downward blade

Since W, C_l and C_d are all larger for a downward blade, the overall lift and drag force are larger on a downward blade. The lift force L is negative on a downward blade due to the negative lift coefficient. The drag force D is always positive. Summarizing:

- Blade up: Lift is small and positive
- Blade down: Lift is large and negative
- Drag is always positive

It can be concluded that at a misalignment angle of 25 deg the large lift force on the downward blade determines the average forces of a full rotation. The largest difference between upward and downward forces is when V_t is around $\alpha_{az} = 270$ deg. This happens every one third rotation, for $\beta_{w-r} = 25$ deg, $\alpha_{ax} = 270$ deg and $\Omega = 0.1$ rad/s, then $60 < \phi < 65$ deg for different radii. Taking the average $\phi = 62.5$ deg and using Eqs. 5.3 and 5.4 results in

$$F_X^{aero} = T = -0.46L + 0.88D \tag{5.10}$$

$$F_Y^{aero} = -0.88L - 0.46D = neg \tag{5.11}$$

It is clear that F_Y^{aero} is negative. Depending on the size of L and D, F_X^{aero} will be positive or negative. For these conditions the angle of attack varies from $-19.5 < \phi < -30$ deg. For these angles of attack holds $2D < L < 4D$. This concludes that F_X^{aero} is negative, since the negative lift force dominates the positive drag force. F_Y^{aero} is larger than F_X^{aero}. This implies a negative surge and a larger negative sway movement as a consequence of the aerodynamic forces on the rotor. The total aerodynamic blade force F_Z^{aero} is zero for all misaligments over a full rotation .

Conclusions on case 2

It can be concluded that the blade that is moving into the wind determines the average behaviour of the turbine. When $0 < \beta_{wind} < 180$ deg the downward blade is dominant and when $180 < \beta_{wind} < 360$ deg the upward blade is dominant. The predictions of the other misalignment angles can now be reasoned from previously gained knowledge.

- If $0 < \beta_{wind} < 180$ deg: downward blade is dominant, analyse α_{az}=270 deg
- If $180 < \beta_{wind} < 360$ deg: upward blade is dominant, analyse α_{az}=90 deg
- Find the average angle of inflow ϕ
- Find out if lift or drag is dominant
- Find out whether lift force is positive or negative
- Analyse Equations 5.3 and 5.4

Wind-rotor misalignment angle of 90 deg

Figure 5.5 shows that for $\beta_{w-r} = 90$ deg the blades will not rotate since $\Omega = 0$ rad/s. So neither the downward or upward blade will be dominant. When the blade is down, the angle of inflow is $\phi \simeq 0$ deg and the angle of attack is $\alpha \simeq -90$ deg. When the blade is up holds $\phi \simeq 180$ deg and $\alpha \simeq 90$ deg. For both scenarios holds $D >> L$. The drag coefficient C_d is maximum and $C_l \simeq 0$. Using Equation 5.3

$$F_X^{aero} \simeq 0 \tag{5.12}$$

There will be no displacement in surge. Using Equation 5.4 for the downward blade with $\phi = 0$ deg and $\alpha_{az} = 270$ deg

$$F_Y^{aero} = -D\cos(0)\sin(270) > 0 \tag{5.13}$$

For the upward blade with $\phi = 180$ deg and $\alpha_{az} = 90$ deg

$$F_Y^{aero} = -D\cos(180)\sin(90) > 0 \tag{5.14}$$

So F_Y^{aero} is always positive causing negative sway. The tower and nacelle aerodynamic drag will both increase the negative sway displacement. The torque will vary from positive to negative, oscillating around one azimuth angle, which corresponds to the expected $\Omega = 0$ rad/s.

Wind-rotor misalignment angle of 345 deg

The upward blade is most dominant when $\alpha_{az} = 90$ deg. The average angle of inflow $\phi \simeq 70$ deg and the angle of attack $-12 < \alpha < -22$ deg, which ensures a dominant lift between $4D < L < 6D$. Lift is negative. Using Equations 5.3 and 5.4

$$F_X^{aero} = -0.34L + 0.94D \tag{5.15}$$

$$F_Y^{aero} = .94L + 0.34D > 0 \tag{5.16}$$

The aerodynamic loads on the blades cause a negative surge and a negative sway displacement. The displacement in sway is larger, because $F_Y^{aero} > F_X^{aero}$. The large negative lift will create a large negative torque.

5.3.2 Comparison to model

The predictions are compared to the results of A.T.FLOW for misalignments $\beta_{wind} = 0$ deg, $\beta_{wind} = 25$ deg, $\beta_{wind} = 90$ deg and $\beta_{wind} = 350$ deg. The BEM code in A.T.FLOW is used when the wind loads create a significant torque. When idling, momentum theory is neglected and the aerodynamic loads are only calculated with blade element theory. The predictions are summarised in Table 5.2.

	mean F_X^{aero}	mean F_Y^{aero}
$\beta_{wind} = 0$	> 0	$\simeq 0$
$\beta_{wind} = 25$	< 0	< 0
$\beta_{wind} = 90$	$\simeq 0$	< 0
$\beta_{wind} = 345$	< 0	> 0

Table 5.2: Misalignments wind rotor

The results of A.T.FLOW for $\beta_{w-r} = 0$ are shown in Figures 5.9 and 5.10. The results of the other misalignments are given in Appendix G.

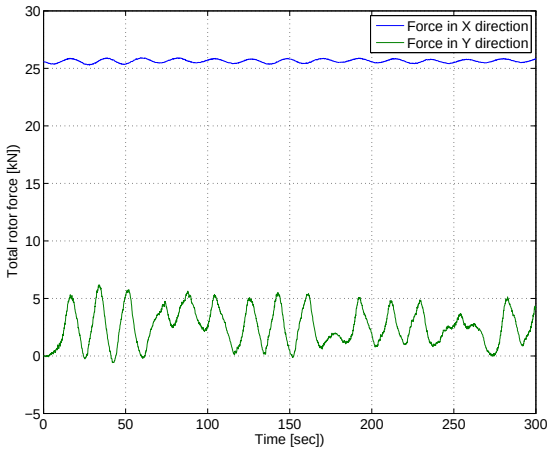

Figure 5.9: Total aerodynamic forces on rotor at $\beta_{w-r} = 0$ deg

Comparison: Wind-rotor misalignment angle of 0 deg

The prediction is that F_X^{aero} is positive and constant. F_Y^{aero} should be zero. Figure 5.9 shows a positive, but fluctuating F_X^{aero} and F_Y^{aero}. Neither is exactly zero. These differences can be explained by the yaw rotation of the turbine as shown in Figure 5.10. This creates a small misalignment causing an extra average force in Y direction. When the angular coordinates are zero, F_X^{aero} is constant and F_Y^{aero} is zero.

Comparison: Wind-rotor misalignment angle of 25 deg

It was predicted that the averages of F_X^{aero} and F_Y^{aero} are negative. The results of A.T.FLOW are presented in Appendix G in Figure G.1. The prediction and results agree. Due to the misalignment angle the forces fluctuate for every rotation.

The aerodynamic force on the tower is neglected in this analysis. The affect of the tower drag is briefly investigated. The lift coefficient of the circular tower is zero. The drag coeffiecient is 0.6. At wind velocity of 44.8 m/s, the aerodynamic force on the tower equals

$$F_{tower}^{aero} = \frac{1}{2}\rho_{air} C_d H_{hub} \overline{D}_{tower} V_w^2 \tag{5.17}$$

with

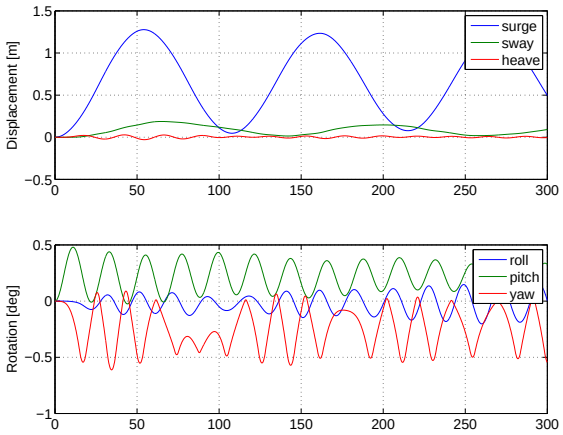

Figure 5.10: Displacements and rotations on rotor at $\beta_{w-r} = 0$ deg

$\overline{D}_{tower}$ Average tower diameter

This results in a total tower drag force of 144 kN, with 130 kN in X direction and -61 kN in Y direction. The tower drag force in X direction is much larger than F_X^{aero}. Therefore the surge force will be positive instead of negative. The tower drag force in Y direction increases the negative sway displacement. Both pitch and roll will be positive.

Comparison: Wind-rotor misalignment angle of 90 deg

The prediction is that F_X^{aero} is zero and F_Y^{aero} is negative. The rotor does not rotate which implies an average torque of zero. The results of A.T.FLOW are presented in Appendix G in Figure G.2. The prediction and results agree. F_X^{aero} is not exactly zero, but very small. This stems from the fact that the average angle of attack is not precisely 90 or -90 deg. F_Y^{aero} converges to a constant value, since the blades are positioned on a fixed azimuth. The torque force should also converge to zero, but it converges to a small negative torque, as shown in Figure G.3. At the current fixed azimuth angles of 0, 120 and 270 deg, the drag of the last downward blade with $\alpha_{az} = 270$ deg is highest causing a small negative torque. Therefore the model results indicate a small negative torque. In reality, this low torque will cause a negative rotation. At some new azimuth position the drag of the upper blades will be higher causing a positive torque. In this way, the rotor will oscillate around an azimuth position and will never make a full rotation.

Comparison: Wind-rotor misalignment angle of 345 deg

The prediction is that F_X^{aero} is positive and F_Y^{aero} is negative. The results of A.T.FLOW are presented in Appendix G in Figure G.4. Again, the prediction and results agree. Another prediction is a large negative torque. The results of A.T.FLOW shown in Figure G.5 confirm this.

The negative rotor force in X direction is overruled by the larger positive drag force on the tower as was estimated earlier for the 25 deg misalignment. The total tower drag force is 144 kN, with 139 kN in X direction and 17 kN in Y direction.

5.3.3 Conclusions

The predictions merely agree with the model results of A.T.FLOW. If not, the differences can be explained. An important remark is that the aerodynamic torque is often negative when the mean angular velocity was assumed positive. The angular velocities are results from BHawC under the same conditions. The mean angular velocity for each misalignment angle must however be incorrect. Therefore the results of this case do not relate to reality, but it can be concluded that the model does what is to be expected under these conditions. Therefore it is still a valid verification method.

5.4 Case 3: Wind gust

Case 3 analyses a wind gust, a sudden change in the wind velocity. The wind direction is fixed with $\beta_{wind} = 0$ deg and there are no waves.

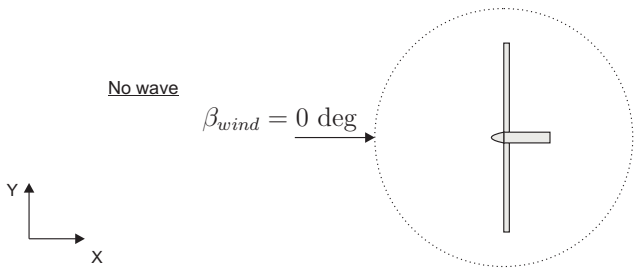

Figure 5.11: Load case with a wind gust

The equation for a gust given by IEC standard is [25]

$$V_{gust} = V_w - 0.37\Delta V sin(\frac{3\pi t}{T})(1 - cos(\frac{2\pi t}{T})) \tag{5.18}$$

with

V_{gust}	Free stream wind velocity during gust
V_w	Free stream wind velocity
ΔV	Amplitude of gust
t	Time
T	Period of gust

The period is set by IEC as $T = 10.5$ sec and the amplitude $\Delta V = 3.3$ m/sec [25]. Figure 5.12 shows a gust occuring during a constant wind velocity $V_w = 10$ m/s.

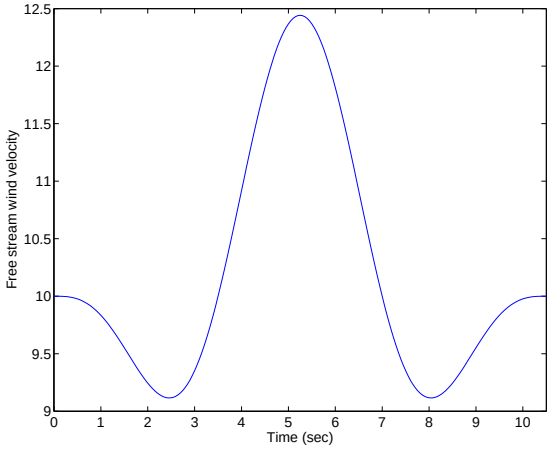

Figure 5.12: Wind gust

The wind gust effects the perpendicular wind velocity V_p. At first V_p will decrease a little to 9.1 m/s, followed by a large increase to 12.5 m/s. Then it rapidly decreases again to 9.1 m/s after which it regains its initial stable wind velocity of 10 m/s. Due to the shape of the curve it is often referred to as "the Mexican hat".

5.4.1 Prediction

Consider a wind gust occuring during production with a constant wind velocity of 10 m/sec. The gust will occur when the motion of the turbine is regular. Regular means that the turbine oscillates regularly around an average position with surge X, sway Y, heave Z, roll θ, pitch ϕ and yaw ψ. The turbine is never fully static. A wind velocity of 10 m/s causes a thrust force on the rotor of 220 kN, as can be seen in Figure 4.9. From Figure 4.4 it can be read that the average surge displacement will be $X = 6.0$ m. A thrust force of 220 kN creates a moment around cg of 29700 kNm. Figure D.3 in Appendix D shows a corresponding pitch angle of $\phi = 2.0$ deg. The other coordinates have an average of zero.

When V_p decreases, the controller normally increases the pitch angle of the blade to get the required torque. Following the Mexican hat, now V_p increases dramatically, but the controller is not able to decrease the pitch of the blades with the required speed. This creates unwanted large aerodynamic loads. The controller in A.T.FLOW does not adjust the pitch angle during a change in wind velocity. A constant pitch angle and rpm is set for the constant wind velocity of 10 m/s. The aerodynamic loads will therefore differ from reality. Locally this load difference is important, but overally has minor impact. This is especially true for a structure with such a high mass and inertia. A.T.FLOW is therefore not appropriate for aerodynamic analyses during e.g. a wind gust, but more suited for general physical turbine behaviour.

Even so, a prediction on the model results will be given. The change of V_p affects the resultant wind velocity W, the angle of inflow ϕ and the angle of attack α. Following Eqs. 3.7, 3.8 and 3.9, when V_p decreases, the other parameters decrease, and when V_p increases, the other parameters increase. For none of the blade elements will the angle of attack turn negative or reach the stall area. It can be concluded that the lift and drag force are high at the peak of the gust and low at the minima of the gust. This results in a thrust force and moment that will follow the Mexican hat curve.

If the floating turbine is quasi-static, the affects of a wind gust will be visible. At the peak of the Mexican hat the thrust will enforce an extra acceleration in surge and pitch. The hydrodynamic loads, which were zero before the gust appeared, will react to the sudden motion of the spar. The horizontal mooring forces and aerodynamic loads are in equilibrium at the attained displacement of the fairlead. When the gust passes, the displacement of the fairlead will trigger the mooring lines and increase the reaction force of the mooring system. The extra pitch rotation will induce a yaw rotation due to the gyroscopic moment. When the gust has passed, the turbine will slowly return to its initial position due the damping of the hydrodynamic loads and the stiffness of the mooring lines.

Only minor global dynamic movement of the turbine occurs due to the gust. The high mass and inertias will result in a minor affect of the gust on the turbine behaviour. Therefore, the prediction is that the gust will influence the surge and pitch behaviour little.

The gust might have no influence on the overall behaviour, but locally it will. The local stress at hub and tower will increase, challenging the design driving loads.

5.4.2 Comparison to model

During a uniform wind velocity of 10 m/s a simulation of a wind gust is done in A.T.FLOW At $T = 1704$ sec the wind gust starts. At this time the turbine is quasi-static. The wind gust as modeled by A.T.FLOW is presented in Figure 5.13.

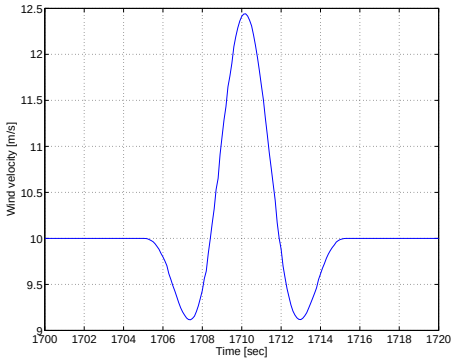

Figure 5.13: Wind gust A.T.FLOW modeling results

The average coordinates of the turbine are $X = 5.51$ m, $Y = 0$ m, $Z = -0.05$ m, $\phi = 1.9$ deg and $\phi = \psi = 0$ deg. The prediction was $X = 6.0$ m and $\phi = 2.0$ deg. The aerodynamics forces during the gust are presented in Figure 5.14.

As predicted, the aerodynamic thrust force in X direction follows the shape of the Mexican hat. Due to the small yaw angle at the moment that the gust occurs, the thrust force has a component in Y direction. Therefore, the Maxican hat is also visible in F_Y^{aero}. The surge and pitch coordinates are presented in Figures 5.15 and 5.16.

At $T = 1704$ sec, the surge suddenly decreases and increases, but minor. The sudden drop and climb has an amplitude of only a couple of centimeters, which

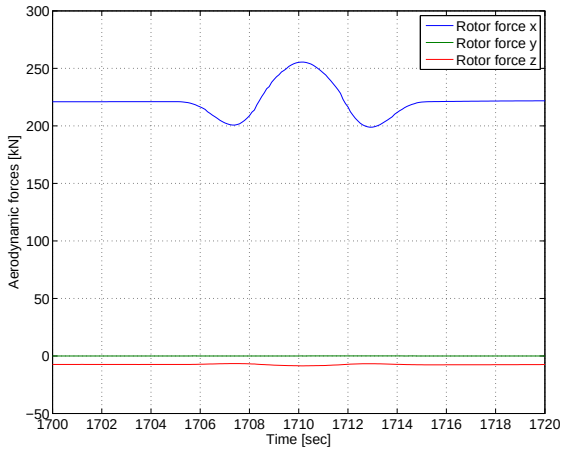

Figure 5.14: Total aerodynamic forces on rotor

indicates the small impact. This was also predicted. The pitch reacts stronger to the gust as presented in Figure 5.16. The quasi-static pitch angle suddenly drops to 1.86 deg and increases to 1.98 deg. In 200 sec the pitch angle converges back to 1.9 deg.

The prediction is that the mooring and hydrodyanic forces would react to the gust. However, the mooring force does not react, since the surge variation is only a few centimeter. The hydrodynamic force does react since it depends on velocity and acceleration, and not on displacement. The sudden increase in angular velocity from zero creates hydrodynamic damping, as presented in 5.17.

Another prediction was an increased yaw angle caused by the increased gyroscpic moment around the z axis due to the sudden pitch rotation. This prediction is confirmed by the A.T.FLOW results of the gyroscopic moment around the z axis as presented in Figure 5.18.

5.4.3 Conclusions

The wind gust has no impact on the surge behaviour. However, the pitch angle is more sensitive to wind fluctuations. Therefore the mooring system does not respond to the gust, while the hydrodynamic damping and gyroscopic moment around the z axis do. The gyroscopig effect is the most dominant reaction to a wind gust for a heavy spar-type floating wind turbine.

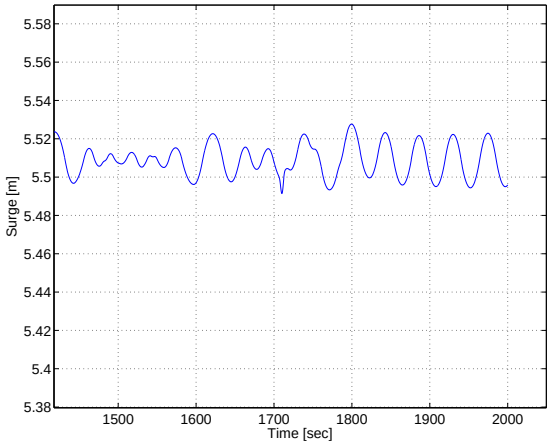

Figure 5.15: Surge displacement

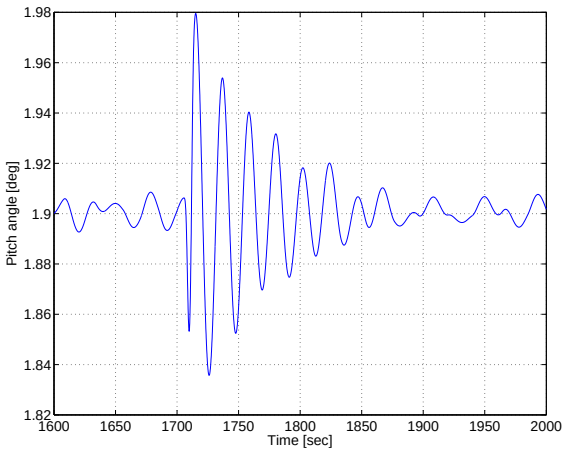

Figure 5.16: Pitch angle

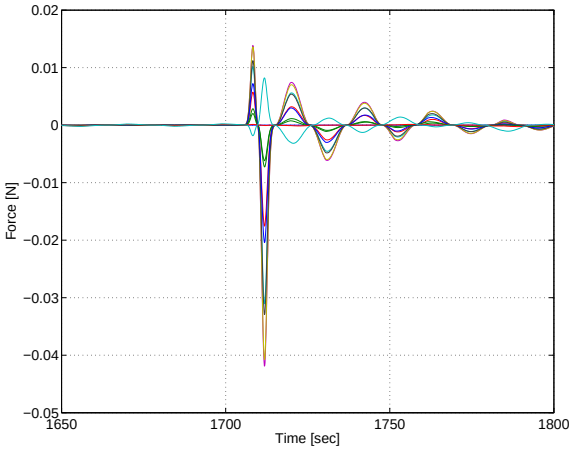

Figure 5.17: Total hydrodynamic forces in X direction

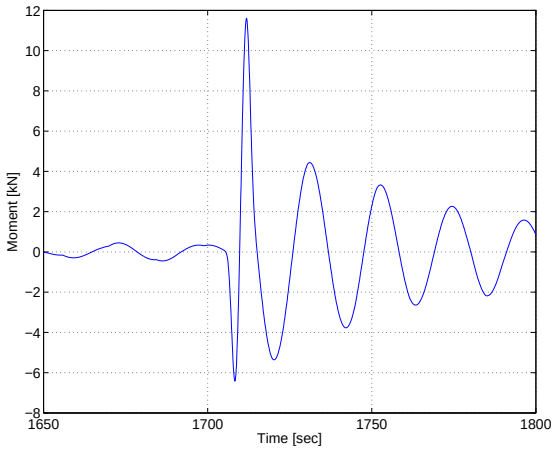

Figure 5.18: Gyroscopig moment around the z axis

Part III

Conclusions and recommendations

Chapter 6

Conclusions

The new A.T.FLOW model has been shown to be a useful tool for assessing the physical behaviour of spar-type floating wind turbines. The limitations of the model do not significantly reduce the quality of the simulation results. The verification methods in Chapters 4 and 5 give good results. They show that the model simulates different load cases as expected. This model can be used to implement and test modules for complex models, such as the hydrodynamic module for BHawC.

The simplifications made in the model, help the interpretation of model results in the light of the standard theory. As a result, the model facilitates to assess the physical behaviour of the spar. The model is practical to use due to its clear documentation and model structure. The model is easy to adapt and extend.

Tower top oscillations into the wind of fixed turbines are aerodynamically damped. For this reason the worst case wind-wave misalignment is 90 deg, when there is no aerodynamic damping. For a floating turbine this is not the case. Prediction case 1 (wind-wave misalignments) shows that aerodynamic damping has no influence on wave-induced oscillations. This is because the natural frequencies of the floating system are very low and far below the wave frequency. Therefore the wind-wave misalignment of 90 deg is not the worst scenario. Contrarily, the aligned case is the worst scenario due to the large gyroscopic moments.

The model clearly demonstrates that the dominant loads on the structure are wave-related, while wind loads have minor impact. First of all, the wave loads are much larger than wind loads. A three meter wave results in a force six times larger than the maximum wind thrust force. Secondly, wind loads result in average displacements, while wave loads enforce continuous dynamics on the system. When the system has reached the average displacement, the aerodynamic loads only act as damping forces. In addition, the aerodynamic damping has no influence on wave-induced oscillations, as concluded above.

The dominance of the hydrodynamic loads indicates that any meaningful modeling approach for spar-type wind turbines, hydrodynamic theory should be the starting point to correctly analyse physical behaviour.

Prediction case 2 and 3 (idling wind-rotor misalignments and wind gust) contribute to the verification process of A.T.FLOW, but could not give insight in the real physical behaviour. To do so, a more advanced dynamic controller is required. The BEM code presently used in A.T.FLOW is standard and not suitable for advanced aerodynamic research.

A.T.FLOW is limited to basic aerodynamic research. It was concluded that more detailed aerodynamic research requires an extended BEM code. The limitations of BEM theory (yaw and 2D errors) is a matter which in general concerns all researchers working with rotor aerodynamics. It is not an issue which this model should focus on. As long as axial wind conditions are analysed the used BEM code is accurate enough.

Chapter 7

Recommendations

The aim was to assess physical behaviour of spar-type floating wind turbines. In terms of physical behaviour some matters are not yet assessed, such as structural bending and mooring dynamics. The body is assumed rigid and the mooring system assumed quasi-static.

When extending the model, with e.g. a dynamic controller, it is recommended to compare results of A.T.FLOW with and witout the extension. If differences are minor, one should analyse whether the extension is necessary, considering that an extention makes the model more complex.

The inaccuracies of non-flexibility and static mooring can be improved without jeopardising the model's simplicity. I recommend to extend A.T.FLOW by taking into account structural bending and mooring dynamics. Focus should lie on the bending of the support structure and not of the blades. The circular geometry of the support structure enables a basic bending model. Modeling the dynamics of the mooring system requires a multi-body approach, in which the platform and the mooring system are two bodies. The mooring body would require a differential equation solver for its own equations of motion.

The implementation of a dynamic controller will contribute to assessing yawed idling cases. A.T.FLOW allows an implementation of a dynamic controller, but a dynamic controller will complicate the model and the model results. A recommendation is to enable the controller to switch from static to dynamic depending on the load case analysed. Implementing a dynamic controller requires a multi-body approach regarding the rotor as a second body. An equation of motion is solved for the angular acceleration containing the rotor axial inertia, the generator torque, the acting aerodynamic loads and the mechanical friction. The rotor angular velocity and blade pitch angle are no longer set, but regulated in time.

It is recommended to test the implementation of tilt and coning of the blades.

Results with large rotations (approximately higher than 10 deg) are inaccurate. However, a single large angle (ω_x, ω_y or ω_z) is still accurate, but the combination of two large angles is not. For these cases the differential equations must be improved. The Euler angles should be implemented as generalized coordinates $\vec{\omega}(\theta, \phi, \psi, \dot{\theta}, \dot{\phi}, \dot{\psi})$ in the differential equations, which is then solved for $\dot{\theta}$, $\dot{\phi}$ and $\dot{\psi}$.

The coming two years the loads on and behaviour of the operating Hywind is monitored. This data should be used to further test and validate A.T.FLOW and to guide further development of the model. The measurements on Hywind are a great opportunity for increasing our knowledge on floating turbines and to test and refine our models. This would be of great value to scientific research.

Part IV

Appendices

Appendix A

Hywind Demo technical drawing

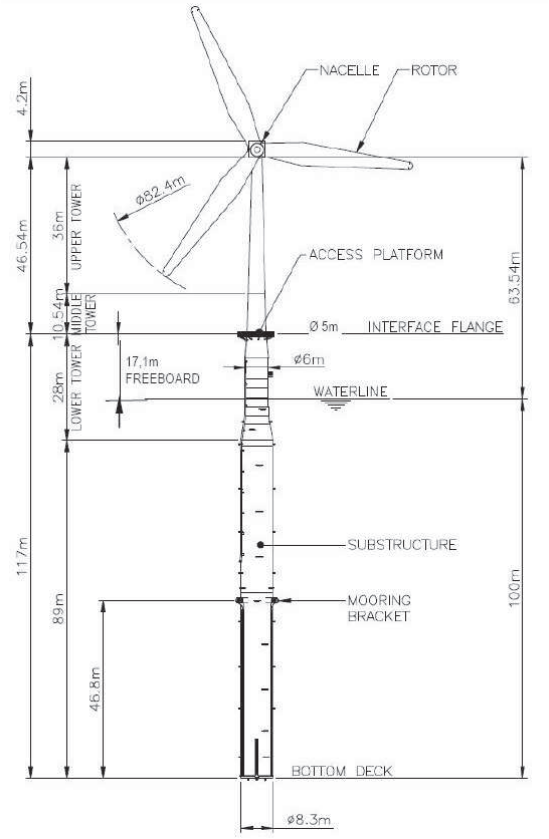

Figure A.1: Hywind dimensions

Appendix B

Hywind physical description

A technical drawing of the Hywind demo project is given in Appendix A. Hywind consists of a wind turbine, a transition piece, a substructure, a mooring system and an electric cable. The wind turbine consists of blades, nacelle, hub, upper tower and middle tower. The transition piece is the middle tower and the lower tower. The total mass of Hywind is 5086 metric tonnes, excluding the mass of the mooring system.

A slender deep spar buoy with ballast in the bottom ensures a large righting moment preventing the turbine from tipping over. The circular floating element has a draft of 100 m below the sea surface and a maximum diameter of 8.3 m. The spar structure consists of a steel jacket filled with high density olivin. Water ballast can in addition be added to control the draft of the floater.

Three catenaty mooring lines prevent the platform from drifting off. The lines are separated by 120 deg and moored to the seabed using anchor points. A clump weight hangs on each line to increase the line tension. The lines are attached to the substructure 46.8 m above the spar bottom. The lines are connected to the substructure using a delta connection to also create a yaw stiffness. The offshore location of the pilot wind turbine has a water depth of 210 meters. The sea bottom has a slight slope such that the anchors may have a difference in depth of about 10 m.

The load carrying structure of the turbine consists of three parts; the substructure, the transition piece and the tower. All are made from steel. The substructure is the lowest part with a length of 89 m and has constant diameter of 8.3 m. The transition piece (TP) has a length of 28 m and has a varying diameter. In between depths $4.5 < d < 11$ m the diameter of TP changes linearly from 8.3 m to 6.0 m. The diameter stays constant up to a height from MWL $H = 11$ m. In between $11 < H < 17$ m the diameter varies linearly to a diameter of 5.0 m. The tower deck is positioned at $H = 17$ m. The tower length is 46.5 m. The

diameter of the tower decreases linearly to the top from 5.0 m to 2.4 m.

The wind turbine has a rated capacity of 2.3 MW. The rotor has a diameter of 82.4 m and the rotor hub towers 65 m above mean water level (MWL). The shortest distance from MWL to the rotor tip is 24.5 m. The total weight of the turbine is 138 tonnes. Adjustments have been made to suite the floating conditions, but the blades are standard.

Appendix C

Kinematics and Transformations

In section 2.1 it is assumed that the structural components are infinitely stiff, which means that structural bending of all parts is neglected. The structure is considered as a rigid body, which is treated as a point mass positioned at the center of mass of the body. When the kinematics of one point known, the kinematics can be calculated for each point on the body. This requires basic kinematical calculations as explained in section C.

A vector can be expressed in the global or local coordinate systems. Transformations between the global and local coordinates are required. Transformation matrices transform a vector from one coordinate system to another. The transformation matrices are given in section C. The angular velocity as function of the Euler angles is given in section C.

Kinematics

The absolute position of a point is a vector function of time keeping track of where the point is at each instant [26].

$$\vec{r}_p = \vec{r}_{cg} + \vec{r}_{rel}; \tag{C.1}$$

with

$\vec{r}_p$	The absolute position of point p in the global coordinate system
$\vec{r}_{cg}$	The position of the center of mass cg in the global coordinate system
$\vec{r}_{rel}$	The relative position of point p in the global coordinate system

The position vector $\vec{r}_{cg}$ of the center of mass is expressed as

$$\vec{r}_{cg} = X\hat{i} + Y\hat{j} + Z\hat{k} = \begin{bmatrix} X \\ Y \\ Z \end{bmatrix} \tag{C.2}$$

The relative position $\vec{r}_{rel}$ of point p with respect to cg is expressed as

$$\vec{r}_{rel} = X_{rel}\hat{i} + Y_{rel}\hat{j} + Z_{rel}\hat{k} = \begin{bmatrix} X_{rel} \\ Y_{rel} \\ Z_{rel} \end{bmatrix} \tag{C.3}$$

The coordinates of vector $\vec{r}_{rel}$ are unknown. They can be calculated by transforming the fixed local coordinates x, y and z to the global coordinates X_{rel}, Y_{rel} and Z_{rel}. This is done with a transformation matrix, which is presented in section C, in Eq. C.9. The absolute velocity $\vec{v}_p$ of a point on a rigid body is [26]

$$\vec{v}_p = \vec{v}_{cg} + \vec{\omega} \times \vec{r}_{rel}; \tag{C.4}$$

with ω the angular velocity vector of the local reference frame

$$\vec{\omega} = \begin{bmatrix} \omega_x \\ \omega_y \\ \omega_z \end{bmatrix} \tag{C.5}$$

Transformation matrices

Transformations between coordinate systems are done with transformation matrices. They are are used to transform a vector in the global coordinate system to the a local coordinate system, and vice versa. Examples of vectors are positions, velocities, accelerations, forces and moments.

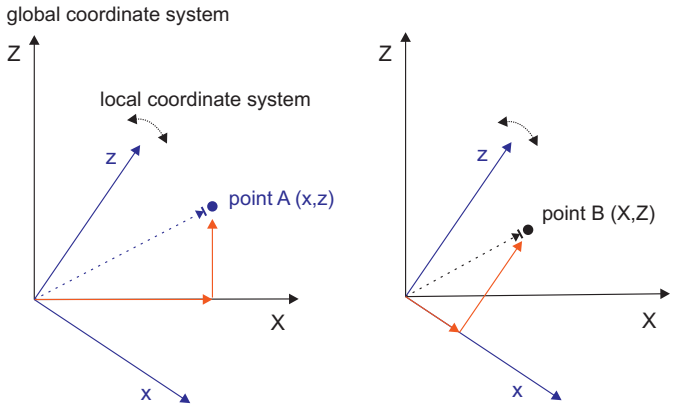

Figure C.1: Transformations between the global and local coordinate systems

Figure C.1 shows point A as a function of local coordinates (left) and point B as a function of global coordinates. The local vector of point A is split up into components on the global axes. This transformation is called transformation 1 and uses the transformation matrix R. The global vector of point B is split up into components on the local axes. This transformation is called transformation 2 and uses the transformation matrix T. As an example Figure C.1 illustrates a 2D case, but the transformation matrices convert vectors in 3D.

Transformation 1 converst a vector with local coordinates into a vector with global coordinates using transformation matrix $R = R_\theta R_\phi R_\psi$ (see left illustration of Figure C.1). Transformation 2 transforms a vector with global coordinates into a vector with local coordinates using transformation matrix T (see right illustration of Figure C.1). The transformation matrix $T = R_\psi R_\phi R_\theta$. The rotation matrices are

$$R_\psi = \begin{bmatrix} \cos(\psi) & \sin(\psi) & 0 \\ -\sin(\psi & \cos(\psi) & 0 \\ 0 & 0 & 1 \end{bmatrix} \tag{C.6}$$

$$R_\phi = \begin{bmatrix} \cos(\phi) & 0 & -\sin(\phi) \\ 0 & 1 & 0 \\ \sin(\phi) & 0 & \cos(\phi) \end{bmatrix} \tag{C.7}$$

$$R_\theta = \begin{bmatrix} 1 & 0 & 0 \\ 0 & \cos(\theta) & \sin(\theta) \\ 0 & -\sin(\theta) & \cos(\theta) \end{bmatrix} \tag{C.8}$$

Equation C.6 transforms the first yaw rotation ψ, Equation C.7 transforms the following pitch rotation ϕ and Equation C.6 transforms the final roll rotation θ.

Transformation local to global

With the transformation matrix known, the relative position of point p as given in Eq. C.3 can be calculated by transforming the fixed local coordinates x, y and z to the global coordinates X_{rel}, Y_{rel} and Z_{rel}.

$$\vec{r}_{rel} = \begin{bmatrix} X_{rel} \\ Y_{rel} \\ Z_{rel} \end{bmatrix} = R_\theta R_\phi R_\psi \begin{bmatrix} x \\ y \\ z \end{bmatrix} \tag{C.9}$$

Equation C.9 shows the transformation of a position vector, but can be used for any vector transformation, e.g. a vector force. Equation C.10 transforms a local force vector to a global force vector.

$$\vec{F}_{XYZ} = R_\theta R_\phi R_\psi \begin{bmatrix} F_x \\ F_y \\ F_z \end{bmatrix} \tag{C.10}$$

with

$\vec{F}_{XYZ}$	The force vector with global coordinates X, Y and Z
F_x	Force in the local x direction
F_y	Force in the local y direction
F_z	Force in the local z direction

Transformation global to local

The other way around, the components on the local axes of a global vector can be calculated with

$$\begin{bmatrix} x \\ y \\ z \end{bmatrix} = R_\psi R_\phi R_\theta \begin{bmatrix} X \\ Y \\ Z \end{bmatrix} \tag{C.11}$$

These vectors can be any vector, e.g. a position, velocity or force.

Angular velocity

From the rotation matrices R_θ, R_ϕ and R_ψ the angular velocity $\vec{\omega}$ around the xyz-axes can be found [26].

$$\vec{\omega} = \begin{bmatrix} \omega_x \\ \omega_y \\ \omega_z \end{bmatrix} = \begin{bmatrix} 1 & 0 & -\sin(\phi) \\ 0 & \cos(\theta) & \sin(\theta)\cos(\phi) \\ 0 & -\sin(\theta) & \cos(\theta)\cos(\phi) \end{bmatrix} \begin{bmatrix} \dot{\theta} \\ \dot{\phi} \\ \dot{\psi} \end{bmatrix} \tag{C.12}$$

The derivative of the angular velocities are

$$\dot{\omega}_x = \ddot{\theta} - \ddot{\psi}\sin(\phi) - \dot{\psi}\cos(\phi) \tag{C.13}$$

$$\dot{\omega}_y = \ddot{\phi}\cos(\theta) - \dot{\phi}\sin(\theta) + \ddot{\psi}\sin(\theta)\cos(\phi) + \dot{\psi}\cos(\theta)\cos(\phi) - \dot{\psi}\sin(\theta)\sin(\phi) \tag{C.14}$$

$$\dot{\omega}_z = -\dot{\phi}\sin(\theta) - \dot{\phi}\cos\theta + \ddot{\psi}\cos(\theta)\cos(\phi) - \dot{\psi}\cos(\theta)\sin(\phi) - \dot{\psi}\cos(\theta)\cos(\phi) \tag{C.15}$$

Appendix D

Pull-out results

The figures in this appendix ilustrate the results of A.T.FLOW and SIMO/RIFLEX for the pullout tests in sway, heave, pitch and yaw. Section 4.3 gives the pullout tests for surge and roll. Also for the results of sway, heave, pitch and yaw the results of the model correspond.

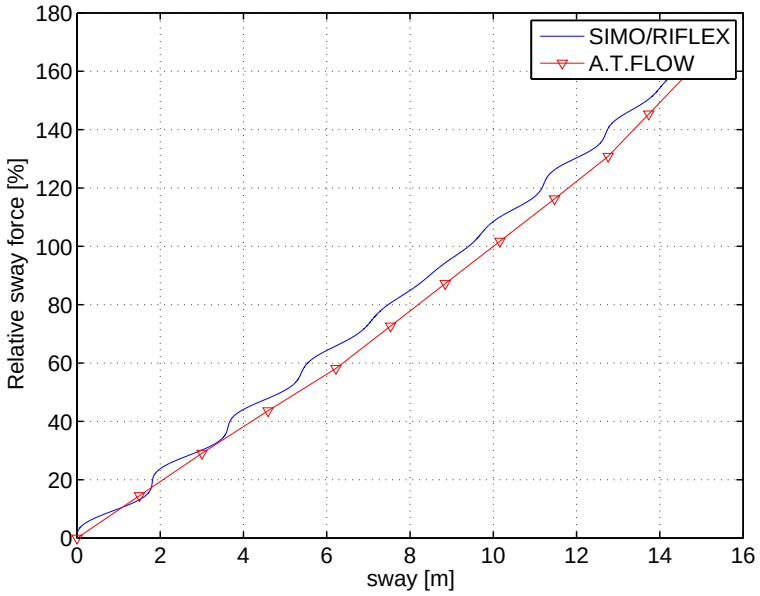

Figure D.1: Pullout test in sway normalized wrt the value of A.T.FLOW at 10 m. Therefore the value at 10 m offset is 100%.

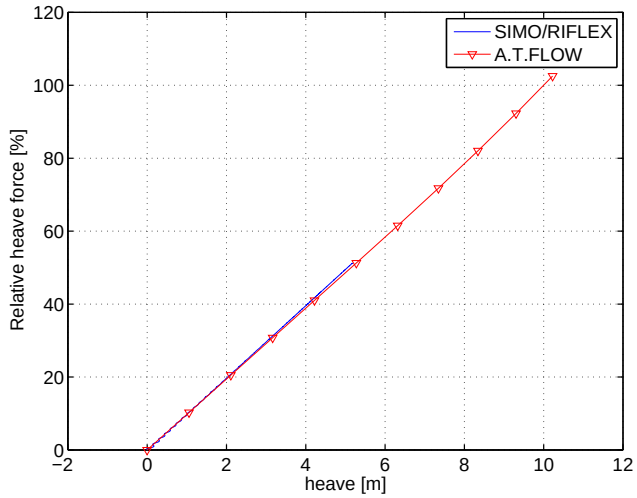

Figure D.2: Pullout test in heave normalized wrt the value of A.T.FLOW at 10 m. Therefore the value at 10 m offset is 100%.

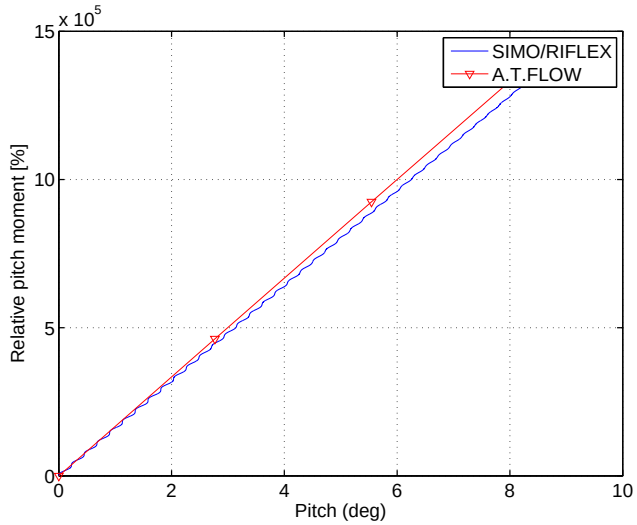

Figure D.3: Pullout test in pitch normalized wrt the value of A.T.FLOW at 6.0 deg. Therefore the value at 6.0 def offset is 100%.

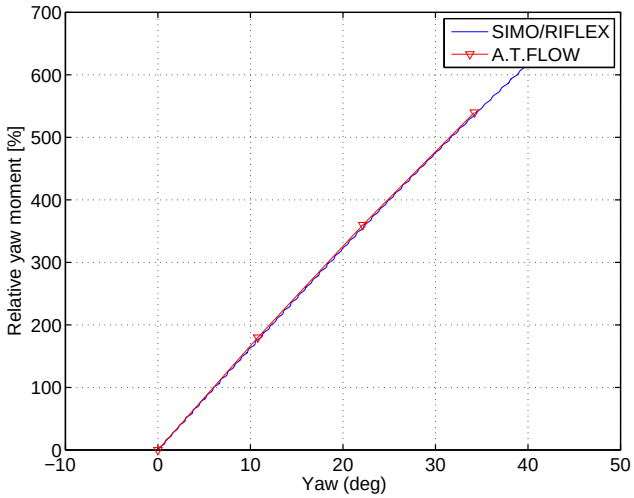

Figure D.4: Pullout test in yaw normalized wrt the value of A.T.FLOW at 6.0 deg. Therefore the value at 6.0 def offset is 100%.

Appendix E

Decay test results

The results of the decay tests for sway, heave, pitch and yaw are given here. The figures show the results from A.T.FLOW and SIMO/RIFLEX.

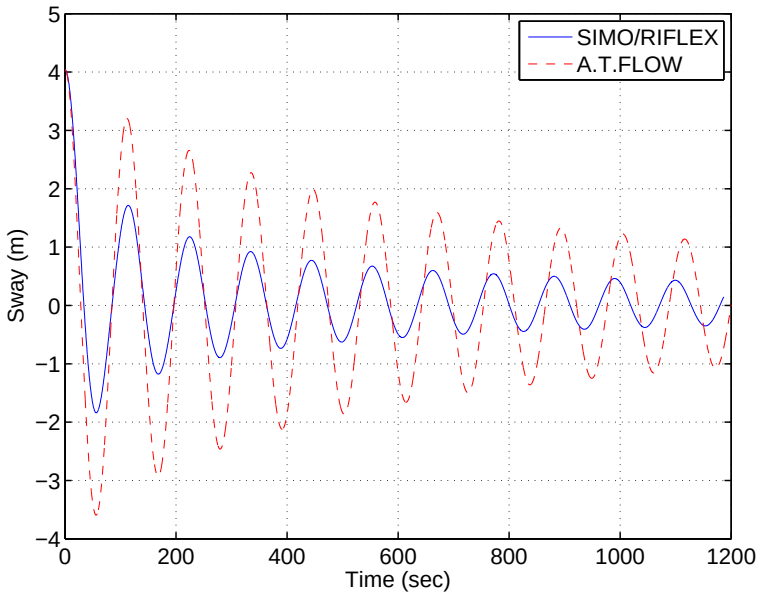

Figure E.1: Decay test in sway

Figure E.1 shows damping curves with more or less the same period, but the damping of SIMO/RIFLEX is much stronger. The damping is much stronger than the damping in surge. This is strange, because the behaviour in surge and sway are almost identical. Only the assymetry of the mooring system creates differences between surge and sway behaviour. The sway damping behaviour of A.T.FLOW is more identical to the surge behaviour from Figure 4.7.

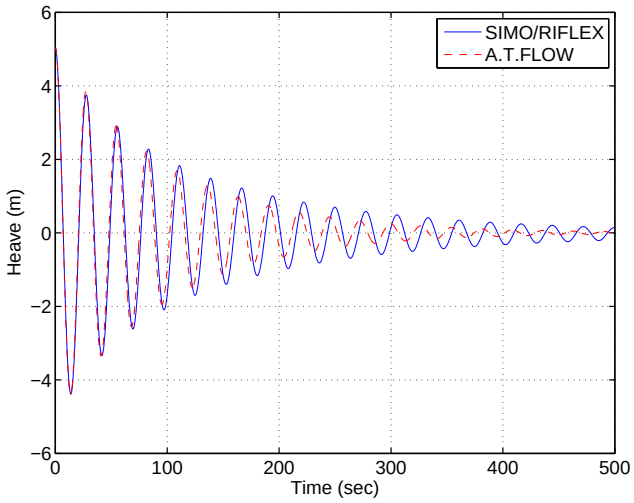

Figure E.2: Decay test in heave

Figure E.2 shows that the period of A.T.FLOW is lower, but the damping is stronger. The pitch and yaw decay test in Figures E.3 and E.2 correspond nicely.

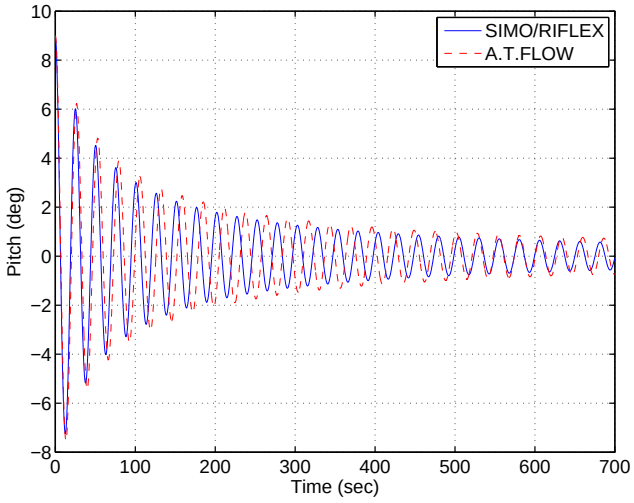

Figure E.3: Decay test in pitch

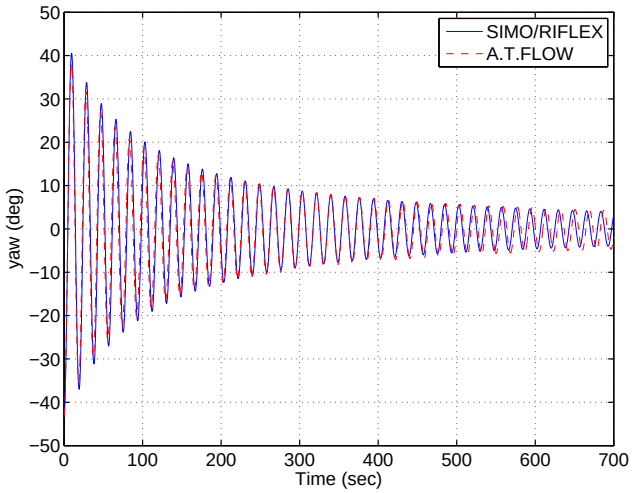

Figure E.4: Decay test in yaw

Appendix F

Results of prediction case 1

This appendix shows the results of prediction case 1: wind-wave yaw misalignments. The results of the aligned situation were already presented in Section 5.2. The results of a 30 deg and 90 deg misalignment are given in Figures F.1 and F.2

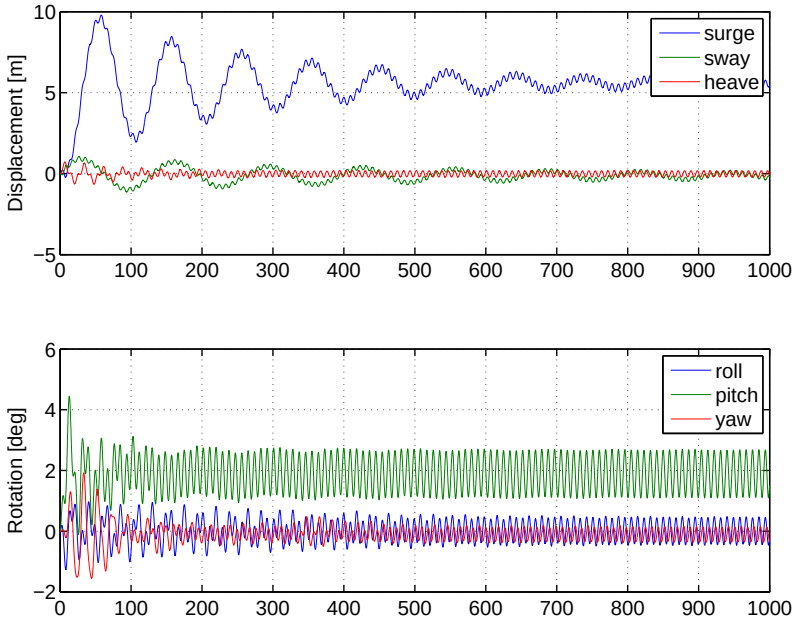

Figure F.1: A.T.FLOW results for case 1 with a wind-wave misalignment of 30 deg

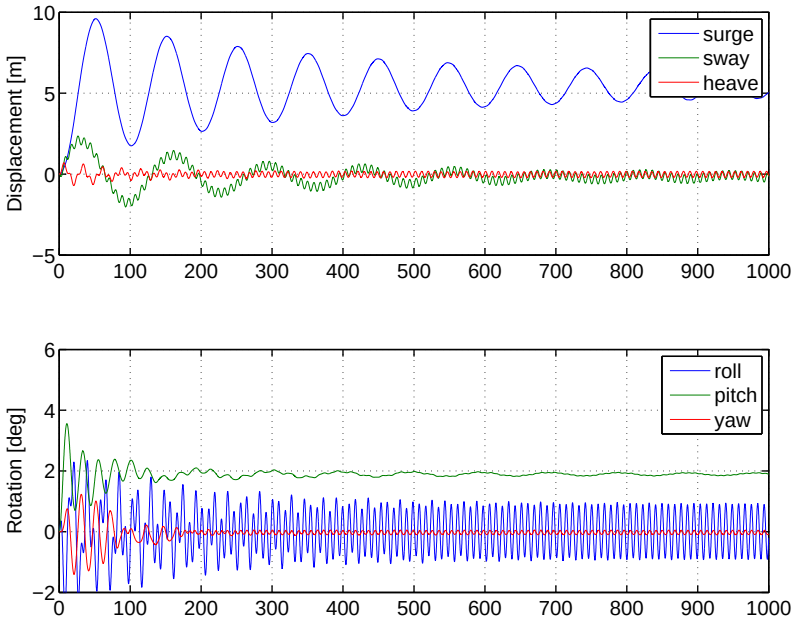

Figure F.2: A.T.FLOW results for case 1 with a wind-wave misalignment of 90 deg

Appendix G

Results of prediction case 2

This appendix shows the results of prediction case 1: wind-rotor yaw misalignments. The results of the aligned situation were already presented in Section 5.3. The results of a 25, 90 and 345 deg misalignment are given in Figures G.1, G.2 and G.4. The aerodynamic torque of 90 and 345 deg misalignment are given in G.3 and G.5.

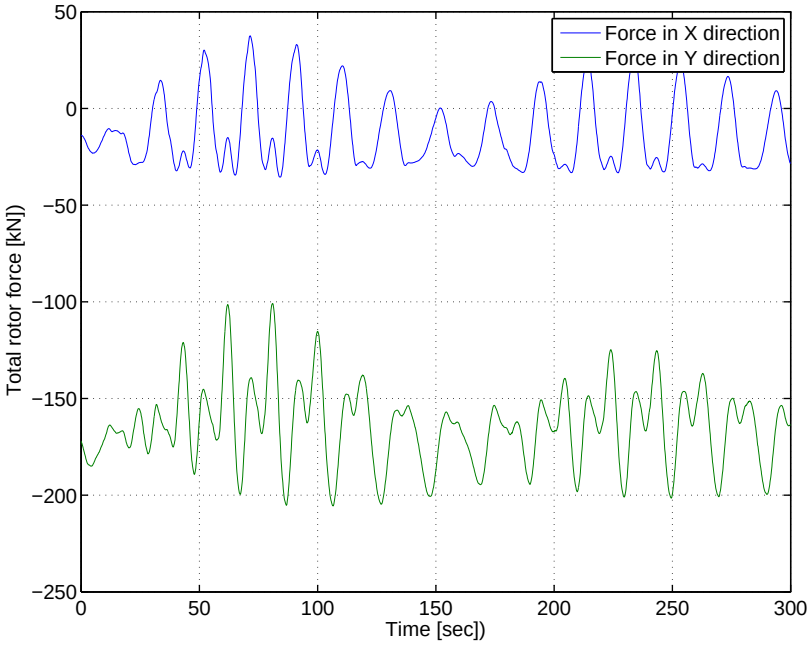

Figure G.1: $\beta w - r = 0$, Aerodynamic force in X direction F_X^{aero} on rotor

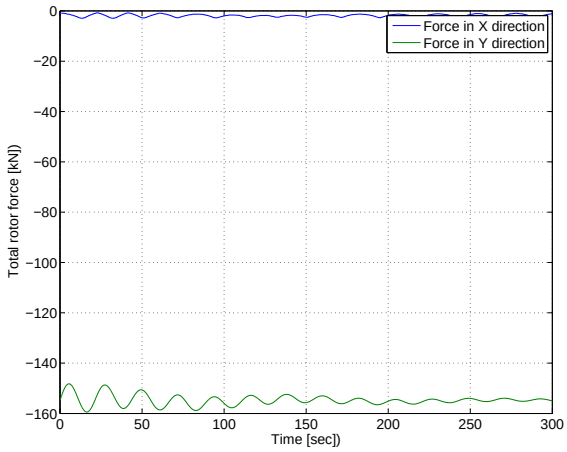

Figure G.2: $\beta_{w-r} = 90$, Aerodynamic force in X direction F_X^{aero} on rotor

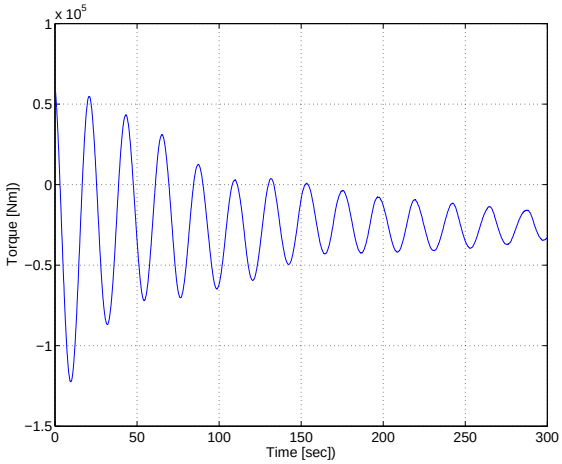

Figure G.3: $\beta_{w-r} = 90$, Aerodynamic torque on rotor

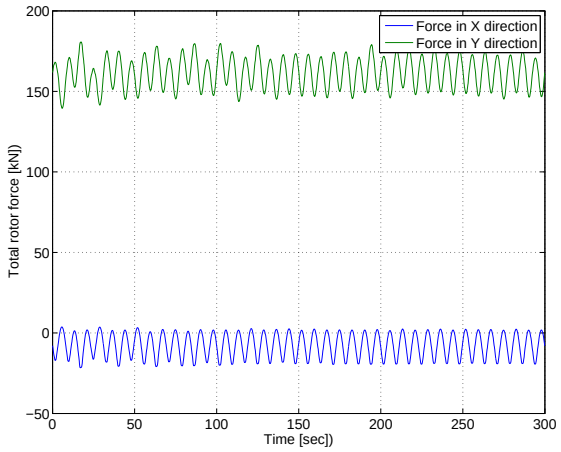

Figure G.4: $\beta_{w-r} = 345$, Aerodynamic force in X direction F_X^{aero} on rotor

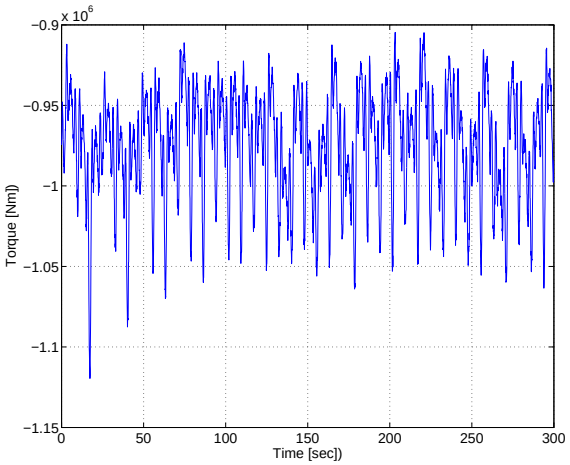

Figure G.5: $\beta_{w-r} = 345$, Aerodynamic torque on rotor

Appendix H

MATLAB differential equation solver ode45

The function of the solver ode45 takes smaller timesteps δt, but not every step requires an output. The timestep δt is enforced by the solver and can not be set. Figure H.2 shows that the solver picks a small timestep with a small increase in accelerations. Larger timesteps occur for all kinds of accelerations. Figures H.1 and H.2 illustrate that the timesteps taken by the solver are in between 0 and 0.045 sec.

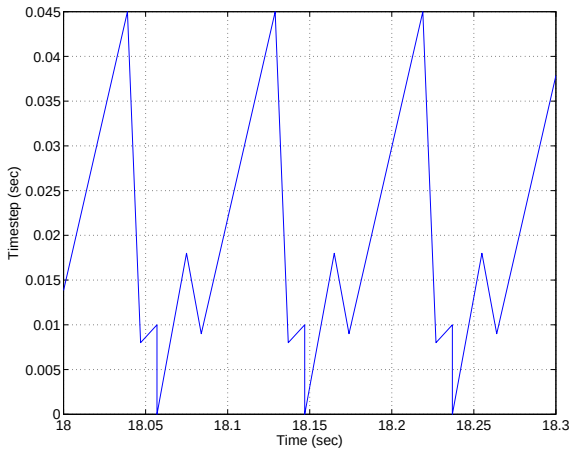

Figure H.1: Time versus the solver timesteps

A limitation of the solver is that T and $\mathbf{S}$ are the only possible outputs. Other parameters can therefore not be stored. The solver function has its own local variables, which are separate from those of other functions, and from those of

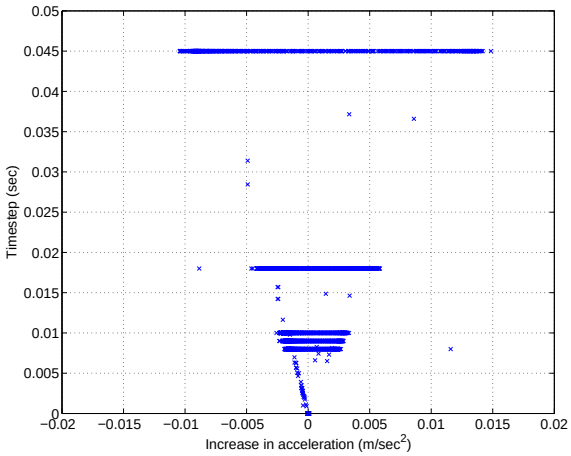

Figure H.2: Increase in surge acceleration versus timesteps

the base workspace. A way to store this data is declaring global variables. If functions declare a particular name as global, they all share a single copy of that variable. Any assignment to that variable, in any function, is available to all the functions declaring it global. In that way all variables can be stored for each timestep. The function itself does not need any modifications.

Bibliography

[1] Hazim Namik, Karl Stol, and Jason Jonkman. State-space control of tower motion for deepwater floating offshore wind turbines. 2008.

[2] J.M. Jonkman. *Dynamics Modeling and Loads Analysis of an Offshore Floating Wind Turbine*. PhD thesis, University of Colorado, Department of Aerospace Engineering Sciences, 2007.

[3] J.M. Jonkman. Development and verification of a fully coupled simulator for offshore wind turbines. *45th AIAA Aerospace Science Meeting and Exhibit*, pages 28–53, 2008.

[4] B. Skaare, T.D. Hanson, and F.G. Nielsen. Importance of control strategies on fatigue life of floating wind turbines. 2007.

[5] T.J. Larsen and T.D. Hanson. A method to avoid negative damped low frequent tower vibrations for a floating, pitch controlled wind turbine. *Journal of Physics: Conference series*, 75, 2007.

[6] F.G. Nielsen, T.D. Hanson, and B. Skaare. Integrated dynamic analysis of floating offshore wind turbines. volume 2006, pages 671–679, 2006.

[7] J.M. Jonkman. Influence of control on the pitch damping of a floating wind turbine. *27th ASME Wind Energy Symposium*, 2008.

[8] Siemens Wind Power. Comparison of results from bhawc, hawc2 and hawc2simoriflex (h2sr). Technical report, 2009.

[9] D.P. Molenaar. *Cost-effective Design and Operation of Variable Speed Wind Turbines - Closing the gap between the control engineering and the wind engineering community*. PhD thesis, Delft University of Technology, 2003.

[10] B. Skaare, T.D. Hanson, and F.G. Nielsen. Integrated dynamic analysis of floating offshore wind turbines. 2007.

[11] M.S. Triantafyllou et al. Dynamic analysis as a tool for open sea mooring system design. *Trans. SNAME*, 93:303–324, 1985.

[12] S.A. Mavrakos et al. Deep water mooring dynamics. *Marine structures*, 9:181–209, 1995.

[13] Hydro. Design brief for offshore floating wind-mills. Technical report, 2005.

[14] J.M. Jonkman. Definition of the floating system for phase iv of oc3. Technical report, 2009.

[15] S.A. Mavrakos and J Chatjigeorgiou. Dynamic behaviour of deep water mooring lines with submerged buoys. *Computers and Structures*, 66:819–835, 1997.

[16] T Sant. *Improving BEM-based Aerodynamic Models in Wind Turbine Design Codes*. PhD thesis, Technical University Delft, 2007.

[17] L.H. Holthuijsen. *Waves in Oceanic and Coastal Waters*. Cambridge University Press, 2007.

[18] O.M. Faltinsen. *Sea loads on Ships and Offshore Structures*. Cambridge University Press, 1990.

[19] Manwell et al. *Wind Energy Explained*. Wiley.

[20] D.P. Molenaar. *DAWIDUM User's guide*.

[21] J.R. Morison et al. The force exerted by surface wave on piles. *Petroleum Transactions (American Institute of Mining Engineers)*, 75, 1950.

[22] J.M. Jonkman. Definition of the floating system for phae iv of oc3. 2009.

[23] D.J. Rixen. Mechanical analysis for engineering. Technical report, 2008.

[24] DUWIND. *Introducation to Dynamics*.

[25] IEC. Iec 61400-1 ed.3: Wind turbines - part 1: Design requirements. Technical report, 2005.

[26] Josef S. Torok. *Analytical Mechanics, with an introduction to Dynamical Systems*. Wiley-Interscience, 2000.

Notations

Part I: Modeling of a spar-type floating offshore wind turbine

Degrees of freedom and coordinate systems

$\hat{i}$	Global base vector	-
$\hat{j}$	Global base vector	-
$\hat{k}$	Global base vector	-
$\hat{m}$	Local base vector	-
$\hat{n}$	Local base vector	-
$\hat{l}$	Local base vector	-
$\hat{p}$	Local base vector	-
$\hat{q}$	Local base vector	-
x	Local position in $\hat{m}$ direction	m
X	Global position in $\hat{i}$ direction, Surge	m
y	Local position in $\hat{n}$ direction	m
Y	Global position in $\hat{j}$ direction, Sway	m
z	Local position in $\hat{l}$ direction	m
Z	Global position in $\hat{k}$ direction, Heave	m
θ	Euler angle, roll	rad
ϕ	Euler angle, pitch	rad
ψ	Euler angle, yaw	rad

Controller

γ_2	Blade pitch angle	rad
Ω	Angular velocity of rotor	rad s^{-1}

Wind module

D_t	Tower diameter at height H	m
H	Height from MWL	m
H_{obs}	Height of wind speed observation	m
R_{shadow}	Shadow ratio	-
R_{shear}	Shear ratio	-
V_{field}	Undisturbed wind field velocity	m s^{-1}
V_w	Undisturbed wind velocity at hub height	m s^{-1}
X_{sh}	Distance in X direction from blade to tower center	m
Y_{sh}	Distance in Y direction to tower center	m
α_{PL}	Power law constant	-
β_{wind}	Wind angle direction	rad
β_{rotor}	Rotor angle direction	rad

Aerodynamic module

a	Axial induction factor	-
a'	Tangential induction factor	-
A_r	Rotor disk area	m^2
c	Airfoil chord length	m
C_l	Lift coefficient	-
C_d	Drag coefficient	-
C_T	Thrust coefficient	-
$\vec{F}^{aero}$	Aerodynamic force vector with global coordiantes	N
F_q^{aero}	Aerodynamic force in $\hat{q}$ direction	N
F_l^{aero}	Aerodynamic force in $\hat{l}$ direction	N
$\vec{M}^{aero}$	Aerodynamic moment vector with global coordiantes	Nm
N_b	Number of blades	-
r_b	Blade element radius	m
V_{ax}	Perpendicular wind velocity at rotor disk position	m $^s-1$
V_t	Tangential wind velocity at rotor disk position	m $^s-1$
V_p	Free stream wind speed perpendicular to rotor	m $^s-1$
V_∞	Wind velocity far downstream in the wake	m $^s-1$
W	Resultant wind velocity	m $^s-1$
x_b	Local coordinate of x-axis of blade element	m
$\dot{x}_p$	Velocity of blade element in $\hat{p}$ direction	m $^s-1$
$\dot{x}_t$	Velocity of blade element in $\hat{t}$ direction	m $^s-1$
y_b	Local coordinate of y-axis blade element	m
z_b	Local coordinate of z-axis blade element	m
α	Angle of attack	rad
γ_1	Fixed twist angle	rad

ΔF_p	Aerodynamic force in $\hat{p}$ direction	N
ΔF_t	Aerodynamic force in $\hat{t}$ direction	N
Δr	Length of the blade element	m
ΔL	Aerodynamic lift force on blade element	N
ΔD	Aerodynamic drag force on blade element	N
ΔQ	Aerodynamic torque on blade element	N
ϕ	Angle of inflow of W	rad
ρ_{air}	Air density	kg m^{-3}

Waves module

d	Water depth	m
H_w	Wave height	m
k_{wave}	Wave number	rad s^{-1}
s	horizontal translation of the spar section in the direction of the wave	m
t	Time	s
U_a	Wave amplitude	m
α_w	Wave phase	rad
β_{wave}	Wave angle	rad
$\dot{\eta}$	Wave velocity	m s^{-1}
$\ddot{\eta}$	Wave acceleration	m s^{-2}
η_h	Translations of wave particles in horizontal plane	m
η_Z	Wave translation in Z direction	m
η_X	Wave translations in X direction	m
η_Y	Wave translations in Y direction	m
ω_w	Wave number	rad s^{-1}

Mechanical module

F_h^{line}	Horizontal mooring line tension	N
F_v^{line}	Vertical mooring line tension	N
F_X^{line}	Total mooring line force in X direction	N
F_Y^{line}	Total mooring line force in Y direction	N
F_Z^{line}	Total mooring line force in Z direction	N
$\vec{F}^{mooring}$	Mooring force vector	N
g	Gravitational acceleration	m s^{-2}
I_{xx}^r	Moment of inertia about x axis	kg m^2
m	Mass of the system	kg
$\vec{M}^{gyros}$	Gyroscopic moment vector	Nm
$\vec{M}^{mooring}$	Mooring moment vector	Nm
$\vec{W}$	Weight vector	N

β^{line}	Mooring line angle	rad
Ω	Angular velocity of the rotor	rad s^{-1}
ω_z	Body angular velocity around z axis	rad s^{-1}
ω_y	Body angular velocity around y axis	rad s^{-1}

Hydrodynamic module

A_{surf}	Spar area at water surface	m^2
A_s	Cross-section area of spar section	m^2
C_a	Added mass coefficient	-
C_{bot}	Damping coefficient of the bottom plate	kg s^{-1}
C_D	Local drag coefficient	-
C_m	Inertia coefficient	-
c_x	Local constant current velocity in x direction	m s^{-1}
D	Local spar diameter	m
D_{bot}	Spar diameter at bottom	m
F_b	Buoyancy force	N
$\vec{F}_{xy}^{drag}$	The hydrodynamic drag force on the side	N
$\vec{F}_{bot}^{hydro}$	The hydrodynamic force vector on the bottom with global coordinates	N
$\vec{F}_{xy}^{hydro}$	The hydrodynamic force on the side	N
F_{side}^{hydro}	The hydrodynamic force vector on the side with global coordinates	N
$\vec{F}_{xy}^{inertia}$	The hydrodynamic inertia force on the side	N
g	Gravitational acceleration	m s^{-2}
m_{a1}	Added mass of the spar section side	kg
m_{a2}	Added mass of the bottom	kg
M_{side}^{hydro}	The hydrodynamic force moment on the side with global coordinates	N
r_1	Distance from center of mass of part 1 to cg	m
u_Z	Translation in Z-direction in global coordinate system	m
V_{displ}	Displaced water volume when $u_Z = 0$	m^3
V_1	Volume of the displaced water of spar part 1	m^3
$\dot{x}_s$	Local velocity of spar in x direction	m s^{-1}
$\ddot{x}_s$	Local acceleration of spar in x direction	m s^{-2}
η_{surf}	Wave elevation at surface	m
$\dot{\eta}_x$	Local velocity of wave particle in x direction	m s^{-1}
$\ddot{\eta}_x$	Local acceleration of wave particle in x direction	m s^{-2}
Δm	Mass of spar section	kg
ΔI	Moment of inertia of spar section	kg m
ΔI_a	Rotational added mass of spar section	kg m
Δz_s	Unit length of spar section	m
$\dot{\omega}$	Angular acceleration of spar section	rad s^{-2}
ρ_{sea}	Sea water density	kg m^{-3}

DOF Solver

$\vec{f}$	Total external force vector	N
$\vec{F}^{aero}$	Aerodynamic force vector	N
$\vec{F}^{hydro}$	Hyrdostatic and hydrodynamic force vector	N
$\vec{F}^{mooring}$	Mooring force vector	N
F_X	Total external force vector in X direction	N
F_Y	Total external force vector in Y direction	N
F_Z	Total external force vector in Z direction	N
$\mathbf{I}$	Moment of inerta matrix	kg m^2
m	Mass of the system	kg
$\mathbf{M}$	Mass matrix	kg
m_{a1}	Added mass of the spar section side	kg
m_{a2}	Added mass of the bottom	kg
$\vec{M}^{aero}$	Aerodynamic moment vector	Nm
$\vec{M}^{gyros}$	Gyroscopic moment vector	Nm
$\vec{M}^{hydro}$	Hyrdostatic and hydrodynamic moment vector	Nm
$\vec{M}^{mooring}$	Mooring moment vector	Nm
$\ddot{\vec{r}}$	Translational acceleration vector	m s^{-2}
$\vec{W}$	Weight vector	N
X	Global coordinate, Surge	m
Y	Global coordinate, Sway	m
Z	Global coordinate, Heave	m
$\dot{X}$	Surge velocity	m s^{-1}
$\dot{Y}$	Sway velocity	m s^{-1}
$\dot{Z}$	Heave velocity	m s^{-1}
θ	Euler angle, roll	rad
$\dot{\theta}$	Roll angular velocity	rad s^{-1}
ϕ	Euler angle, pitch	rad
$\dot{\phi}$	Pitch angular velocity	rad s^{-1}
ψ	Euler angle, yaw	rad
$\dot{\psi}$	Yaw angular velocity	rad s^{-1}
$\dot{\vec{\omega}}$	Angular acceleration vector	rad s^{-2}
$\dot{\omega}_x$	Angular acceleration around x axis	rad s^{-2}
$\dot{\omega}_y$	Angular acceleration around y axis	rad s^{-2}
$\dot{\omega}_z$	Angular acceleration around z axis	rad s^{-2}

Part II: Verification and predictions

β_{w-w}	Wind-wave yaw misalignment	rad
β_{w-r}	Wind-rotor yaw misalignment	rad
α_{az}	Blade azimuth angle	rad
V_{gust}	Free stream wind velocity during gust	m s^{-1}
ΔV	Amplitude of gust	m s^{-1}
T_{gust}	Period of gust	s

Part III: Appendices

$\vec{F}_{xyz}$	The force vector with local coordinates x, y and z	N
$\vec{F}_{XYZ}$	The force vector with global coordinates X, Y and Z	N
F_x	Force in the local x direction	N
F_X	Force in the global X direction	N
F_y	Force in the local y direction	N
F_Y	Force in the local Y direction	N
F_z	Force in the local z direction	N
F_Z	Force in the global Z direction	N
$\vec{r}_{cg}$	The position vector of the center of gravity	m
$\vec{r}_p$	The position vector of point p on the structure in the global coordinate system	m
$\vec{r}_{rel}$	The position of point p relative to point 0 in the global coordinate system	m
R_θ	Transformation matrix of roll	-
R_ϕ	Transformation matrix of pitch	-
R_ψ	Transformation matrix of yaw	-
$\vec{v}_p$	The velocity of a point on a rigid body	m s^{-1}
$\vec{v}_{cg}$	The velocity of cg of a rigid body	m s^{-1}
$\vec{\omega}$	Angular velocity vector	rad s^{-1}
ω_x	Angular velocity around x axis	rad s^{-1}
ω_y	Angular velocity around y axis	rad s^{-1}
ω_z	Angular velocity around z axis	rad s^{-1}

Abbrevations

A.T.FLOW	Analysis Tool for Floating Offshore Wind
BHawC	Bonus Horizontal Axis Wind Code
cg	Center of mass of the full body
cb	Center of buoyancy
MWL	Mean water level
SWT 2.3-82	Siemens wind turbine with rated power of 2.3 MW and rotor diameter of 82.4 m
TP	Transition piece

Definitions

Hywind	Hydro Oil and Energy floating wind turbine concept
Turbine	Contains blades, nacelle, hub, upper tower and middle tower
Transition piece	Lower tower
Platform	Turbine plus transition piece plus substructure